UNIVERSITÀ DEGLI STUDI DI TORINO
Dipartimento di Fisica Sperimentale

J/ψ , ψ' and Drell-Yan production in proton-nucleus collisions at 450 GeV incident energy at the CERN SPS

Tesi di Dottorato di Ricerca
di
Pietro Cortese

Relatori

Prof. G. Dellacasa

Dott. E. Scomparin

Contro-Relatore

Prof. P. Force

XIII CICLO

Anni Accademici 1997-2000

Coordinatore
Prof. R. Garfagnini

Alla mia famiglia

Ringraziamenti

Voglio ringraziare innanzitutto il mio relatore Prof. Giuseppe Dellacasa, per il suo entusiasmo, per l'aiuto e l'incoraggiamento che mi ha dato fin dalla mia attività di tesi e per avermi dato l'opportunità di coltivare la mia passione per la Fisica.

Poi ringrazio Enrico per avermi introdotto all'analisi dei dati e per tutto l'aiuto prezioso nello svolgimento di questo lavoro.

Insieme a loro ringrazio tutti gli altri componenti del gruppo Pinot per la loro simpatia, per l'amicizia e la stima che mi hanno sempre dimostrato: il Prof. Emilio Chiavassa e poi Alessandro, Alfredo, Anna, Chiara, Enrico, Ermanno, Federica, Giovanna, Mauro, Nora, Pierluca e Roberta.

I would like to thank Louis Kluberg and the NA50 Collaboration for the unique opportunity to make this analysis. Finally, I want to thank Paul Force who accepted to report on my work for the final examination of my PhD thesis.

Introduction

Quantum Chromo Dynamics (QCD) calculations predict that, at sufficiently high temperature (of the order of $T_c \sim$ 150–180 MeV), ordinary nuclear matter undergoes a phase transition to a state of matter where quarks and gluons are no more confined inside hadrons, but behave as free particles. If the partons remain deconfined for long enough, their kinematical distributions reach thermal characteristics, and such a state is named Quark-Gluon Plasma (QGP).

Ultrarelativistic ion collisions are supposed to be able to create the initial conditions of temperature and energy density necessary for the formation of the deconfined state. In particular, at BNL and CERN, since 1986, an experimental program involving several hundreds of researchers on each site, has studied in detail the characteristics of the final state produced in these collisions, with the aim of discovering the specific signals theoretically proposed as signatures of the phase transition. The explored center of mass energy of the collision ranges from $\sqrt{s} \sim 3$ GeV (AGS at Brookhaven) to $\sqrt{s} \sim 20$ GeV (SPS at CERN). Very recently, at BNL, the Relativistic Heavy Ion Collider (RHIC) has started to deliver beams at $\sqrt{s}$=65 and 130 GeV and will soon accelerate Au ions at $\sqrt{s}$=200 GeV.

One of the most interesting signatures of the QGP formation is the J/ψ suppression. In particular, Matsui and Satz predicted that in a QGP the colour binding potential between the c and $\overline{c}$ quark would be screened, leading to a measurable reduction of the J/ψ yield. The NA38, NA50 and NA51 collaborations have performed, since 1986, a study of J/ψ production in proton-proton, proton-nucleus and nucleus-nucleus collisions (using ^{16}O, ^{32}S and ^{208}Pb projectiles).

Of course, dissociation processes at the hadronic level can also give a sizeable J/ψ suppression, making somewhat more complicate the analysis of the experimental results. In particular, the NA50 experiment has shown that, while the data from p-p to central S-U collisions can be reasonably explained in terms of J/ψ suppression due to hadronic processes, in Pb-Pb collisions there is an extra-suppression (usually called "anomalous suppression") that can not be explained with conventional mechanisms and appears to be due to QGP creation.

This conclusion is mainly based on the different behaviour between the J/ψ suppression pattern observed in S-U collisions and the one measured in Pb-Pb collisions. In fact, data on p-A interactions were up to now much less accurate. Such data, however, are very interesting since they can help, in absence of effects due to a QGP, to distinguish between the various sources of hadronic suppression of the J/ψ. In particular the J/ψ can be suppressed either by the nuclear environment created by the projectile and target nucleons. This source of suppression is present both in p-A collisions (where of course only the target nucleons

contribute) and in A-A collisions. Another source of suppression, present only in A-A collisions, is the interaction with the created hadronic secondary particles. These particles (usually called "hadronic comovers" or simply "comovers") move together with the J/ψ and can destroy the bound state.

Clearly, this topic can be investigated by carefully comparing J/ψ production in p-A and S-U collisions. Having recognized the importance of these studies, the NA50 collaboration has recently taken data on p-A interactions on different nuclear targets. The present thesis will concentrate on the analysis of these data and will show the first results, together with a comparison with the (older) S-U data.

Chapter 1 deals with basic remarks on the charmonium physics. In Chapter 2 the NA50 experimental apparatus will be described. Chapter 3 is devoted to a description of the technical aspects of the analysis. In particular the reconstruction procedure for dimuon events, the quality cuts and the run selection criteria will be detailed. In Chapter 4 I describe the Monte-Carlo simulation of the experimental apparatus, and its use for the calculation of the expected invariant mass shapes for the various physical processes (Drell-Yan, J/ψ, ψ'). The subtraction of combinatorial background, and of empty target contribution is also described. Chapter 5 contains the results of the analysis of p-A data. In particular the calculation of the cross sections $\sigma_{J/\psi}$, $\sigma_{\psi'}$ and σ_{DY} is presented in detail, with emphasis on the determination of systematic errors. The ratios of cross sections $\sigma_{J/\psi}/\sigma_{DY}$ and $\sigma_{\psi'}/\sigma_{DY}$ are also presented and their role in reducing systematic errors is discussed. Finally, in Chapter 6 I compare the p-A results with previous NA38 results on S-U collisions. First I show how to solve the problems connected with the comparison of data taken in different kinematic conditions, and finally I extract and compare, in the framework of a simple model, the values for the dissociation cross section of J/ψ and ψ'.

Introduzione

I calcoli della Cromodinamica Quantistica (QCD) predicono che, ad una temperatura sufficientemente elevata (dell'ordine di $T_c \sim 150$–180 MeV), la materia nucleare ordinaria attraversi una transizione di fase verso uno stato in cui i quark ed i gluoni non sono più confinati all'interno degli adroni, ma si comportano come particelle libere. Se i partoni rimangono nello stato deconfinato abbastanza a lungo raggiungono una situazione di equilibrio termico; questo stato è chiamato Quark-Gluon Plasma (QGP).

Le collisioni di ioni ultrarelativistici sono un possibile mezzo per creare in laboratorio le condizioni di temperatura e densità di energia necessarie per la formazione dello stato deconfinato. Al BNL e al CERN, a partire dal 1986, è stato avviato un programma sperimentale che coinvolge centinaia di ricercatori presso ciascun laboratorio; questo ha permesso di studiare in dettaglio le caratteristiche dello stato finale prodotto in queste collisioni, allo scopo di rivelare segnali specifici, proposti dalla teoria come "segnature" della transizione di fase. Si sono studiate collisioni ad energie nel centro di massa che vanno da $\sqrt{s} \sim 3$ GeV (AGS a Brookhaven) a $\sqrt{s} \sim 20$ GeV (SPS al CERN). Recentemente, al BNL, il Relativistic Heavy Ion Collider (RHIC) ha cominciato a fornire fasci a $\sqrt{s}$=65 e 130 GeV e presto accelererà ioni Au a $\sqrt{s}$=200 GeV.

Una delle più interessanti segnature della formazione del QGP è la soppressione della J/ψ. Matsui e Satz hanno predetto che in un QGP il potenziale di colore tra i quark c e $\overline{c}$ verrebbe schermato, portando ad una significativa riduzione della produzione di J/ψ. Le collaborazioni NA38, NA50 e NA51 hanno effettuato, a partire dal 1986, uno studio della produzione di J/ψ in collisioni protone-protone e nucleo-nucleo (usando come proiettili ioni ^{16}O, ^{32}S e ^{208}Pb).

Naturalmente anche processi di dissociazione a livello adronico possono dare un considerevole contributo alla soppressione della J/ψ, rendendo in qualche modo più complicata l'analisi dei risultati sperimentali. In particolare l'esperimento NA50 ha mostrato che, mentre i dati a partire da p-p fino alle collisioni centrali S-U possono essere descritti in modo soddisfacente in termini di una soppressione della J/ψ dovuta a processi adronici, nelle collisioni Pb-Pb c'è una ulteriore soppressione (detta solitamente "soppressione anomala") che non può essere spiegata in base a meccanismi convenzionali ed è dovuta molto probabilmente alla formazione di un QGP.

Questa conclusione è basata principalmente sul diverso comportamento della soppressione della J/ψ che si osserva in collisioni S-U e quello misurato in collisioni Pb-Pb. Infatti, fino ad ora, i dati per interazioni p-A, che avrebbero costituito il riferimento ideale, erano molto meno accurati. Questi dati tuttavia sono molto

interessanti poiché possono aiutare a distinguere, in assenza di effetti dovuti alla formazione di un QGP, le diverse sorgenti di soppressione della J/ψ di tipo adronico. Infatti la J/ψ può essere soppressa dalle interazioni con l'ambiente nucleare creato dal proiettile e dal bersaglio. Questa sorgente di soppressione è presente sia in collisioni p-A (dove contribuiscono solo i nucleoni del bersaglio) sia in collisioni A-A. Un'altra sorgente di soppressione, presente solo in collisioni A-A, è l'interazione della J/ψ con gli altri adroni generati nella collisione. Queste particelle (di solito chiamate "hadronic comovers" o semplicemente "comovers") si muovono insieme alla J/ψ e possono distruggere lo stato legato. Chiaramente questo può essere studiato paragonando accuratamente la produzione di J/ψ in collisioni p-A e S-U.

Avendo riconosciuto l'importanza di questi studi, la collaborazione NA50 ha recentemente acquisito dati in interazioni p-A su differenti bersagli. Questa tesi si concentra sull'analisi di questi dati, riporta i primi risultati ottenuti e li paragona con i precedenti dati di collisioni S-U.

Nel Capitolo 1 si descrive brevemente la fisica del charmonio. Nel Capitolo 2 si descrive l'apparato dell'esperimento NA50. Il Capitolo 3 considera gli aspetti tecnici dell'analisi dei dati. In particolare vengono descritte in dettaglio la procedura usata per ricostruire gli eventi "dimuone", i tagli sulla qualità delle tracce e i criteri di selezione dei "run". Nel Capitolo 4 descrivo la simulazione Monte-Carlo dell'apparato sperimentale e come questa viene usata per calcolare le forme teoriche degli spettri di massa invariante dei diversi processi fisici (Drell-Yan, J/ψ, ψ'). Viene anche descritta la procedura per la sottrazione del fondo combinatoriale e del contributo di "bersaglio vuoto". Il Capitolo 5 contiene i risultati dell'analisi dei dati protone-nucleo. I calcoli delle sezioni d'urto $\sigma_{J/\psi}$, $\sigma_{\psi'}$ e σ_{DY} vengono presentati in dettaglio con un'enfasi particolare sulla determinazione degli errori sistematici. Vengono poi presentati i rapporti di sezioni d'urto $\sigma_{J/\psi}/\sigma_{DY}$ e $\sigma_{\psi'}/\sigma_{DY}$ e viene discusso il loro ruolo nella riduzione degli errori sistematici. Infine nel Capitolo 6 paragono i risultati p-A con i precedenti risultati di NA38 su collisioni S-U. Inizialmente mostro come risolvere i problemi che si creano quando si paragonano dati acquisiti in differenti condizioni cinematiche e infine, nell'ambito di un semplice modello, estraggo e paragono i valori per la sezione d'urto di dissociazione della J/ψ e ψ'.

Contents

Chapter 1

Physical motivation

Statistical Quantum Chromo Dynamics predicts that strongly interacting nuclear matter, at sufficiently high density, undergoes a transition to a state of deconfined quarks and gluons named Quark Gluon Plasma (QGP). This condition can be reached in relativistic heavy ion collisions.

Various signatures can be studied to identify the occurrence of this phase transition. Signals emerging from the collisions keep information about the stage when they were formed and also about the successive evolution because of the interactions that occurred in the later stages.

Light mesons and baryons have large hadronic cross sections and thus will interact strongly in the medium. They carry informations on quark abundances produced in the early stage of the interaction but final abundances are fixed only when the last inelastic hadron-hadron interaction takes place. It is therefore more interesting, for the study of the early stage of the collision, when a QGP would be formed, to choose particles that weakly interact with the surrounding medium.

Good candidates for such studies are dilepton pairs. Unfortunately the different physical sources can be difficult to disentangle, since their contributions to the measured invariant mass spectra can overlap.

The most interesting probe in dilepton studies at SPS energies is the J/ψ which decays into a lepton pair and forms a narrow peak in the invariant mass spectrum.

In 1986, Matsui and Sats [1] predicted that the production of J/ψ and other quarkonium states would be suppressed in a QGP by colour screening. In a deconfined medium, in fact, the $c\bar{c}$ pairs that are produced are not able to form a bound $c\bar{c}$ state.

The cross section for J/ψ -hadron interactions, if compared with that of light mesons as pions and kaons, is small but not negligible. So the interpretation of the J/ψ signal in nucleus-nucleus collisions depends on the final state interaction of the J/ψ . Basically we expect a "normal" J/ψ suppression, due to the interaction

of the meson with projectile and target nucleons, or with produced hadrons, superimposed to a possible "anomalous" suppression, due to colour screening in a QGP.

The study of "normal" suppression can be performed in proton-nucleus collisions where no Quark Gluon Plasma formation is expected but the produced J/ψ can re-interact in its way through the target nucleus. In this way we can establish a reference, useful to understand nucleus-nucleus data.

1.1 The J/ψ

The J/ψ is an hadronic resonance. It was discovered in 1974 simultaneously at the "Brookhaven National Laboratory" and at the "Stanford Linear Accelerator Center". Hence the two names; it was christened J at Brookhaven and ψ at SLAC.

It's a bound state of charm (c) and anti-charm ($\bar{c}$) quarks in a $1S$ triplet state with mass 3096.87 ± 0.04 MeV with full width 85 ± 5 KeV . It's very stable because it can not decay into two charmed mesons because of energy conservation.

The $c\bar{c}$ states form a wide spectrum of bound states with different quantum numbers. Important in this study are also the $\psi(2S)$ named ψ' and the $\chi(1P)$ states that will be called χ_c in the following.

Both the J/ψ and the ψ' decay into two muons with a branching ratio of $(3.88 \pm 0.10)\,\%$ and $(1.03 \pm 0.35)\,\%$ respectively [2].

1.2 J/ψ production models

Some models have been proposed to describe quarkonium production in hadronic interactions.

The J/ψ production is thought to occur into different steps. First, we have the production of a $c\bar{c}$ pair from the scattering of a projectile on a target parton. This can involve two contributions: the fusion of two gluons or the annihilation of a quark with a sea anti-quark. The $c\bar{c}$ can be either in a colour singlet state or in a colour octet state. The two processes are represented in Figure 1.1.

The second step is the binding of the $c\bar{c}$ pair into a J/ψ or another hadronic resonance. This involves the colour neutralisation of the pair via an interaction with other quarks or gluons, to finally give a colour singlet state.

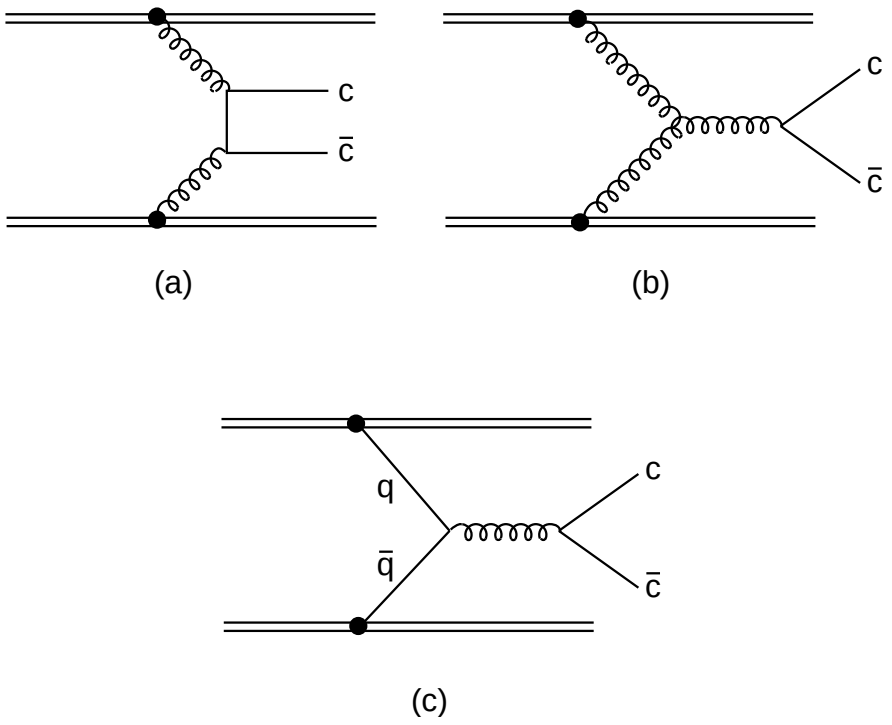

Figure 1.1: Lowest order diagrams for $c\bar{c}$ production in hadronic collisions through (a,b) gluon fusion and (c) $q\bar{q}$ annihilation.

1.2.1 The "Colour Evaporation" model

In the "Colour Evaporation" model charmonia production is treated in the same way as open charm production. At the leading order of perturbative QCD it is a hard-scattering process that involves gg fusion or $q\bar{q}$ annihilation.

The elementary cross sections are a function of the invariant mass of the $c\bar{c}$ pair (m) and of the momentum fractions (x_1 and x_2) of the colliding partons or gluons.

They are integrated over the x_1 and x_2 variables with the conditions:

$$\begin{aligned} m^2 &= x_1 x_2 s \\ y &= \frac{1}{2} ln \left(\frac{x_1}{x_2} \right) \end{aligned}$$

and then summed over the quark flavours.

The resulting cross section is then integrated over the invariant mass between $2m_c$ and $2m_D$, i.e. the highest possible mass value for bound $c\bar{c}$ states.

ψ'/ψ	$(\sum_J \chi_c \to J/\psi + X)/\psi$
0.14	0.4

Table 1.1: Production ratios of charmonium states from colour evaporation model. These numbers include direct and indirect production. The NLO calculation has been done with the MRS D - ' parton densities.

Once formed, the $c\bar{c}$ pair has to hadronize in order to give the physical resonant state; in particular it has to neutralise its colour. This process is non-perturbative and is included in a factor f_H that is fitted from the experimental data. Once f_H has been fixed for each state: J/ψ , ψ' and χ_c the model predicts energy and momentum dependencies.

The colour evaporation model does not give a theoretical basis for the production fractions f_H . The assumption is that the production dynamic for resonance production is the same as the underlying $c\bar{c}$ production, so the f_H factor is connected with hadronization only and does not depend on the dynamic of the process.

A consequence of the above assumption is that the ratios of cross sections of different quarkonium states does not depend on the dynamic of the collision. In particular:

$$\frac{\sigma(\psi')}{\sigma(J/\psi)} = \frac{f_{\psi'}}{f_{J/\psi}} \tag{1.1}$$

This appear to be true, in a first approximation, for charmonia production. The fitted ratios are reported on Table 1.1. In Figure 1.2 the ratio of J/ψ and ψ' production cross sections is plotted as a function of the center of mass energy.

The values of Table 1.1 refer to the measured inclusive J/ψ cross sections that include both direct and indirect production [4].

Basically, all the detected ψ' are native ψ' , i.e. do not come from resonance decay; on the contrary for the J/ψ there is an huge indirect contribution from other states. About $(55 \pm 5)\%$ of the ψ' decay into $J/\psi + X$ so the measured J/ψ are contaminated by $\approx 8\%$ events coming from ψ' decays and $\approx 40\%$ from χ_c decays.

From these values one can disentangle the different sources subtracting the feeds to J/ψ from the decays of ψ' and χ_c resonances. With a simple calculation it can be seen that for every produced ψ' there are ≈ 2.9 produced J/ψ and ≈ 3.7 χ_c that decay into $J/\psi + X$.

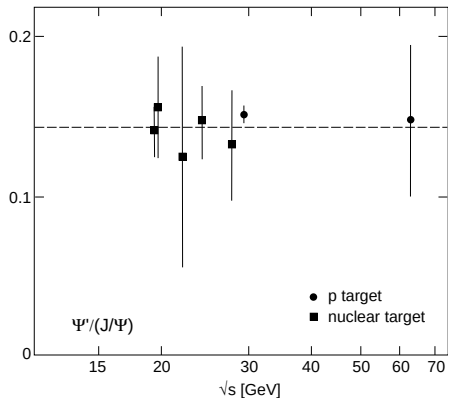

Figure 1.2: The ratio of J/ψ and ψ' production cross sections is plotted as a function of the center of mass energy.

1.2.2 The "Colour Octet" model

Another model used in describing the J/ψ hadro-production is the so called "Colour Octet" model. In this model both the J/ψ and the ψ' are produced as a coloured octet state $(c\bar{c})_8$. The $c\bar{c}$ state propagates in the medium together with a collinear gluon which in the end is absorbed to form a colourless $(c\bar{c})_8\, g$ state.

The basis of the colour octet model is that any quark-antiquark bound state is in reality a superposition of the basic $q\bar{q}$ state plus fluctuations involving in addition one or more gluons:

$$|J/\psi\rangle = a_0\,|(c\bar{c})_1\rangle + a_1\,|(c\bar{c})_8\, g\rangle + ... \tag{1.2}$$

i.e. a pure $c\bar{c}$ colour singlet, plus a component consisting of a colour octet plus a gluon and so on, requiring that the overall colour state to be a colour singlet.

In this model the $(c\bar{c})_8\, g$ can be seen as a sort of universal pre-resonance state that, later, gives one of the possible final states. In this framework a $c\bar{c}$ pair can generate a J/ψ after having neutralised its colour with the collinear gluon.

A very important feature of this model is that the mechanism of the interaction of the two coloured states with the nuclear medium is able to explain with good accuracy the measured nuclear absorption.

1.3 Experimental p-p data

The nucleon-nucleon J/ψ production cross section depends on the center of mass energy $\sqrt{s}$ of the protons, the momentum fraction x_F in the center of mass system and the transverse momentum p_T of the produced J/ψ .

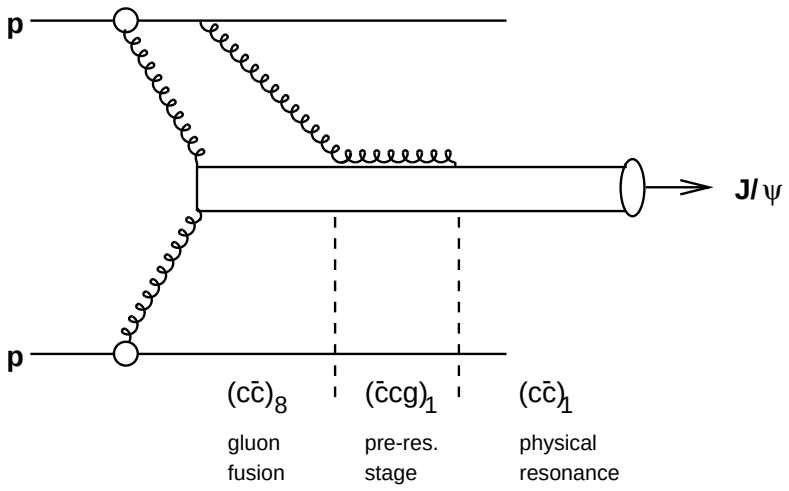

Figure 1.3: J/ψ production in p-p collisions.

The integrated cross section for $pp \to J/\psi + X$ can be parametrised as:

$$\sigma_{pp\to J/\psi+X}\,(s, x_F \geq 0) = \sigma_0 \left(1 - \frac{M_{J/\psi}}{\sqrt{s}}\right)^n \tag{1.3}$$

with $\sigma_0 = 638 \pm 104$ nb and $n = 12.0 \pm 0.9$, for a proton beam [7]. This parametrisation, called "Schuler parametrisation", well describes the production cross sections for $\sqrt{s} < 60$ GeV, as shown in Figure 1.4.

It must be noted that, within this range, this parametrisation agrees with the colour evaporation model calculations [4].

1.4 J/ψ production in proton-nucleus interactions

The nuclear target dependence of hard processes, including J/ψ production is usually parametrised as a power law:

$$\sigma_{pA} = \sigma_{pp}\, A^{\alpha} \tag{1.4}$$

The exponent α implicitly contains all nuclear effects, both in the final state (absorption or dissociation) and in the initial state (nuclear modifications of the parton distribution functions).

In case there are no initial state effects, the case $\alpha = 1$ is for a particle that once produced does not interact with the surrounding medium. This is true for

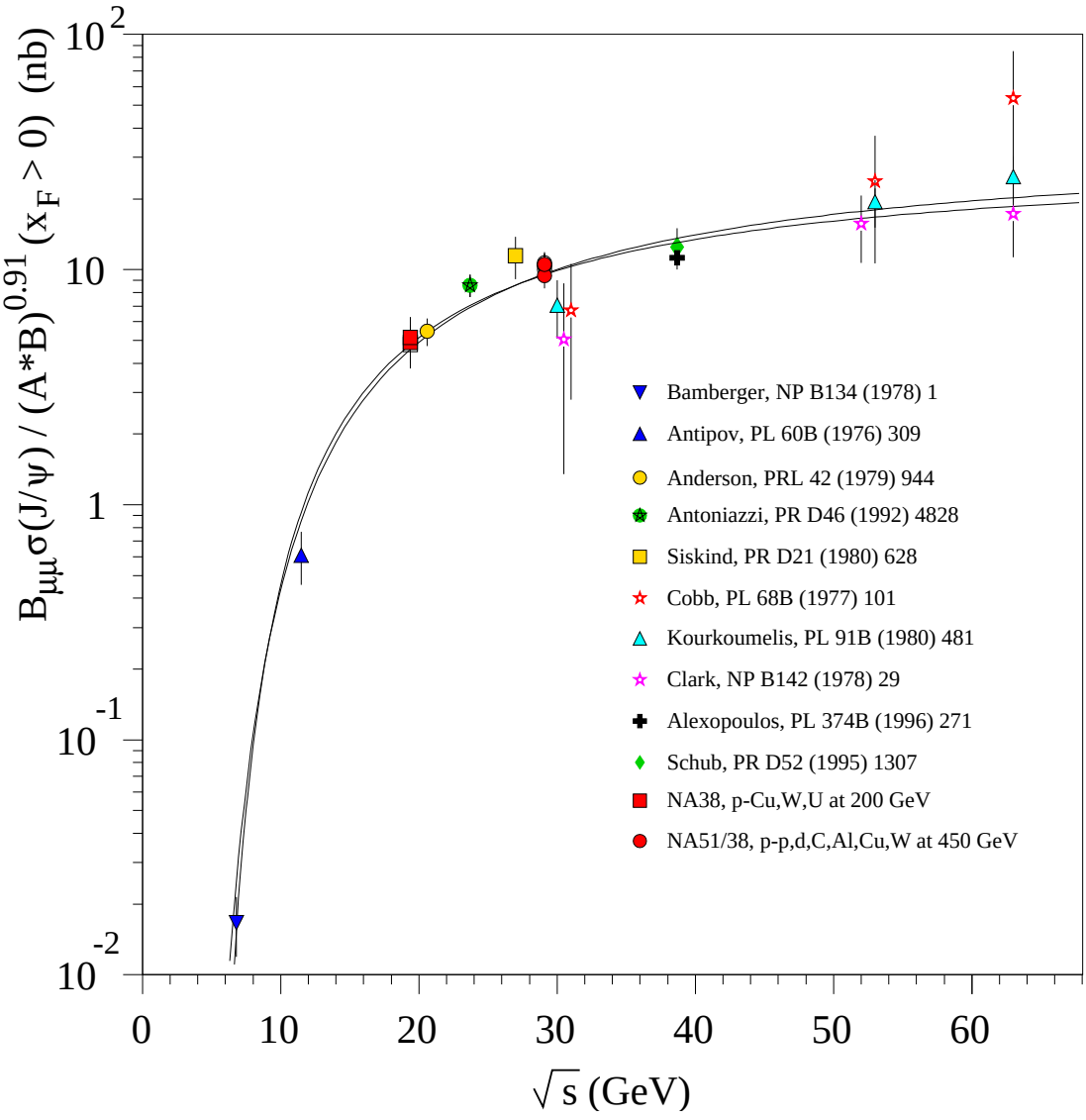

Figure 1.4: Experimental energy dependence of J/ψ production in p-p collisions, The solid line represents the Schuler parametrisation. The nuclear dependence is parametrised with $\alpha = 0.91$.

example for muons pairs produced in the Drell-Yan process but it's not true for the J/ψ .

In fact the J/ψ , being an hadron, strongly interacts with the surrounding medium. The expected α is therefore smaller than 1.

Different experiments measured the $\alpha_{J/\psi}$ in proton-nucleus collisions. Unfortunately the α values only marginally agree with each other. Moreover when p-p data are considered together with p-A data, the resulting α value is often inconsistent with a fit to the proton-nucleus data only. This lead some authors to exclude the p-p points in the calculation of the nuclear dependence [4], [5]. A careful measurement, with small statistic and systematic error, would therefore be of the greatest importance.

In fact, the measured α value can be used to extract an effective cross section of the J/ψ with the nuclear matter. We must however take into account that the J/ψ behaviour should be corrected for the contribution of other hadronic resonances that decay into $J/\psi + X$. This is particularly true for the χ_c contamination.

1.5 J/ψ suppression

In ion-ion collisions, as well as in proton-nucleus collisions, various phenomena may induce a suppression of the expected J/ψ yield. Basically we have effects expected to occur in A-A collisions only (1.5.1) and other which can occur in p-A collisions already.

In the following sections these effects and their influence on J/ψ suppression are discussed.

1.5.1 J/ψ suppression by a Quark Gluon Plasma

In 1986 Matsui and Satz proposed the J/ψ suppression as a signature of the QGP formation [1]. This idea is based on an analogy between "Debye screening" in classical electrodynamics and colour screening in QCD.

To describe the colour screening effect we can study the J/ψ as a two body system, composed by a quark and an anti-quark.

At zero temperature, or otherwise in an isolated system, bound states of heavy quarks can be described by a non relativistic potential with a confining term and a Coulomb-like term

$$V(r, T = 0) = \sigma\, r - \frac{\alpha_c}{r} \tag{1.5}$$

where r is the distance between the 2 quarks, $\sigma \approx 0.192\,\mathrm{GeV}^2$ and $\alpha_c = 0.471$ (in this formula is assumed $\hbar = c = 1$) [3].

The binding potential increases with growing distance between the constituent quarks. This is the reason why quarks are confined inside hadrons in ordinary matter. When the density or the temperature of the hadronic matter is increased a phenomenon similar to Debye screening takes place.

In fact, for electromagnetic interactions, in a dense medium the Coulomb potential between two electric charges, for example a nucleus and an electron, is screened by the presence of an high density of positive and negative charges:

$$V(r) = -\frac{e}{r} \rightarrow -\frac{e}{r} exp\left(-\frac{r}{r_D}\right) \tag{1.6}$$

where r_D is the Debye radius (or Debye length or plasma length) that is proportional to $1/\rho$, where ρ is the density of the medium. This is a measure of the distance over which the Coulomb attraction can have an effect.

If the distance between the two opposite charged particles is greater than r_D the two can not feel anymore their mutual attraction. A bound state can not exist anymore and the bulk of particles behaves like a plasma.

For the same reason, in a system bound by strong interactions, the attraction between two quarks may be reduced, due to colour screening, in a high temperature and density medium.

The "free" inter-quark potential is then modified to:

$$V(r,\, T) = \frac{\sigma}{\mu(T)}\left(1 - e^{-\mu(T)\, r}\right) - \frac{\alpha_c}{r} e^{-\mu(T)\, r} \tag{1.7}$$

where $\mu(T) = 1/r_c$ is the screening mass and r_c is the screening radius.

When r_c becomes small the potential goes to zero and the two quarks can not be bound into an hadron any more.

1.5.2 J/ψ suppression by hadrons

The effect described in the previous section is expected to occur in case of colour deconfinement. However there are two conventional hadronic effects that may destroy the pre-resonant J/ψ state or the already formed J/ψ . In fact, once the $c\bar{c}$ pre-resonant state is produced, it may be split by the interactions with the surrounding nuclear matter or it may as well interact with secondary particles produced in the same collision and moving with the $c\bar{c}$ pair.

These two effects occur at different stages of the life of the $c\bar{c}$ pair: nuclear interactions take place before the $c\bar{c}$ pair escapes from the interaction region where it was formed. In the framework of the colour octet model, the interaction can take place both with the $c\bar{c}$ pair and with the collinear gluon.

After a time of the order of $0.3 \cdot \gamma\,\mathrm{fm/c}$ the $c\bar{c}$ pair hadronizes. If the formation time is long enough all the hadronic resonances are formed outside the nuclear medium. Afterwards, in nucleus-nucleus collisions, the resonance moves in an environment similar to a hadron gas and can be further dissociated.

Nuclear absorption

The nuclear absorption is present in all the models trying to describe J/ψ suppression. In p-A collisions the pre-resonance absorption is the only relevant process to invoke in order to understand the experimental results while in A-B collisions it just represents one of the suppression mechanisms.

The probability that the $c\bar{c}$ pair survives the interactions with the nuclear matter is the product of the survival probabilities for interactions with the target nucleons and, for A-A collisions, with the projectile nucleons.

Since the J/ψ travels through the surrounding nucleons, an appropriate variable to parametrise the measured J/ψ yield is the number of nucleons it can potentially interact with. This number can be calculated as the product ρL , where ρ is the average nuclear density and L is the length of nuclear matter the $c\bar{c}$ state traverses while escaping from the interaction region. The L variable is a relativistic invariant quantity (just as cross sections are).

As a first approximation the charmonium survival probability can therefore be parametrised as $exp(-\sigma_{abs}\rho L)$.

Dissociation by comovers

Comoving secondaries, formed after $\tau_0 \sim 1-2$ fm may also scatter with the fully formed resonances. In fact the typical formation time of a J/ψ from a colour octet state is less than τ_0 , so that the hadron that interacts with comovers is the final charmonium state.

The resonance, say the J/ψ , and the hadrons will interact via the inelastic reaction

$$J/\psi + h \rightarrow D\overline{D} + X \tag{1.8}$$

inducing a suppression of the produced J/ψ .

The survival probability of the J/ψ depends on the comover density at every stage of the evolution of the system $\rho(\tau)$, on the J/ψ cross section with comovers $\sigma_{\psi\, co}$ and on the relative velocity between comovers and J/ψ .

A comover contribution could in principle be present even in p-A collisions. In that case the resulting α dependence would be the sum of the two contributions

$$\alpha_{eff} = 1 - (1 - \alpha_{nucl.}) - (1 - \alpha_{co.}) \tag{1.9}$$

where $\alpha_{nucl.}$ is the A dependence in case there are only nuclear absorption effects and $\alpha_{co.}$ the same for comover effects. The two contributions probably may be separated in near-threshold $\overline{p}A$ or γA reactions [4].

Some of the calculations based on comovers try to explain the J/ψ suppression pattern, from p-A to A-A collisions, without requiring the onset of a phase transition of nuclear matter in a deconfined medium. They describe successfully the NA50 J/ψ data from p-A interactions to central S-U interactions but fail in the description of Pb-Pb data [6].

1.6 J/ψ and ψ' cross sections

Another interesting quantity in the study of the nuclear dependence of charmonium production is the ratio between ψ' and J/ψ cross sections.

If the formation time of the resonant state is long enough to allow the $c\overline{c}$ pair to escape from the nucleus, a constant value is expected. If, on the contrary, some of the J/ψ and ψ' are already formed within the nuclear medium, then the two resonances may have different interaction cross section with nuclear matter because of their different binding energy. Therefore a dependence on the target mass number is expected.

1.7 The Drell-Yan

The J/ψ production is often given as a ratio with respect to the Drell-Yan process. I give in this section the main features of this process.

At leading order the Drell-Yan production of lepton pairs is given by the annihilation of a quark and anti-quark of the same flavour in a hadron-hadron interaction. This produces a virtual photon that forms a lepton pair. Figure 1.5 is a representation of the DY process at the leading order.

The elementary cross section for the process

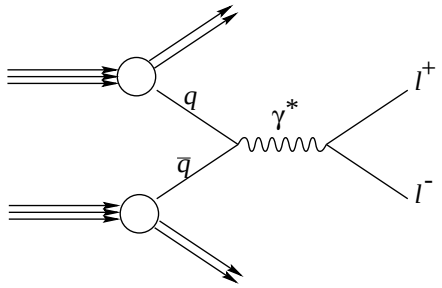

Figure 1.5: The Drell-Yan process is a $q\overline{q}$ annihilation process in a nucleon-nucleon collision that leads to the production of a lepton pair.

$$q_i\overline{q_i} \rightarrow \gamma^* \rightarrow l^+l^- \tag{1.10}$$

is

$$\left.\frac{d\sigma}{d\Omega}\right|_{cms} = \frac{4}{16}\alpha^2\frac{e_i^2}{M^2}(1+\cos^2\theta) \tag{1.11}$$

and once integrated over the solid angle can be written as

$$\sigma_i(q_i\overline{q_i} \rightarrow \gamma^* \rightarrow \mu^+\mu^-) = \frac{4}{3}\pi\alpha^2\frac{e_i^2}{M^2} \tag{1.12}$$

The two quarks have the same flavour "i". e_i is the electric charge of the quarks (e_u = +2/3, e_d = -1/3, ...), α is the structure constant and M is the mass of the virtual photon (or the invariant mass of the lepton pair in which it decays). If we take into account the probability of finding the quark and the anti-quark "i " in the two colliding hadrons, in the framework of the parton model the cross section may be written as:

$$\frac{d^2\sigma}{dx_1dx_2} = \frac{1}{3}\frac{4\pi\alpha^2}{3M^2}\sum_i e_i^2[f_i^A(x_1)\overline{f_i^B}(x_2) + \overline{f_i^A}(x_1)f_i^B(x_2)] \tag{1.13}$$

where the colliding parton of projectile (A) carries a fraction x_1 of the momentum of the hadron and the parton of the target (B) carries a momentum fraction x_2 . $f_i^H(x_j)\,dx$ represents the probability of finding the parton of type i in the hadron H , carrying a longitudinal momentum fraction between x_j and $x_j + dx_j$ of the total hadron momentum. The f_i are called parton distribution functions (PDFs). The factor 1/3 is related to colour.

Perturbative QCD adds to these elementary parton cross section the contributions from other sub-processes. The corrections to the 1.13 with the leading order approximations (LLA) lead to:

$$\frac{d^2\sigma}{dx_1 dx_2} = \frac{4\pi\alpha^2}{9M^2} \sum e_i^2 [f_i^A(x_1, Q^2)\overline{f_i^B}(x_2) + \overline{f_i^A}(x_1, Q^2) f_i^B(x_2, Q^2)] \tag{1.14}$$

Q^2 is named "scale" and $Q^2 = -q^2 = M^2$ is the transferred four-momentum.

These redefined PDFs are extracted from deep inelastic scattering data.

The LLA cross sections underestimates the experimentally measured DY cross section by a factor ≈ 2 . This factor

$$K^{DY} = \frac{measured\, cross - section}{Leading\, Log.\, prediction} \tag{1.15}$$

is usually known as "DY K-factor". It is found to be independent from the invariant mass of the DY pair above 1.5 GeV and with no energy dependence at the currently accessed energies. The K^{DY} can depend, to a certain extent, on the particular set of PDFs used in the calculations.

Chapter 2

The experimental apparatus

In this chapter the NA38, NA50 and NA51 experiments will be briefly described and the differences between the setups used in different periods of data taking will be explained.

2.1 Introduction

The NA50 experiment studies the production of muon pairs in collisions of high intensity relativistic proton or ion beams with various fixed targets.

These events come from various sources: the decay of pions and kaons, the decay of hadronic resonances (ϕ , ρ , ω , J/ψ , ψ'), the decay of charmed mesons and from hard scattering processes.

The high mass resonances have very small cross sections (of the order of a few nb/A for the J/ψ in collisions of a 450 GeV/c proton beam). This required the construction of a detector capable to deal with high beam intensities, having a good geometric acceptance and with a fast selective trigger.

The heart of the NA50 experiment is the NA10 muon spectrometer completed with various detectors and beam monitors.

During heavy ion runs the experiment is equipped with three centrality detectors providing redundant and complementary information about the impact parameter. They provide a precise determination of the geometry of each collision and allow to investigate the dependence of dimuon production from this variable.

The experiment is installed at CERN, the European Laboratory for Particle Physics, in the North Area of the SPS accelerator complex. The experimental area is dedicated to high intensity proton and ion beams.

A schematic view of the NA50 muon spectrometer is shown in Figure 2.1.

2.2 Beams

The NA50-NA38 experiments used ion beams from the SPS accelerator, as well as proton beams.

The ion beams used were primary beams of Deuteron, Oxygen, Sulphur at the energy of 200 A $\cdot$ GeV and Lead at the energy of 158 A$\cdot$ GeV. This corresponds to 400 GeV/c momentum delivered for each charge. The energy uncertainty is about 0.1%. The proton beams have the maximum energy available from SPS that is 450 GeV. The NA38 experiment used also 200 GeV secondary proton beams that have an energy uncertainty of about 0.3%. These were obtained from the interaction of the primary proton beam on a Beryllium target. The outcoming particles were selected in momentum and charge tuning in a proper way the beam line after the target.

The study of the same collisions both with 450 GeV and 200 GeV proton beams allowed to estimate the appropriate scaling factor to compare the 200 GeV ion data with the 450 high intensity proton data.

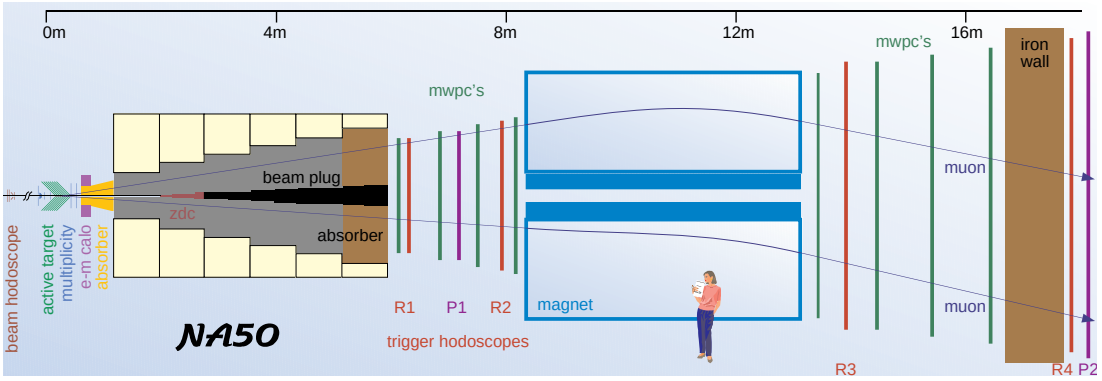

Figure 2.1: The NA50 muon spectrometer

Beams from the SPS are pulsed, the total cycle length is 14.4 s with an effective spill of 2.37 s for proton beams and 19.2 s with an effective spill of 4.8 s for ion beams.

The beam intensities are different for proton-nucleus and nucleus-nucleus data taking. The maximum beam intensity was $\approx 5\,10^7$ lead ions per burst during NA50 data taking. In NA38, during S-U data taking the beam intensity was around 10^8 S ions per burst. During Pb-Pb ion data taking the beam intensity is limited by the operation of the detectors that are placed on the beam line. For the proton-nucleus data taking the maximum intensity is imposed by chamber occupancy which causes a degradation of the reconstruction efficiency. This is 100% at low (10^8 p/burst) intensity and falls down when higher ($\simeq 2.5\,10^9$ protons/burst) intensity is used.

2.3 Beam detectors in proton nucleus data taking

2.3.1 The beam telescopes

Three telescopes named "Jura", "Saleve"[1] and "Vertical" are placed at the target level. The axe of each telescope is at 90° with respect to the beam axis and is pointing to the target.

Every telescope is made of three scintillators and is protected by a shield of paraffin and iron. The telescopes "Jura" and "Saleve" are placed in the horizontal plane, a few meters away from the target region.

These telescopes measure a small fraction of the interaction products and have a very low counting rate compared to the beam intensity. Because of the high beam intensity no scintillating counter can be placed on the beam to define the

[1] From the names of two massifs near the laboratory

trajectory so the stability of the beam impact point on the target is monitored with this three telescopes.

2.3.2 The argon counters

During the proton runs three ionization chambers filled with argon allow to measure the beam intensity. The ionization current is integrated during every burst and the total charge collected is proportional to the number of crossing protons.

The argon counters were calibrated with low intensity proton beams. The stability of the calibration constant has been verified with different techniques.

The integrated current, expressed in ADC channels, will be referred to as: "number of argonium". The calibration constant is 6408[2] protons per argonium measured by ARGO1 with an uncertainty of about 4% [3].

2.4 The beam hodoscopes

During nucleus-nucleus data taking two hodoscopes are placed on the beam line. The NA50 Beam Hodoscope (BH) is placed $22\,m$ upstream the target in a place where the beam is defocussed ($\sigma_x \simeq 0.8$ mm and $\sigma_y \simeq 6$ mm). It consists of 16 quartz blades detecting beam particles by Cherenkov effect. Each blade is read by a photo-multiplier and intercepts the same fraction of the beam. The detection efficiency is better than 99% and the maximum intensity on the BH is $\approx 10^8$ particles per burst. The BH signals are read with a 20 ns gated ADC and allow to reject in the analysis all the events where more than one ion cross the BH in this time window (this is the so called beam pile-up rejection). This is of paramount importance to have a correct measurement of the centrality.

Two sets of scintillator blades named BHI and BHIN are placed outside the beam path, just after the BH, and are used to reject events where the incoming ions interacted in the BH.

2.5 The target system

During the heavy ion data taking a segmented target is used. It has been designed to provide easy determination of the vertex and to increase the luminosity. Each

[2]The argon counters have been recently re-calibrated and this lead to a better estimation of the beam luminosity. The results on absolute cross sections have been upgraded. The results can be found in Appendix A.

[3]See Section 5.7 for details.

Target	A	λ_i $\left(\frac{g}{cm^2}\right)$	ρ $\left(\frac{g}{cm^3}\right)$	X_0 (cm)	L (cm)	L eff. (cm)	L eff. (λ_i)
Be	9.01	75.2	1.85	35.3	13.	11.1	0.27
Al	26.98	106	2.70	8.9	12.	10.3	0.26
Cu	63.55	135	8.96	1.43	7.5	5.91	0.39
Ag	108	156	10.5	6.37	7.5	5.89	0.40
W	183.8	185	19.1	0.35	4.5	3.6	0.37

Table 2.1: Target characteristics for the proton-nucleus data taking of 1998, 1999 and 2000. L eff. take into account beam attenuation in the target

sub-target is followed by two radiation resistant quartz blades that identify the target where the interaction takes place. Eventually, after a peripheral collision, a projectile fragment can be produced and it can interact in another sub-target. The quartz blades can be used to reject this kind of event.

Just before the first target a couple of blades identifies interactions of lead on air and a couple of anti-halo detector are used to identify the ions out of a 3 mm diameter.

During the proton-nucleus data taking, to increase the luminosity, a single thick target of the desired material is employed.

In the present analysis were used data taken on five targets that are listed in Table 2.1.

2.6 The hadron absorbers

There are two hadron absorbers. One is placed downstream the target, before the muon spectrometer and one is placed at the end of the spectrometer, before the last trigger hodoscope.

The first hadron absorber, see Fig. 2.2 is designed to stop the collision products other than muons with minimum angular deflection on the muon tracks. It is composed of various materials that are listed in Table 2.2 (together with the purpose of each component). It is divided into four zones.

The plug, in the central part, absorbs the beam particles which did not interact in the target. In NA38 it was a cone of W and U. In NA50 the first 80 cm of W have been replaced by 65 cm of Ta, corresponding to the Zero Degree Calorimeter (ZDC, see later) and 15 cm of air.

The plug is surrounded by carbon cylinders for a total length of 4 m ($10.5\,\lambda_i$) completed with 80 cm of iron cylinders ($4.8\,\lambda_i$) covering the total acceptance of the spectrometer. This part acts as a muon filter. The choice of carbon is

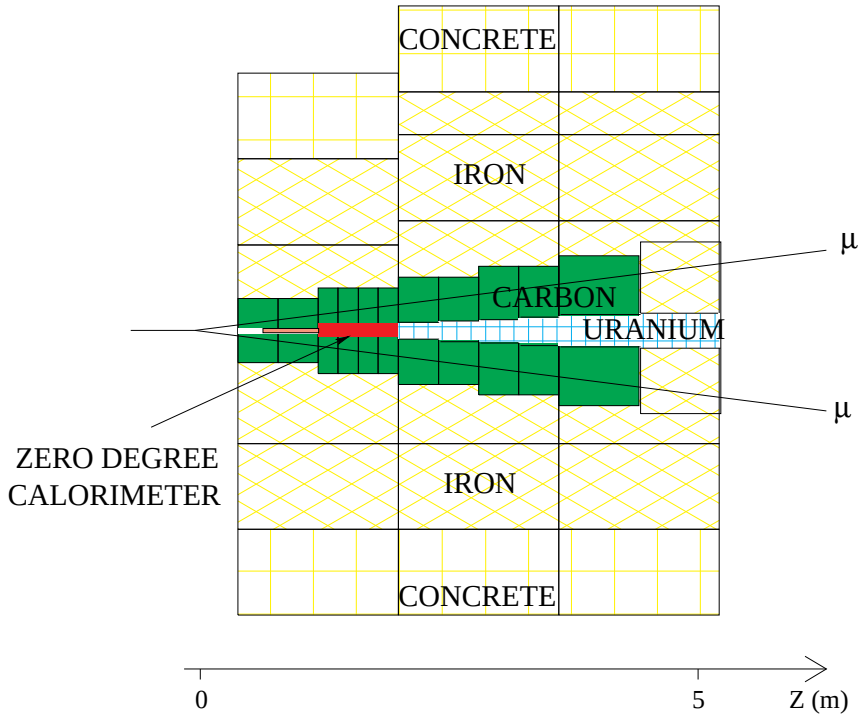

Figure 2.2: The NA50 hadron absorber

a compromise between the filtering efficiency and the limitation of the multiple scattering effects. This central part is surrounded by iron blocks and concrete blocks that are outside the acceptance of the spectrometer.

The 80 cm thick iron wall after the carbon cylinders is used to increase the filtering power.

To be able to exit from the absorber a muon shall have at least 4 GeV/c momentum.

Before the main absorber, a pre-absorber is placed to stop pions and kaons before they can decay into muons: 59.1 cm BeO or 60.8 cm Al_2O_3 . During ion-nucleus data taking the absorber BeO is used. During the NA50 proton-nucleus data taking, the EMCal is removed and the Al_2O_3 is used instead. The BeO covers the pseudo-rapidity range $2.42 < \eta < 4.43$, while the Al_2O_3 the range $2.17 < \eta < 4.93$.

The second absorber at the end of the muon spectrometer is a 1.20 m thick iron wall that stops the surviving hadrons in order to reduce the number of fake triggers.

Material	Aim	Length(cm)	λ_i (g/cm^2)	ρ (g/cm^3)	X_0 (g/cm^2)
BeO	pre-abs.	59.1	84.9	2.81	41.30
Al_2O_3	pre-abs.	60.8	98.7	3.82	27.90
C	main abs.	400.0	86.3	1.93	42.70
Fe	main abs.	80.0	131.9	7.20	13.84
Air	plug	80.0	90.0	$1.205\,10^{-3}$	36.67
Ta	ZDC (plug)	65.0	197.95	16.6	6.83
W	plug	80.0	185.0	17.8	6.76
U	plug	320.0	199.0	18.95	6.00

Table 2.2: Characteristics and use of the absorber and pre-absorber materials

2.7 The muon spectrometer

2.7.1 The toroidal field magnet

The NA50 magnet, see Figure 2.3, is located downstream the target, after the hadron absorber. It has a toroidal shape with an hexagonal symmetry and is composed of 6 equal sextants.

It's 4.8 m long and has a 4.1 m diameter. The open zone has an internal radius of 29.5 cm and an external radius of 1.5 m. A central hole of 9.5 cm is delimited by the iron sectors. The angular acceptance is between ~ 35 mrad to ~ 115 mrad.

The current circulates into 6 coils mounted on 6 iron supports. The magnet is pulsed with a direct current that is synchronised with the SPS spill. It can range up to 10000 A.

The resulting field has a toroidal shape in the azimuthal direction:

$$\int \overrightarrow{B}(r)\,dz = \frac{B_0}{r}\overrightarrow{u_\varphi} \tag{2.1}$$

where:

- r is the distance from the beam axis
- $\overrightarrow{u_\varphi}$ is the azimuthal versor
- B_0 is a constant whose value is 0.219 T m in NA38 where the magnet current was set to 4000 A, 0.383 T m in NA50 where the nominal current is 7000 A in order to improve mass resolution and background rejection and 0.550 T m for the 10000 A current used in NA38 p-A data taking.

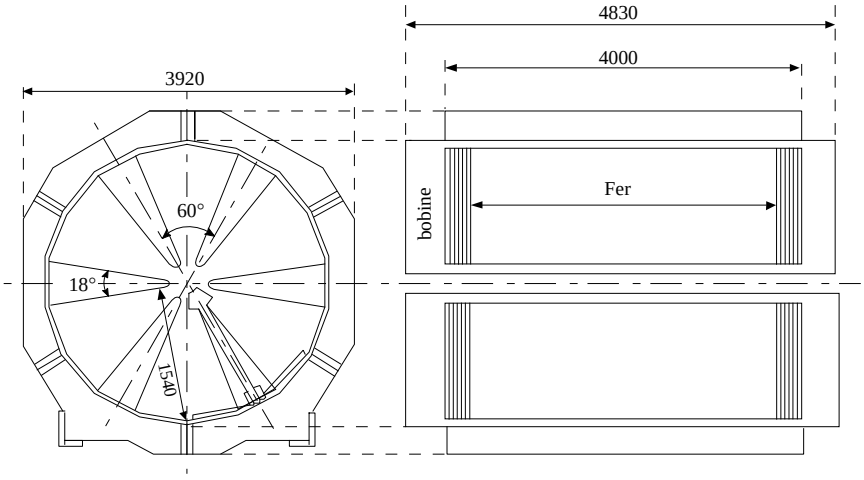

Figure 2.3: The NA50 magnet

All the particles that arrive in an azimuthal plane (as the particles coming from the target) are deflected by the toroidal field in this same plane. For these tracks the deflection is proportional to the field intensity and the momentum

$$\Delta\theta \propto \frac{B}{p}$$

but since

$$B \propto \frac{1}{r}$$

where r is the distance from the magnet axis, then

$$\Delta\theta \propto \frac{1}{p\,r} \propto \frac{1}{p_t}$$

The deflection angle can be calculated as

$$\Delta\vartheta \simeq \frac{qB_0}{p_t} ln\left(\frac{z_2}{z_1}\right) = \frac{b}{p_t} \tag{2.2}$$

where:

- $z_1 - z_2$ is the magnet length and the z_1 and z_2 are computed from the target position.

Figure 2.4: Picture of NA50 muon spectrometer

- b is approximately 0.023 rad GeV/c in NA38 for a 4000 A current and 0.0402 rad GeV/c in NA50 for a 7000 A current.

To be free from systematic effects due to differences between the sextants, the sign of the magnetic field is reversed during the data taking period. Half of the statistics is collected with one field and the other half with the other polarity.

2.7.2 The trigger hodoscopes

Four scintillator hodoscopes form the trigger system. Two of them (R1 and R2) are located upstream the magnet and the other two (R3 and R4) are downstream perpendicular to the beam axis. The hodoscope R4 is at the end of the spectrometer after the 120 cm thick iron wall.

The hodoscopes have an hexagonal symmetry and are divided into six sextants that correspond to the sextants of the magnet. Each sextant is composed of scintillator blades in number of 30 (R1 and R2), 24 (R3) and 32 (R4) (numbered from inside to outside).

The hodoscope R2 is homothetic to the hodoscope R1 with respect to the target centre. The width of scintillator blades varies from 1.05 cm to 3.05 cm for hodoscope R1 and from 1.25 cm to 3.85 cm for hodoscope R2. In hodoscopes R3 and R4 all the scintillators have the same width of 5.5 cm.

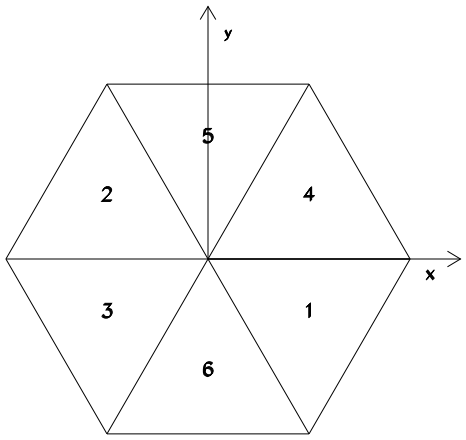

Figure 2.5: Sextants numbering convention, beam is coming out along z axis, y axis is upwards

Sextant by sextant each scintillator $\mathrm{R1}_i$ is associated with a scintillator $\mathrm{R2}_i$. The coincidence $\mathrm{R1}_i * \mathrm{R2}_i$ selects tracks coming from the center of the target.

Each scintillator blade of hodoscope R1 is read by a photo-multiplier on one side and the corresponding scintillator in hodoscope R2 is read on the opposite side. The coincidence of the two signals in a mean timer gives a signal with good timing properties.

Because of the extension of the target region and to increase the acceptance at the low masses, the condition $\mathrm{R1}_i * \mathrm{R2}_{i-1}$ is also accepted.

The occurrence in a given sextant of one of the two previous conditions is called "V"

$$V_i = \mathrm{R1}_i * \mathrm{R2}_i + \mathrm{R1}_i * \mathrm{R2}_{i-1} \tag{2.3}$$

The V_i signal enters in a coincidence matrix together with the signals of the last two hodoscopes. This matrix verifies that the hits in the two backwards telescopes are compatible with the forward track and give a first estimation of the transverse momentum of the track. This condition is named:

$$V_i * p_t$$

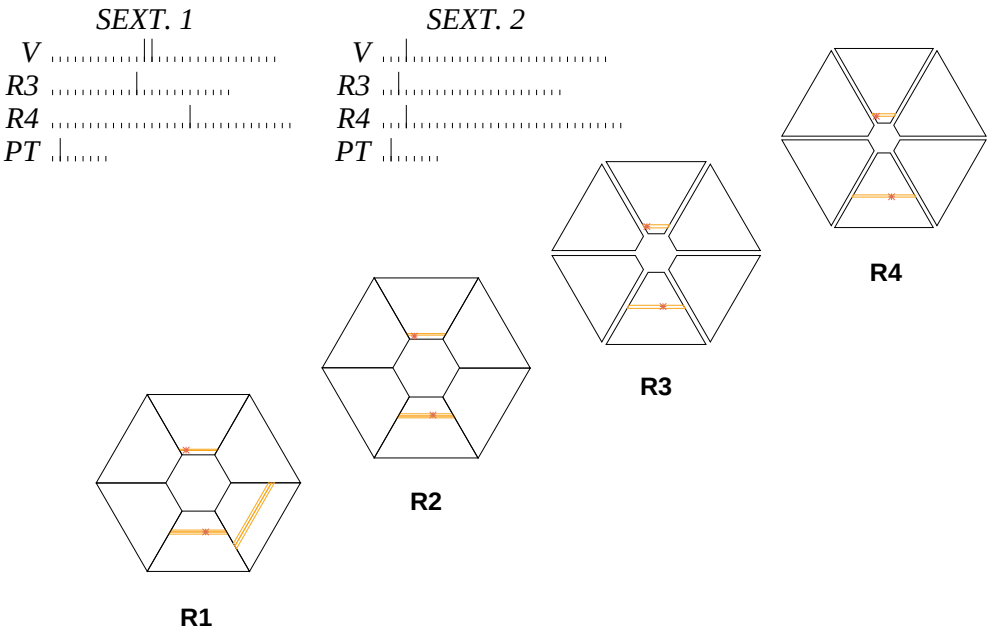

Figure 2.6: Hits on the trigger hodoscopes of a typical dimuon event in low intensity runs. Information is displayed about the signals that generated the trigger in the coincidence matrix and the resulting p_t estimation.

The occurrence of at least two of these conditions in different sextants give the standard dimuon trigger.

2.7.3 The acceptance function

The presence of the hadron absorber and of the iron wall as well as the trigger logic give raise to a very particular acceptance function. There is a momentum cut on the single tracks due both to the presence of the hadron absorber and to the magnetic field. High mass dimuons are favoured because they can easily enter into opposite sextants. Low mass dimuons have chance to be triggered only if they have high p_t so that they can enter into adjacent sextants.

The geometric acceptance imposes cuts on the rapidity distribution of the dimuons. Moreover muon pairs with similar momentum are more easily accepted.

The consequences of these characteristics of the apparatus design will be discussed in more detail in Section 3.5.

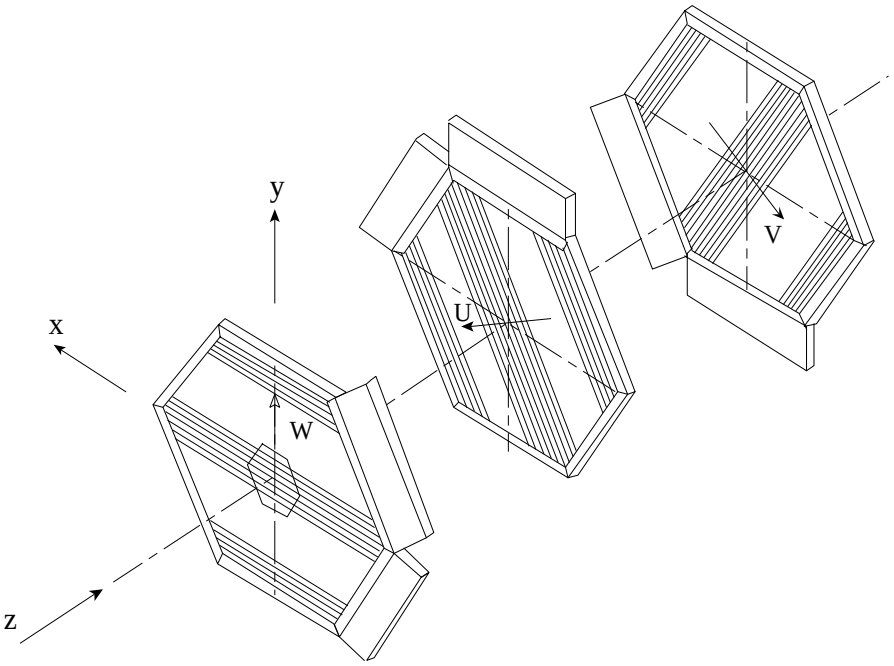

Figure 2.7: The three planes of the NA50 MWPC

2.7.4 The tracking chambers

Eight multi-wire proportional chambers are used to reconstruct the trajectory of the muons. Four are placed upstream the magnet and four downstream. They have an hexagonal symmetry and are made of three wire planes separated one from the other by a 2.2 cm gap. Every plane measures a spatial coordinate in a not-orthogonal reference frame. In the so called w plane the wires are disposed parallel to the horizontal plane (x axis). The other two planes u and v are rotated with respect to the w plane as shown in Figure 2.7.

Wires have a diameter of $20\,\mu m$ and spacing of 3 mm that gives a good resolution on the muon angle (some tenth of a mrad).

The radius of the chambers of the first set is 1.3 m and each chamber has 749 wires, while the radius in the second set is 3 m and each chamber has 1229 wires. The MWPC are fluxed with a mixture of Argon (80%), iso-butane (19.8%) and Freon (0.2%).

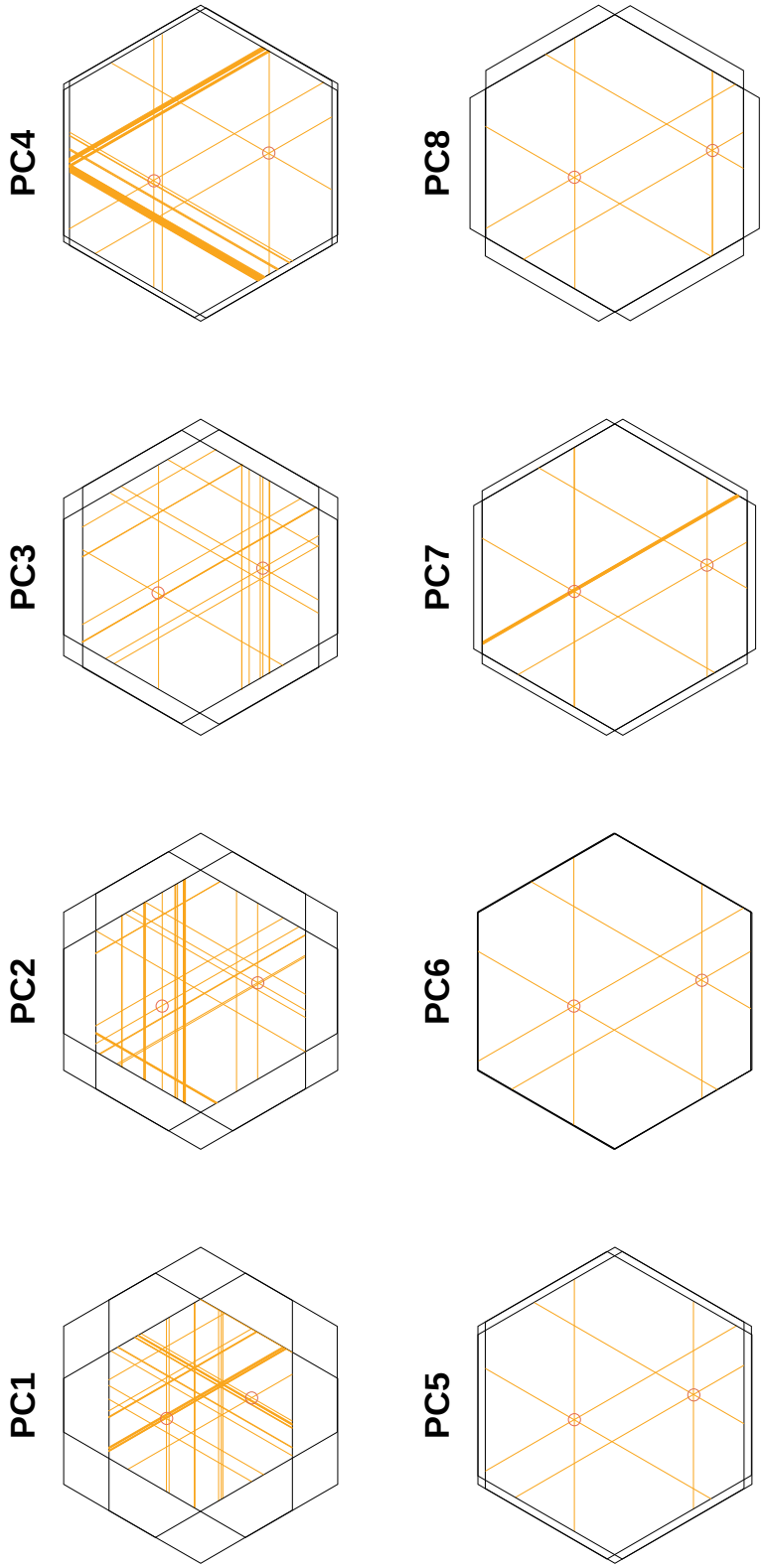

Figure 2.8: Hits in the tracking chambers for a typical dimuon event in low intensity data taking. Fired hits are shown, the closed circles identify the reconstructed track: forward telescope is made by chambers PC1 – PC4 , backward telescope by PC5 – PC8 .

2.7.5 The P1 and P2 telescopes

Two independent scintillator telescopes are used to estimate the trigger efficiency. One is placed before the magnet and the other is placed at the very and of the spectrometer, just after the R4 hodoscope. During special periods of the data taking the magnet field is set to zero and these two telescopes are used to trigger on straight tracks. This independent trigger is used to calculate the trigger efficiency of the whole system.

2.8 Detectors for centrality measurement

During the ion data taking period the NA50 experiment is equipped with three independent detectors that estimate the centrality of the collision: the Zero Degree Calorimeter (ZDC), the Electromagnetic Calorimeter (EMCal) and the Multiplicity Detector (MD). They exploit complementary information about the geometry of the collisions. The MD measurement is strongly correlated with the EMCal one and both are anti-correlated with the ZDC.

In NA38 the collision centrality was measured only by the EMCal.

2.8.1 The Zero Degree Calorimeter

The Zero Degree Calorimeter (ZDC) [11] measures the energy carried by spectator nucleons and beam fragments emitted at very small angles. Depending on the impact parameter a different number of nucleons are affected by the collision. Some of them does not strongly take part in the interaction and their momentum is unchanged: they retain the momentum they had at the moment of the collision (beam momentum plus Fermi motion). From the measurement of the energy carried by these, the impact parameter can be estimated.

The ZDC constitutes the first element of the beam dump being located on the beam axis, 1.65 m downstream from the target. When no interaction takes place it allows to monitor the position of the beam impact point.

The ZDC is a sampling calorimeter made of tantalum slabs with embedded quartz fibres. The hadronic showers produce signals by Cherenkov effect in the quartz fibres that act as well as light guides. This gives the NA50 ZDC an intrinsic response speed (a few ns rise-time) that allows to cope with beam intensities up to 10^7 ions per second. The use of quartz fibres gives to this calorimeter a strong radiation hardness. In Figures 2.9 and 2.10 it is shown the evolution of the ZDC signal and resolution versus the integrated dose in the central part of the calorimeter (that is of the order of a few Grad per month of operation at the NA50 experiment).

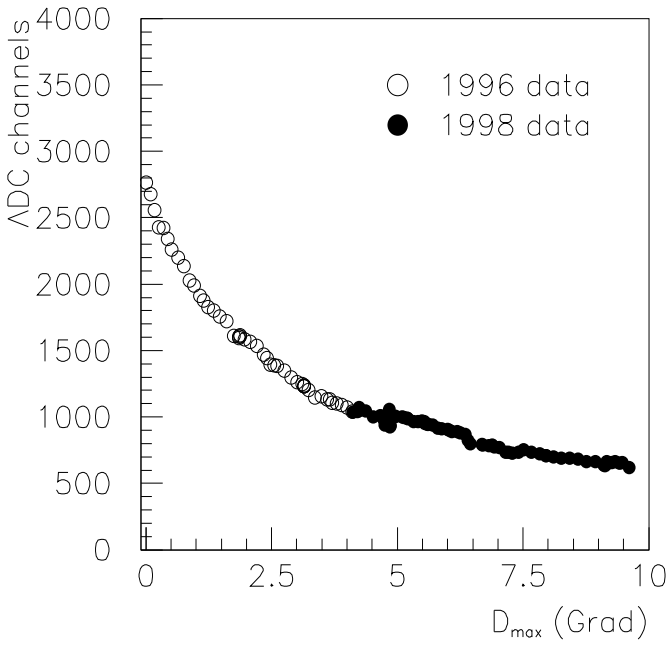

Figure 2.9: Position of the lead peak in the ZDC spectrum as a function of the dose D_{max} absorbed by the detector throughout the 1996 and 1998 data taking period.

The β threshold of Cherenkov light production makes this calorimeter insensitive to radiations coming from nuclear decays and keep the background counts at a low level even after irradiation.

2.8.2 The Electromagnetic Calorimeter

The Electromagnetic Calorimeter is a sampling calorimeter using an alloy of lead and bismuth as showering material and polystyrene scintillating fibres as active material. The fibres have a diameter of 2 mm and are placed parallel to the beam axis. The filling ratio is 1/2. It has hexagonal shape and is divided into four crowns. It is placed $\approx$ 32 cm downstream the central target position. In NA50 it covers the pseudo-rapidity interval $1.1 < \eta < 2.3$ while in NA38 it covered $1.4 < \eta < 4.1$. This shift allowed to reduce the material budget on the path of the muons and helped in improving the mass resolution.

The EMCal measures the energy carried by those interaction products that generate electromagnetic showers: photons (either direct or coming from resonance decay), electrons and positrons. This measurement shows a good anti-correlation with the energy measured by the ZDC. Corrections are made to subtract the contribution of the hadron showers.

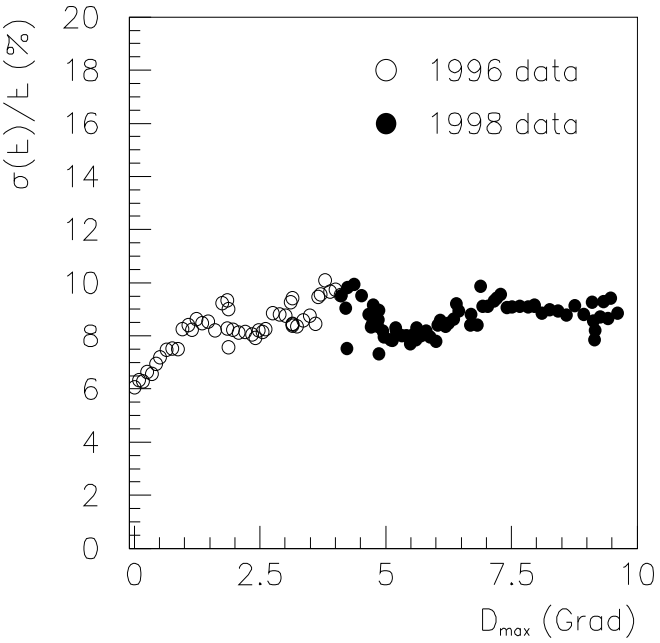

Figure 2.10: Resolution $\sigma(E)/E$ on the lead peak measurement as a function of the dose D_{max} absorbed by the detector throughout the 1996 and 1998 data taking period.

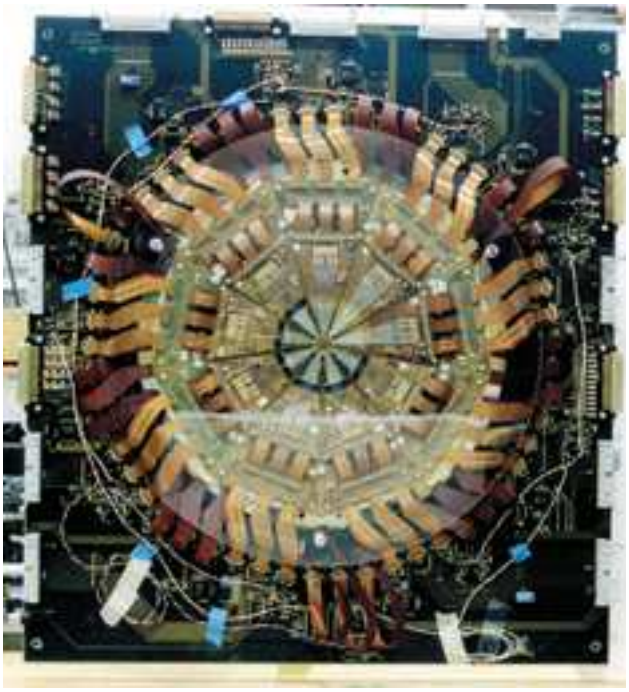

Figure 2.11: One of the two Multiplicity Detector planes.

2.8.3 The Multiplicity Detector

The multiplicity detector measures the number of charged tracks emerging from the collision. The MD is made of two silicon strip detectors organised in two disks each. Each of the disks consists of $\approx$ 7000 micro-strips. A detailed description of the MD can be found in Ref. [12]. In Figure 2.11 one of the detector planes is shown.

Chapter 3

Reconstruction, data reduction and run selection

In this chapter I describe the method used to reconstruct the raw data, then the cuts on single muon tracks and at the dimuon level. Finally the criteria used for run selection are discussed.

3.1 Introduction

Raw data are analysed with a dedicated program called "DIMUREC" that reconstructs the dimuon tracks and calculates all the dimuon physical variables. The reconstruction program also checks the working conditions of the apparatus and provide an estimation of live-time and reconstruction efficiency [10].

3.2 Event reconstruction

3.2.1 Track reconstruction

The reconstruction program selects the starting region for track reconstruction from the patterns of the scintillators that gave the dimuon trigger.

The track reconstruction is done in two steps: first, the half-tracks are reconstructed in the forward and backward spectrometers, then the two half-tracks are associated to form the full tracks.

The reconstruction program first considers the backward spectrometer (after the magnet) where the hit multiplicity is much lower than in the forward one. For a given wire plane each couple of the active wires of the first and the last chambers are used to define a define a road. The intermediate chambers are then considered and the reconstruction program searches for active wires in the road defined by the extreme planes. The same procedure is repeated for the three projections. The associations of the three projections defines a tube whose diameter (road-width) depends on the chamber resolution and is selected at the moment of reconstruction. The track is considered reconstructed if at least three chambers measure a point belonging to that tube.

The same procedure is repeated for each hit pair in the first and last chambers with the conditions that an active wire only belongs to one track.

For the reconstruction of the tracks in the forward spectrometer the same procedure is used. The studied region is however restricted to tracks compatible with the backward track and pointing towards the target.

The tacks are associated at the middle plane of the magnet with a request on the minimum distance between the tracks (less than 3 cm) and on the difference in azimuthal angle ($\Delta\phi < 0.25$ rad). This cut, quite large, allows to accept also some tracks that suffered from multiple scattering, in particular low momentum muons.

3.2.2 Vertex determination

The reconstruction program calculates the impact points of the reconstructed tracks in a plane perpendicular to the beam axis. The barycentre of the impact point is calculated taking into account the errors on each point. The calculation is repeated iteratively in order to find the optimal vertex position.

3.3 Event selection

3.3.1 Geometrical cuts

The main purpose of these cuts is to extract a sample of data with good tracking precision and to reject fake tracks due to reconstruction errors or to coincidences of background tracks.

The reconstruction program performs a fast simulation of the reconstructed tracks on the basis of the calculated momentum of each muon and of the hits on the detectors of the muon spectrometer. The following points are checked:

- a reconstructed track should not cross any iron part of the magnet. These events are discarded because they lead to a low mass resolution because of the additional scattering and energy loss in the iron yoke,
- a "fiducial cut" is applied. It rejects tracks outside the useful active zone of the tracking chambers,
- the hits in the trigger scintillators are simulated and are then compared with the real ones. If the trigger pattern deduced from reconstruction is not compatible with the one written on tape the event is discarded.
- A special cut named "image cut" is applied to all remaining tracks,
- a track quality cut ("global cut") is then applied.

The last two cuts will be described in detail in the following subsections.

3.3.2 The "image cut"

The algorithm relative to this cut changes the sign of the muon and performs a fast simulation of the obtained track[1]. If this new track is not accepted by the apparatus the muon is rejected.

[1] This is equivalent to leave the particle unchanged and reverse the sign of the magnetic field.

This ensures that all muons have the same acceptance independently from their charge. This is essential to perform in a correct way the subtraction of the combinatorial background (see Section 4.8).

In order to be free from possible effects due to inefficiencies in this cut procedure, the sign of the magnetic field is reversed every few runs so that approximately half of the statistics is taken with one sign of the magnetic field and the other half with the opposite.

3.3.3 The "global cuts"

The reconstructed track is projected back to the target. The position along the x and y direction (D_x , D_y) and the distance from the beam axis:

$$DTarg = \sqrt{D_x^2 + D_y^2} \tag{3.1}$$

in the target mid plane are computed.

Typically the calculated distance $DTarg$ is much greater than the beam radius. This is essentially caused by the multiple scattering in the target and in the absorber. In fact, when the muon arrives in the tracking chambers , it has lost some piece of information about its original vertex position and consequently informations about its production vertex are smeared.

Another possibility is that the real interaction point was not in the target but upstream in the beam line or downstream in the hadron absorber. A track whose origin is not the target but some point downstream or upstream the target can obviously show a very large $DTarg$.

Since multiple scattering is proportional to $1/P_\mu$, where P_μ is the muon momentum, it is more convenient to factorise the P dependence and study the $P*DTarg$ distribution.

If the beam is centred on the beam axis the distributions of P_xD_x and P_yD_y are Gaussian, centred on zero and with width σ_x and σ_y . If these distribution are not centred one can calculate the mean value $\mu_x =< D_x >$, $\mu_y =< D_y >$ and use it to obtain the following distribution:

$$Cut_1 = \left(\frac{P\,(D_x - \mu_x)}{\sigma_x}\right)^2 + \left(\frac{P\,(D_y - \mu_y)}{\sigma_y}\right)^2 \tag{3.2}$$

that has the distribution of a chisquare with two degrees of freedom[2].

[2]This is not strictly correct by the statistical point of view. A priori it is not true that the condition $\mu_x =< D_x >$ ensures that$< P_x(D_x - \mu_x) >= 0$. A more correct approach would lead to consider $\mu_x =< PD_x >$ that implies that $< PD_x - \mu_x >= 0$. Practically this effects happens to be negligible because there is no correlation between P and D_x or D_y

For symmetry reasons we have:

$$\sigma_x = \sigma_y \equiv \sigma$$

The coefficients μ_i and σ are computed in different momentum bins in order to take into account possible residual dependencies not properly taken into account in the factorisation. In this calculation only the tracks with invariant mass in the J/ψ region and above are used because this is the region of interest in this work.

For every tracks one can define a "χ^2 probability" to have $\chi^2 \geq Cut_1$:

$$Prob(P * DTarg) \equiv Prob(Cut_1) \equiv \int_{Cut_1}^{+\infty} f(\chi^2)\, d\chi^2 \tag{3.3}$$

where $f(\chi^2)$ is a normalised, integrable χ^2 distribution with two degrees of freedom.

The events with a low χ^2 probability are discarded because most of them come from strongly scattered tracks that worsen the mass resolution or from tracks generated in out of target interactions.

As an example in figure 3.1 the $Prob(Cut_1)$ distribution for p-Al runs is shown. The strongly scattered tracks and out of target events fall in the low $Prob(Cut_1)$ region.

Other cuts on the reconstruction quality are possible and are related to the matching of the reconstructed track at the middle of the magnet. They can help to reduce the number of fake tracks (i.e. two tracks produced by different particles that are associated by the reconstruction routine and considered as a single track).

The half-track reconstructed in the upstream spectrometer is compared with the half-track reconstructed in the spectrometer downstream the magnet. The upward track and downward track are then projected to the middle of the magnet. It's then possible to apply:

- a cut on the χ^2 probability for a the distribution of the distance between the projections of the upward track and downward track,
- a cut on the angular deflection based on the difference between the azimuthal angles of the tracks before and after the magnet. In fact the toroidal field of the magnet preserves the azimuthal angle for tracks contained in the same azimuthal plane (and this is the case for tracks coming from the target).

These two cuts where not used in the present analysis. They are only useful in extremely critic conditions, when the beam intensity is much higher than for the data presented in this work.

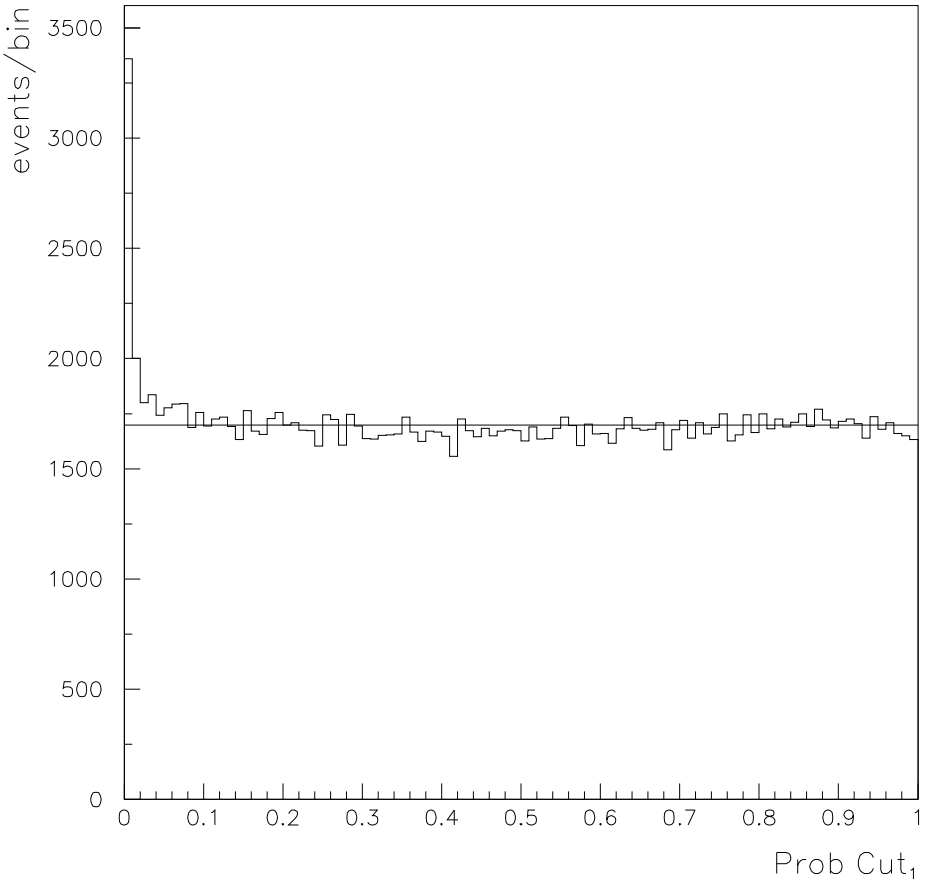

Figure 3.1: $Prob(Cut_1)$ distributions for p Al 1999 data, nominal acceptance and mass of the dimuon greater than 3 GeV.

Cut on $PROB(P*DTarg)$	0%	1%	5%	10%	20%	50%
Accepted events	423	289	225	191	134	39

Table 3.1: Effect of global cuts on empty target events. The accepted events are opposite sign muons integrated on all the invariant mass spectrum within the kinematic window $-0.5 < cos\vartheta_{CS} < 0.5$ and $-0.4 < y^* < 0.6$.

3.3.4 Some technical improvement

The global cut calculation is usually done by the reconstruction program considering 15 bins in the momentum of the muon track. The bin width is 3 GeV so the maximum momentum that is considered is 45 GeV. For each bin the width of the $P*D_x$ and $P*D_y$ is computed taking into account only the gaussian zone and it's then used back in the global cut calculation. As you can see from Figure 3.8 there are some muons with momentum above 45 GeV/c. The reconstruction program puts these muons in the highest momentum bin (which however corresponds to 45 GeV/c only) and calculates χ^2 probability using the parameters of such bin.

This can induce some effects on the quality cuts because leads to an underestimation of the calculated $P*DTarg$. Events with momentum above 45 GeV/c are then less likely to be cut out by the quality cuts.

In order to have a better estimation of the $P*DTarg$ cut variable the number of bins has been increased to 20 so that all tracks up to 60 GeV have the coefficients properly tuned. In this way the high momentum tracks are taken into account more precisely using their real momentum.

The high momentum tracks come mainly from the DY process. This refined calculation of the global cuts, in principle, allows to have a cleaner estimation of this variable in the DY region.

3.3.5 Global cuts and out-of-target contribution

The use of a cut on $PROB(P*Dtarg)$ is useful to reduce the contamination of events that are produced outside the target. These dimuons can be produced in interactions upstream the target, for example in the argon counters, or downstream in the absorber.

In Table 3.1 I show the effect of different global cut levels on the number of accepted events in the opposite sign spectrum for empty target runs.

For events coming from the target one would expect a flat distribution. For empty target events we see that most events are contained in the low $PROB(P*Dtarg)$ region (see Figure 3.2), as expected for a random origin of the track.

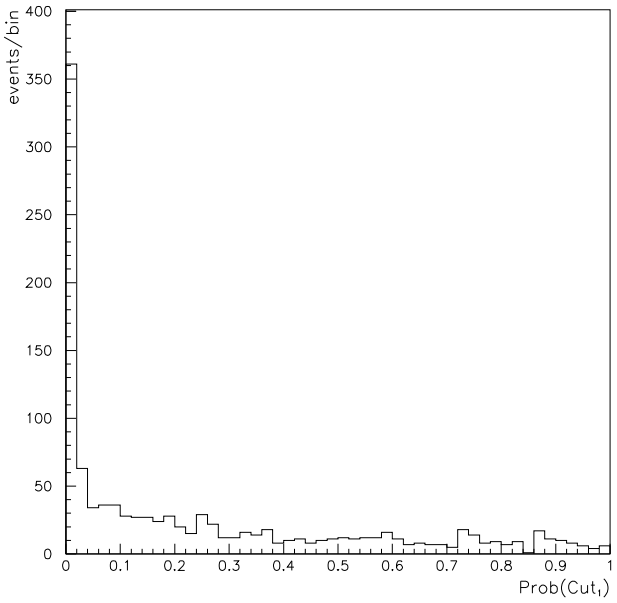

Figure 3.2: $Prob(Cut_1)$ distributions for empty target runs, within the acceptance window $-0.5 < cos\vartheta_{CS} < 0.5$ and $-0.4 < y^* < 0.6$.

In Figure 3.3 the invariant mass of the opposite sign dimuon pair is plotted against the z coordinate of the reconstructed vertex. In the upper plot (a) no global cut is applied while in the lower plot (b) a 1% global cut is used. In the first plot the contribution of out of target interactions is clearly visible. The J/ψ pole in fact has a shadow in the "high mass - low z" region, and a more important one in the "low mass - high z" region. The first is obviously due to J/ψ produced upstream the target and the second comes from J/ψ produced downstream. The global cut on the target variable helps in reducing this contribution as can be seen in plot (b).

3.4 Kinematical cuts

In order to have a better definition of the experimental acceptance some cuts have been imposed on some reconstructed kinematical variables. Essentially a cut in the reconstructed rapidity of the dimuon in the center of mass frame is applied:

$$-0.4 < y^* < 0.6$$

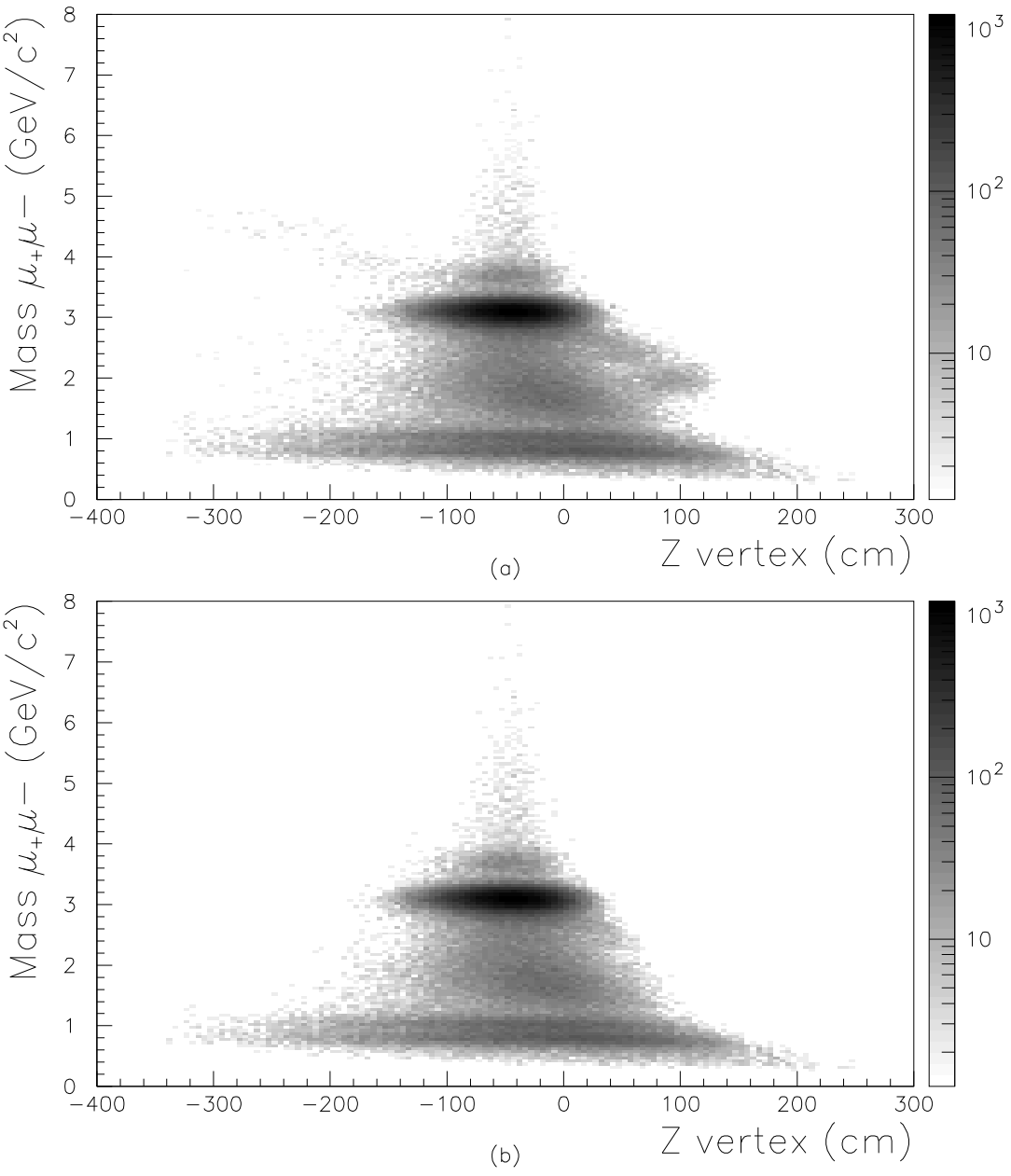

Figure 3.3: Effect of the global cuts on the rejection of out-of-target contributions. Reconstructed invariant mass is plotted versus the z vertex coordinate for opposite sign dimuons after kinematic cuts: a) without global cuts, b) after a 1% global cut on the target estimator.

and a cut on the decay angle of the dimuons in the Collins-Soper reference frame

$$-0.5 < cos\vartheta_{CS} < 0.5$$

These two cuts and their effect will be described in detail in Section 4.2 on page 76.

3.5 Reconstructed physical observables

3.5.1 The invariant mass spectrum of opposite sign dimuons

In Figure 3.4 I present the invariant mass spectrum for opposite sign dimuons in the kinematic region $-0.4 < y^* < 0.6$, $|\cos\vartheta_{CS}| < 0.5$, after applying a 1% cut on $PROB(P * DTarg)$.

Usually three regions are defined in such a spectrum:

- the low mass region (LMR) where the peaks of the $\omega + \rho$ and ϕ resonances clearly appear,
- the intermediate mass region (IMR), between the low mass resonances and the J/ψ peak,
- the high mass region (HMR), from the J/ψ upwards.

The J/ψ resonance is very pronounced thanks to the good mass resolution of the apparatus in this region of the spectrum. The low mass resonances are less pronounced either because of the poorer mass resolution, either because of the acceptance of the spectrometer. In fact the spectrometer setup is tuned in order to have maximum acceptance in the high mass region and consequently the acceptance vanishes in the low mass region.

The intermediate mass region is formed by the superposition of different sources, essentially Drell-Yan (DY) dimuons, semileptonic decay of charmed hadron pairs ($D\overline{D}$) plus a contribution due to dimuons from the decay of two pions or kaons.

In the high mass region the ψ' resonance is visible, even if the statistics is much lower then for the J/ψ .

At higher masses, as can be clearly seen in logarithmic scale (Figure 3.5), we have muon pairs coming from the Drell-Yan mechanism. As will be discussed later, these events are crucial as a reference for the study of J/ψ production.

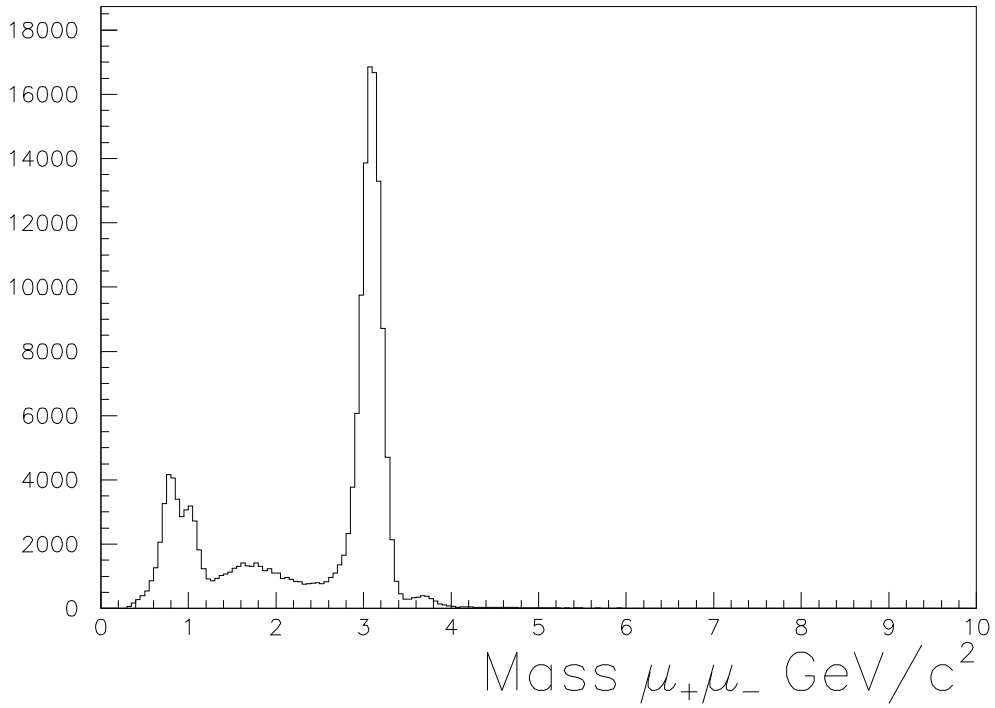

Figure 3.4: The invariant mass spectrum for opposite sign dimuons in the kinematic region that defines NA50 acceptance after 1% target cut.

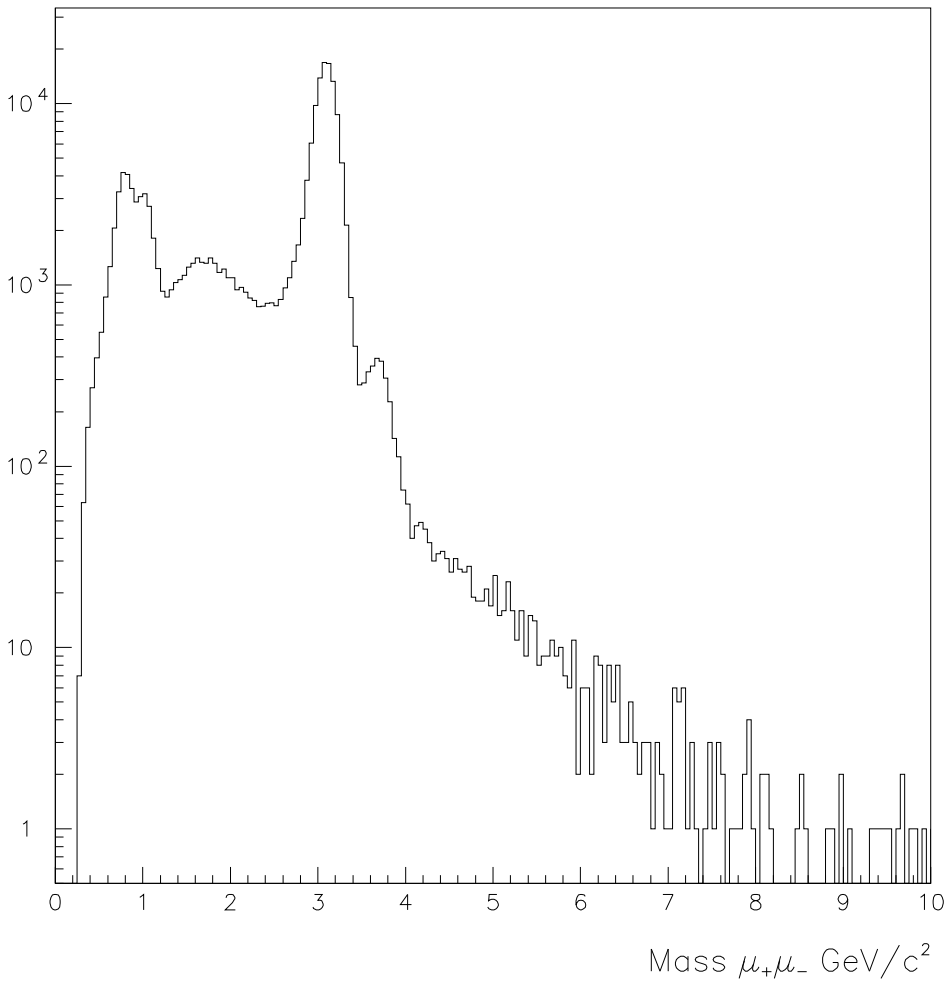

Figure 3.5: The invariant mass spectrum for opposite sign dimuons in the kinematic region that defines NA50 acceptance after 1% target cut.

3.5.2 Rapidity, transverse momentum, decay angle and momentum

In Figure 3.6 the raw spectra for other kinematical variables are presented. Together with the already discussed invariant mass plot, we show the rapidity distribution in the center of mass frame, the transverse momentum spectrum and the distribution of the cosine of the emission angle of one of the two muons in the Collins-Soper[3] reference frame.

The same plots are then presented in Figure 3.7 after kinematic cuts and after applying a 1% global cut.

From these two sets of plots we can clearly understand NA50 acceptance function. For a 450 GeV/c incident beam, the experiment selects dimuon produced around mid-rapidity in the center of mass frame. The muons coming from the decay of the resonance have a $cos(\vartheta_{CS})$ distribution peaked at zero. This corresponds to muons that are produced orthogonally to the beam axis in the center of mass reference frame. The Lorentz boost gives in the laboratory two muons with approximately the same energy. High values of $|cos(\vartheta_{CS})|$ are not accepted because in this case one of the two muons has very low momentum and it is stopped in the hadron absorber.

In Figure 3.8 the single muon momentum distribution is shown. A 10 GeV/c momentum cut due to stopping in the absorber and to loss of soft tracks too strongly deflected in the magnet is evident.

In Figure 3.9 the correlation between the mass of the dimuon and the transverse momentum of the dimuon is presented. This help to understand the mass cut that can be seen at low mass values in Figure 3.4, 3.6 and 3.7.

3.6 Run per run analysis

Data are collected in time slots called runs that are identified by an unambiguous "run number". This is done for practical reasons and to have tolerance versus faults in the data acquisition chain. This division is used to identify periods when the apparatus didn't work properly. Data corresponding to such runs are rejected.

[3]The Collins-Soper reference frame is defined in the center of mass frame (CM) of the muon pair.

Be $\overrightarrow{P_1}$ the momentum of the beam in the CM frame and $\overrightarrow{P_2}$ the momentum of the target, the z axis is oriented along the bisector of the angle between $\overrightarrow{P_1}$ and $-\overrightarrow{P_2}$. The y axis is taken parallel to $\overrightarrow{P_1} \times \overrightarrow{P_2}$ and the x axis is taken to form a right handed reference frame. The polar and azimuthal angles of the positive muon in this reference frame are named ϑ_{CS} and φ_{CS} respectively.

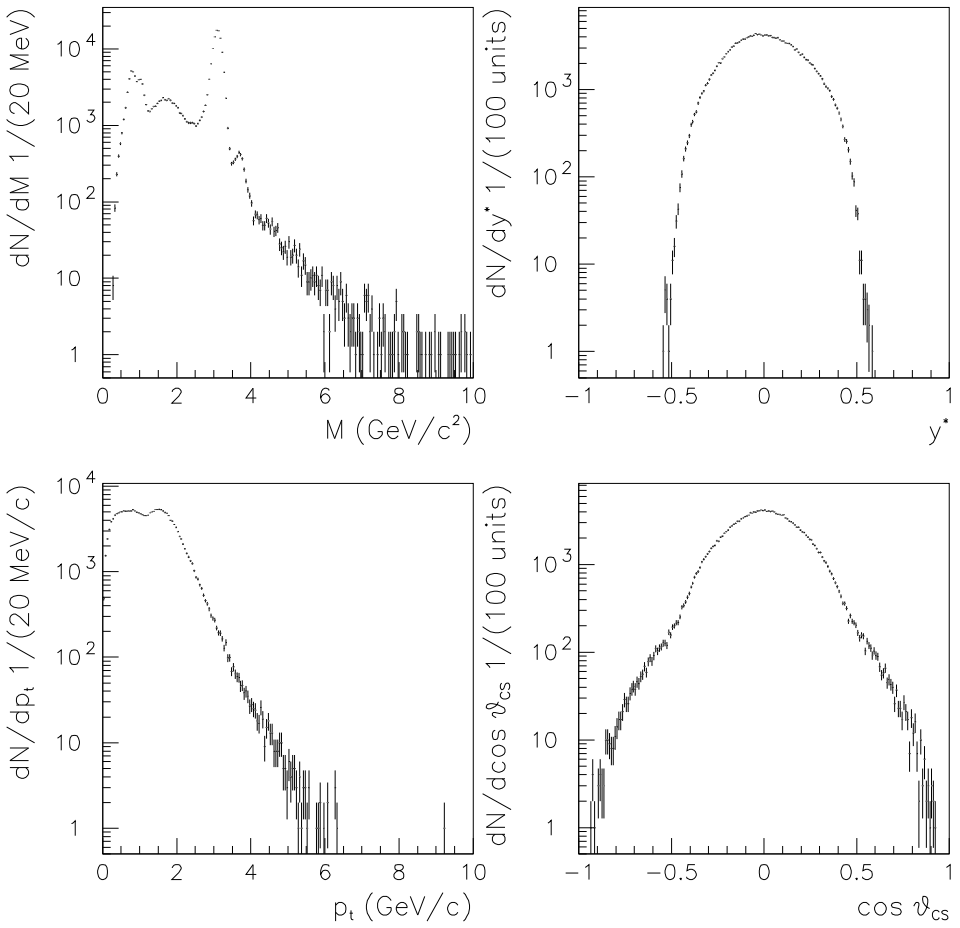

Figure 3.6: Mass, rapidity, p_t and $cos\vartheta_{CS}$ distributions of reconstructed events for p Al 1999.

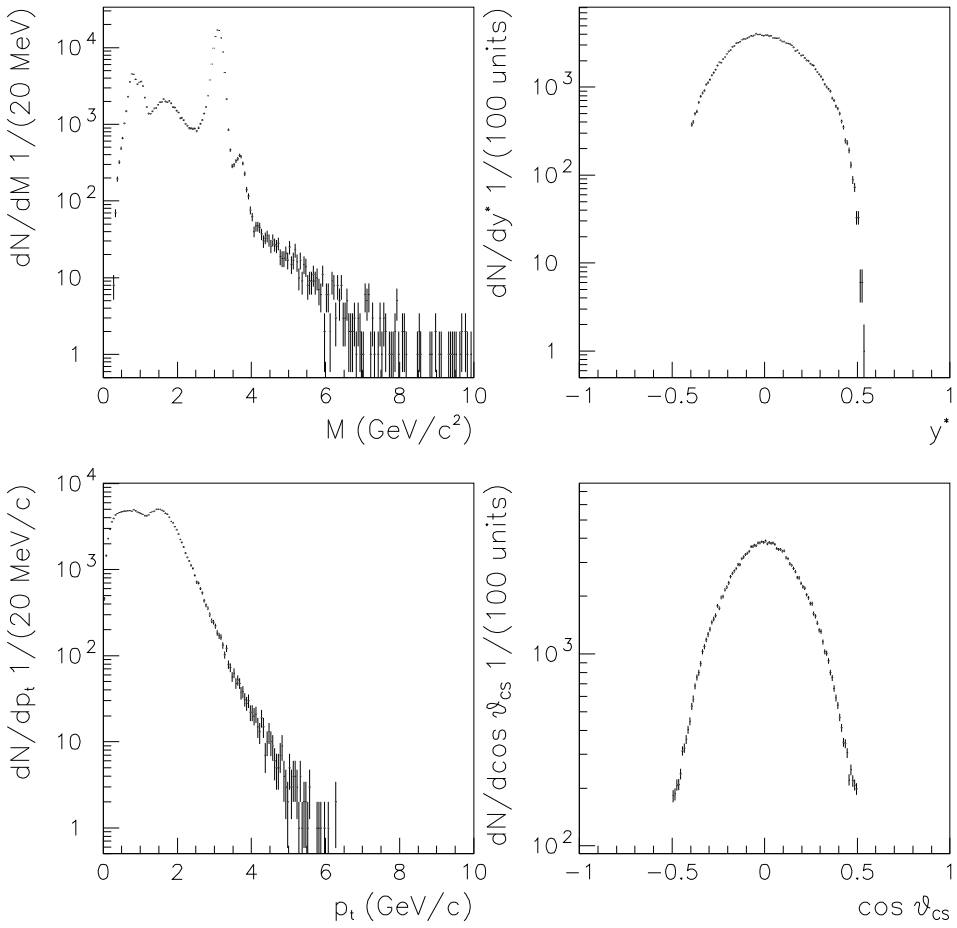

Figure 3.7: Mass, rapidity, p_t and $cos\vartheta_{CS}$ distributions of accepted events in the nominal acceptance with a standard cut of 1% on the $PROB(P * DTarg)$ distribution for p Al 1999.

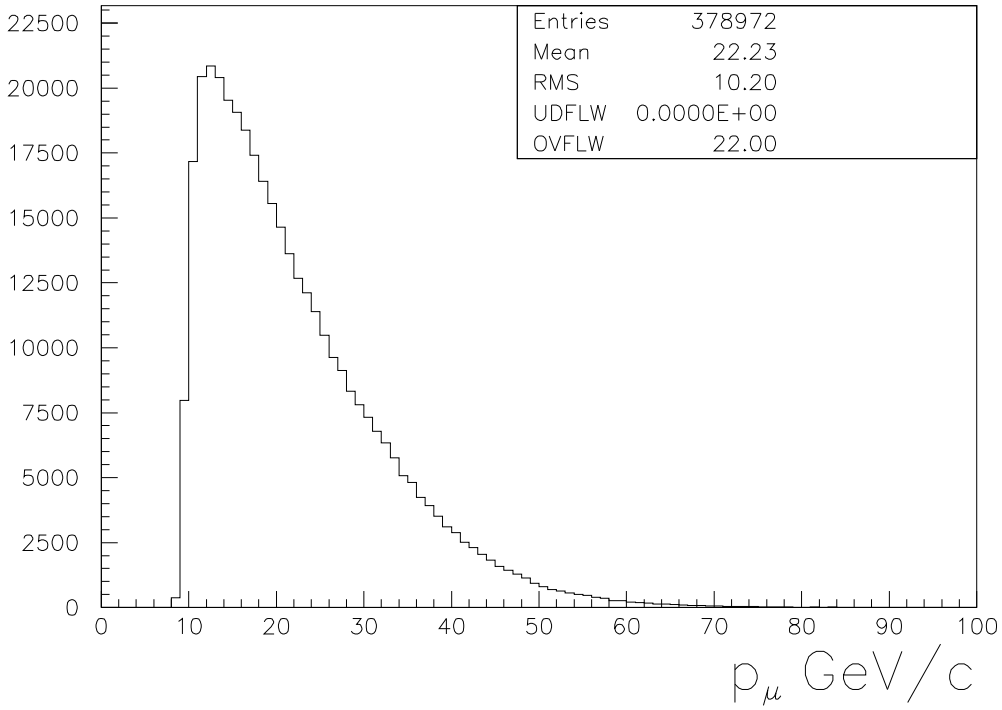

Figure 3.8: Momentum distribution for all reconstructed tracks after kinematic cuts and 1% global cut for p Al collisions at $450\,GeV/c$ of 1999 data taking.

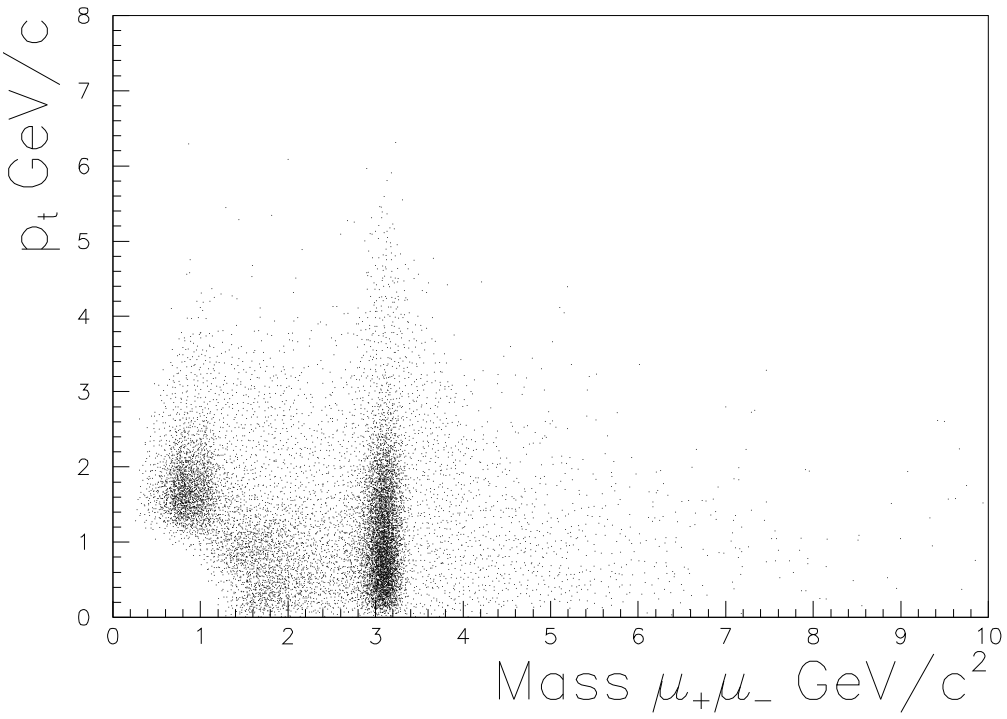

Figure 3.9: Correlation between transverse momentum and invariant mass for reconstructed tracks in p Al collisions after cuts.

Therefore, after reconstruction, an analysis is performed on a run by run basis. In the following figures some parameters of the data taking are plotted as a function of run number.

In Figure 3.10 I plot the beam intensity for the various data taking periods. The beam intensity is usually expressed in terms of counts on the first argon counter (named $ARGO1$) per burst (called argonium per burst). This unit is proportional to the number of protons and from the calibration runs we know that the scaling factor is approximately 6408 protons per argonium (with an uncertainty of 4%[4]). The burst length was 2.37 s for all the periods.

In Figure 3.11 I plot the trigger rate. This is very low, compared with the capability of the acquisition chain ($\approx$ 4000 triggers per burst). Therefore the live time of the apparatus is $\approx 100\%$.

In Figure 3.12 I plot the number of dimuons after some reconstruction steps (see caption).

In Figure 3.13 I plot the reconstruction efficiency. It depends on the beam intensity because is determined by the chamber occupation. The data studied in this thesis were collected using low intensity beams expressly to reduce the systematic errors connected with the estimation of the reconstruction efficiency.

3.7 Run selection

Since the cross section calculation crucially depends on a correct determination of apparatus inefficiencies and beam luminosities, it is very important to reject runs showing instabilities related to these quantities. This has been done in various steps.

First the annotations on the run log-book were used to reject runs with faults in the trigger chain or in the readout modules as well as runs with strong instabilities of the beam.

A further check of the performance of the apparatus has been done studying each sextant separately. The fraction of reconstructed tracks crossing each sextant is checked. If the apparatus did work properly this ratios should be constant.

In Figure 3.14 the number of reconstructed tracks divided by the total number of tracks is plotted for the p Be 2000 data taking (this was the worst period on the view point of faults in the electronics). The average value for each sextant has been calculated and then the number of standard deviation is computed run per run. The result is shown in Figure 3.15. A cut on the number of standard

[4]See Section 5.7 for details.

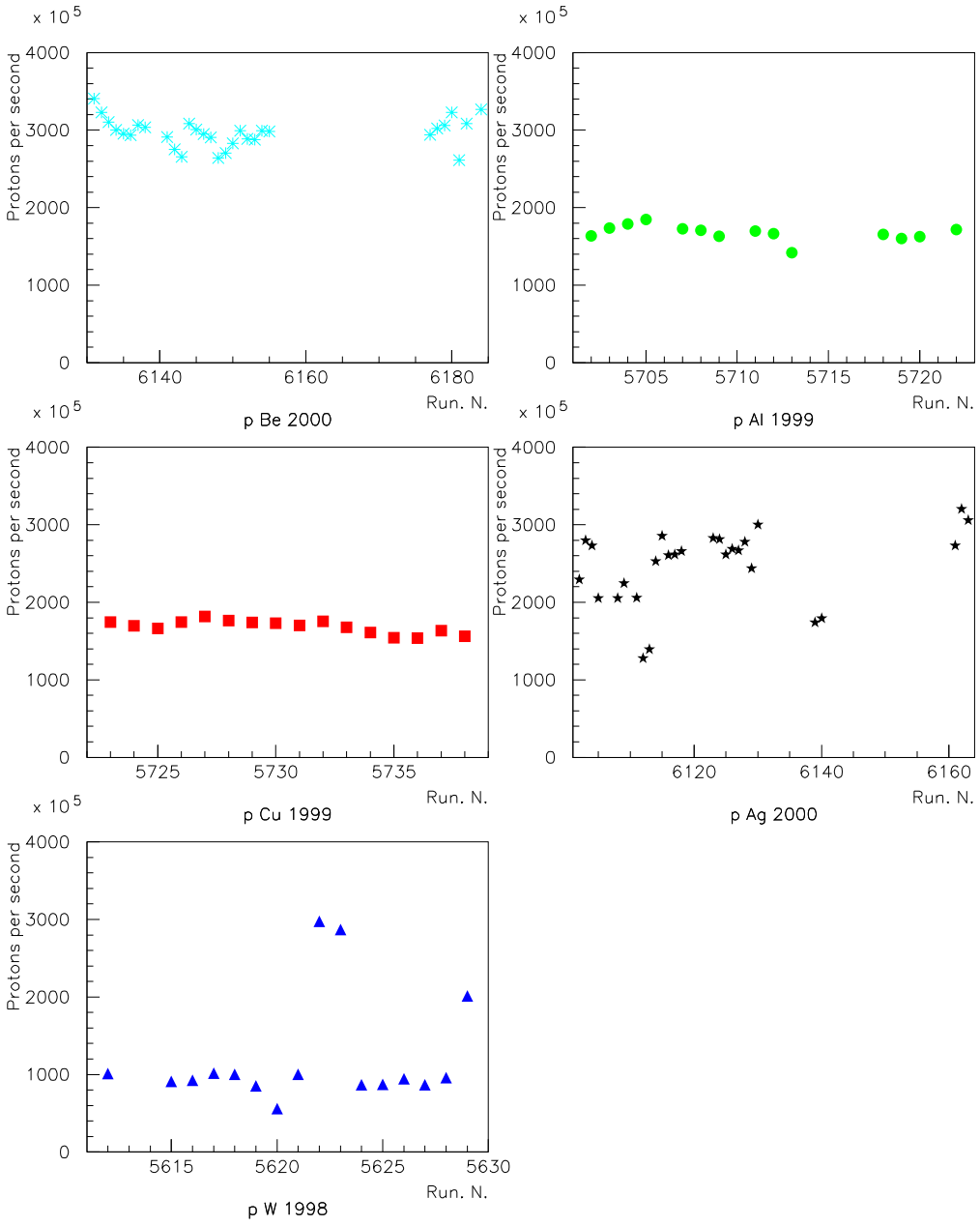

Figure 3.10: Beam intensity in the various periods of data taking.

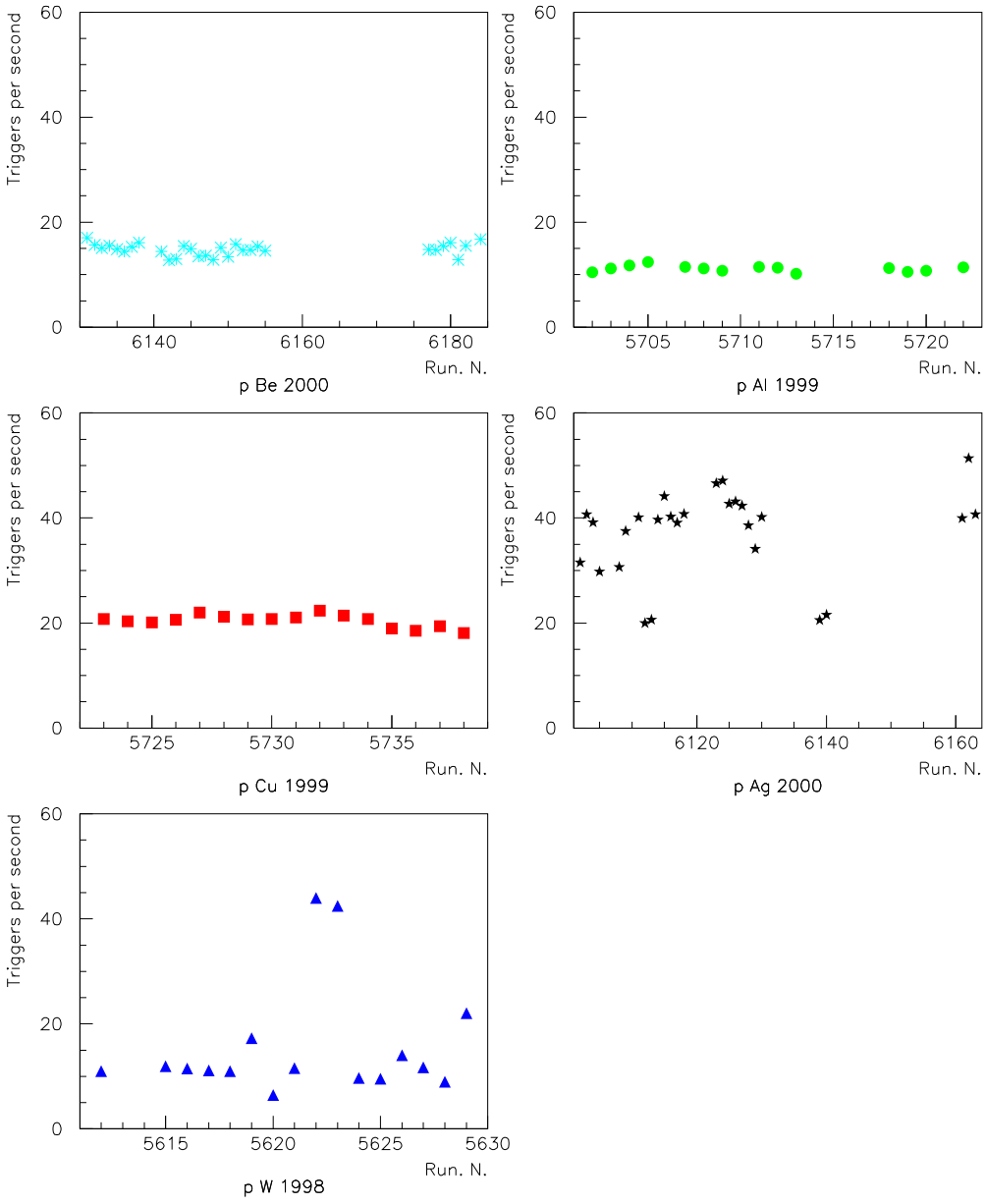

Figure 3.11: Trigger rate in the various periods of data taking.

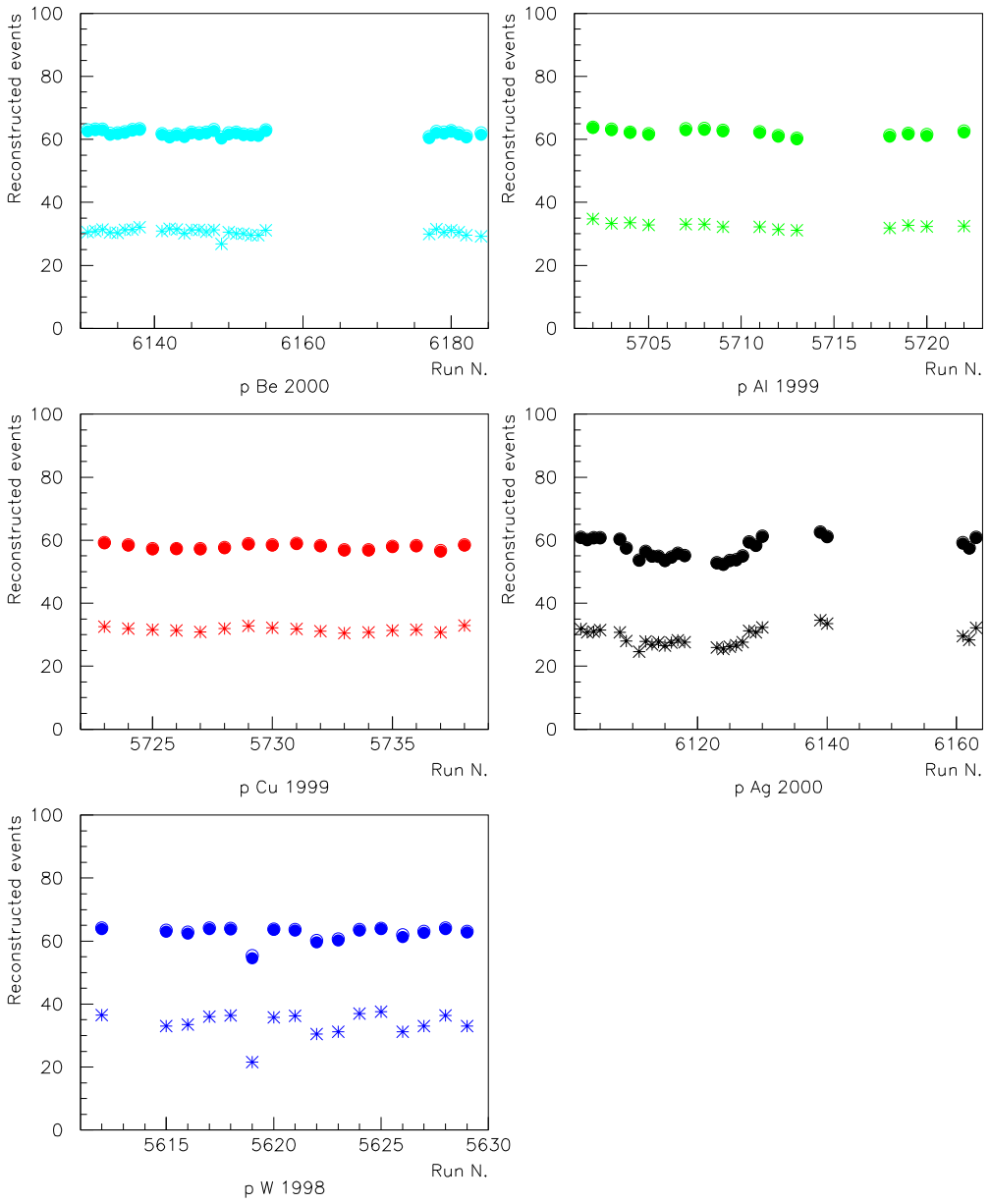

Figure 3.12: Dimuons after reconstruction steps. The (often hidden) open circles refer to the percentage of reconstructed event after tracking, the solid circles to that after vertex detection and the diamonds to that after geometrical cuts: fiducial, air-iron, and image cut.

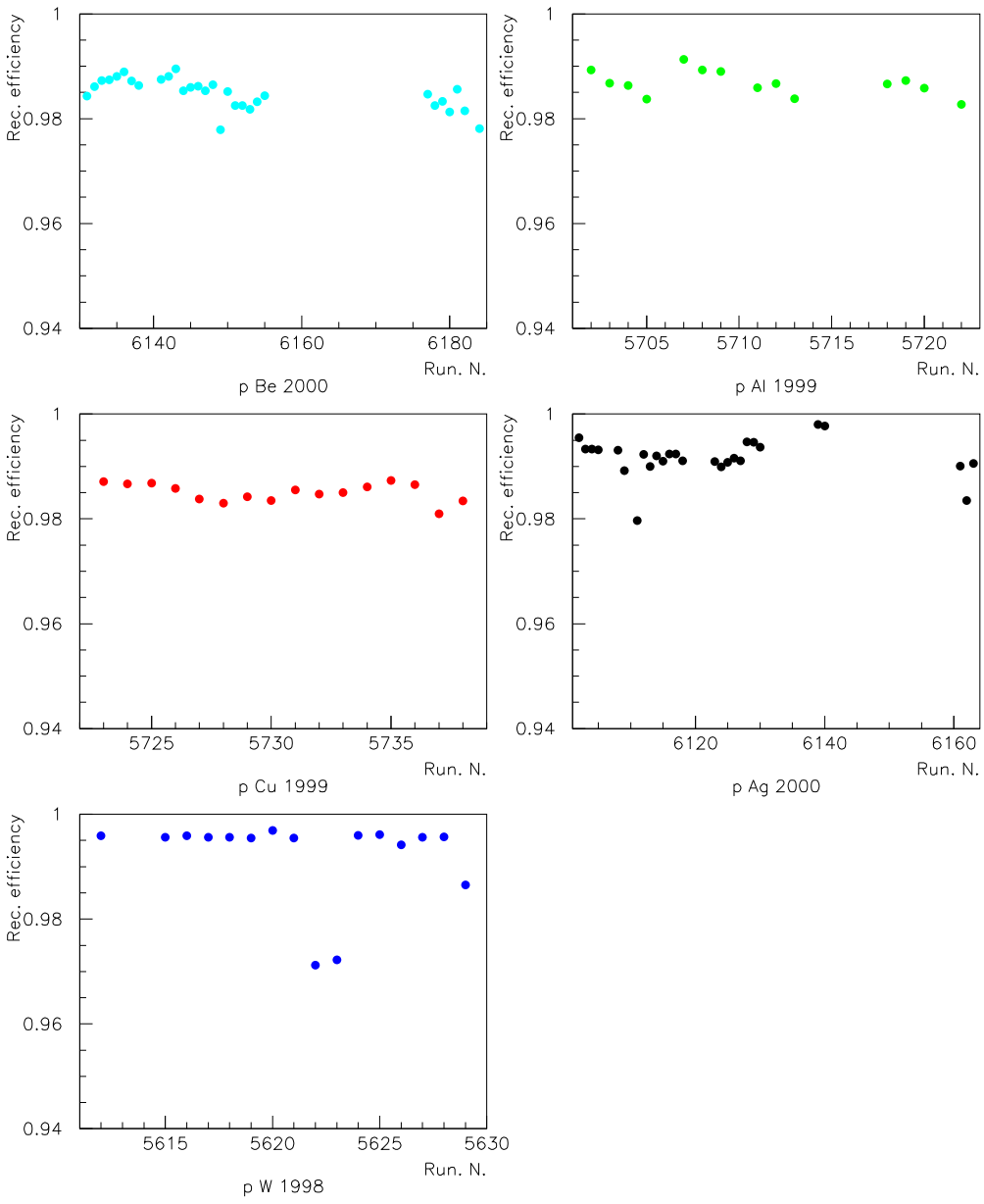

Figure 3.13: The reconstruction efficiency versus run number for the various data taking periods.

	RUN	discr. probl. coinc. probl.	sextant asymmetry	J/ψ mass	J/ψ width	other
p Be	6142, 6149, 6151	X				
	6145, 6150, 6155, 6178		X			
	6146	X		X		
	6180				X	
p Al	5704		X			
	5720		X	X		beam unst.
p Cu	5729, 5732, 5737			X		
p Ag	6102, 6105		X			
	6115			X		
	6118				X	
	6162, 6163		X			beam unst.
p W	5612		X			
	5615, 5616	X				
	5622, 5623, 5629					high int.

Table 3.2: Runs excluded from cross section calculation.

deviations is applied in two steps. First the most anomalous runs are rejected and then a new fit is performed and eventually a further rejection is done.

Another rejection criterion is given by the stability of the pole position and the width of the J/ψ . This allowed to reject some runs with instabilities in the magnetic field. In Figure 3.16 the pole position of the J/ψ is plotted versus run number and in Figure 3.17 the ψ width is shown.

In Table 3.2 the results of this run selection are summarised.

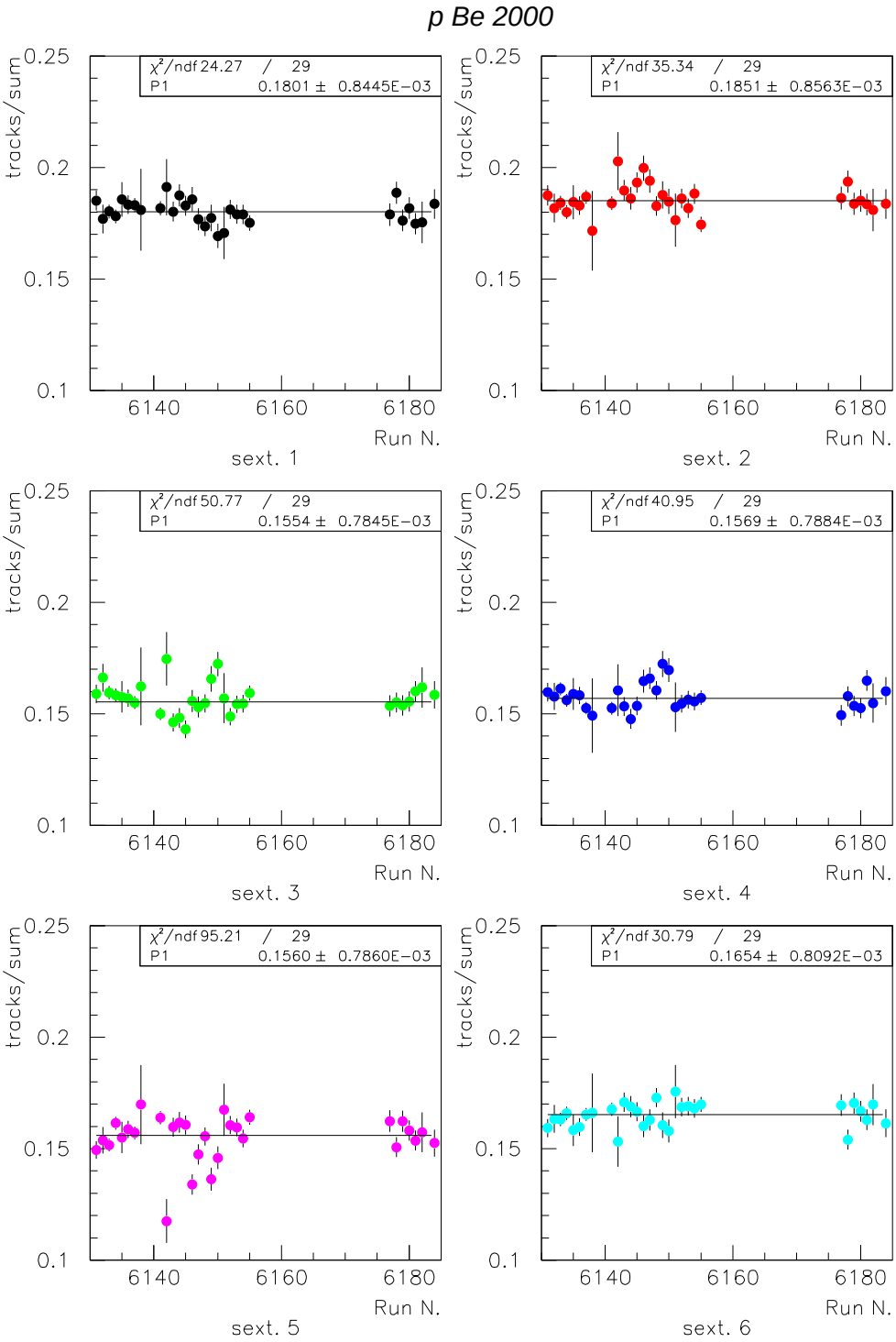

Figure 3.14: Sextants asymmetry during p Be 2000 data taking.

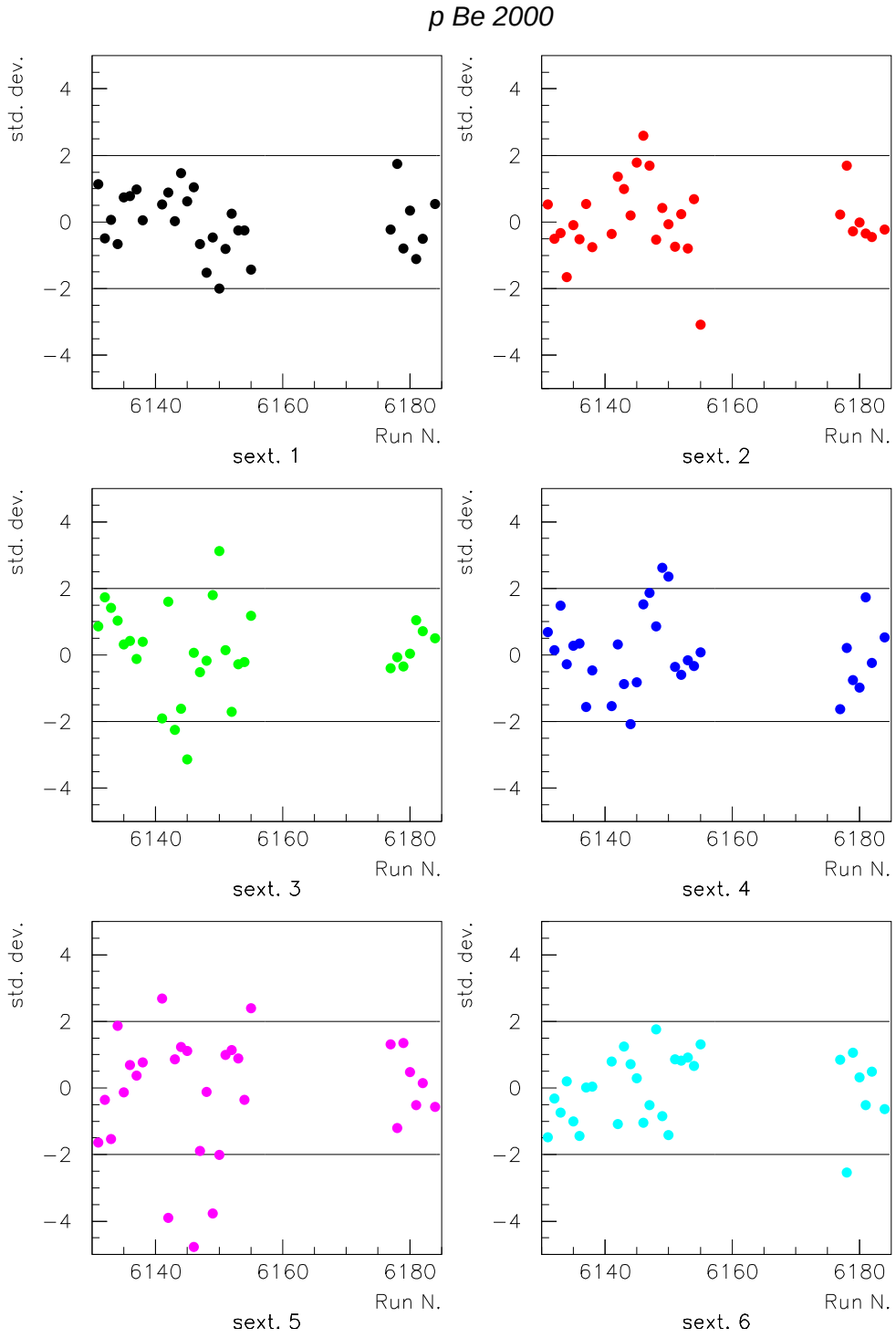

Figure 3.15: Sextant asymmetry in p Be 2000 data taking expressed in number of standard deviations with respect to the average behaviour.

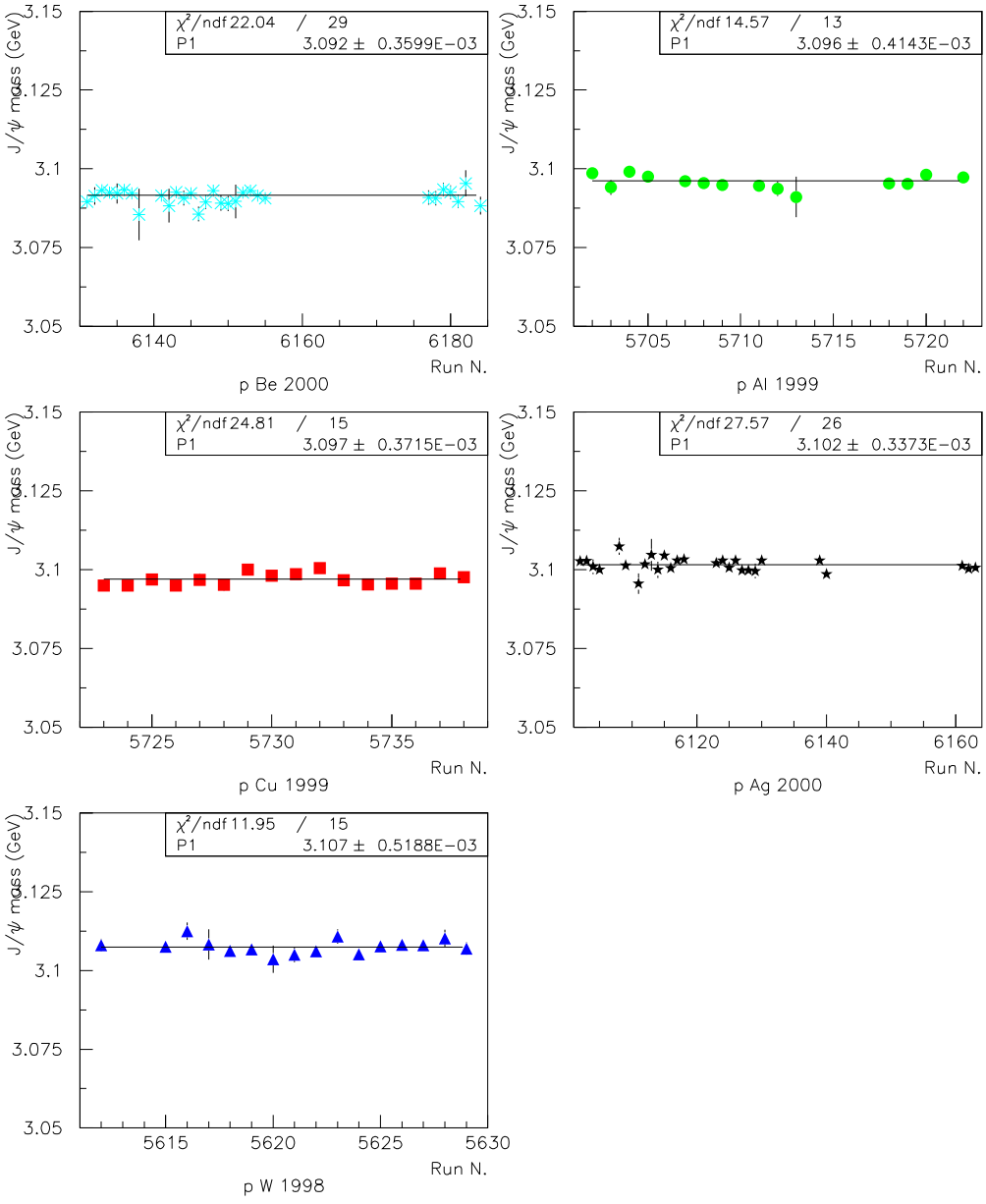

Figure 3.16: Fitted mass of the J/ψ in all proton nucleus runs.

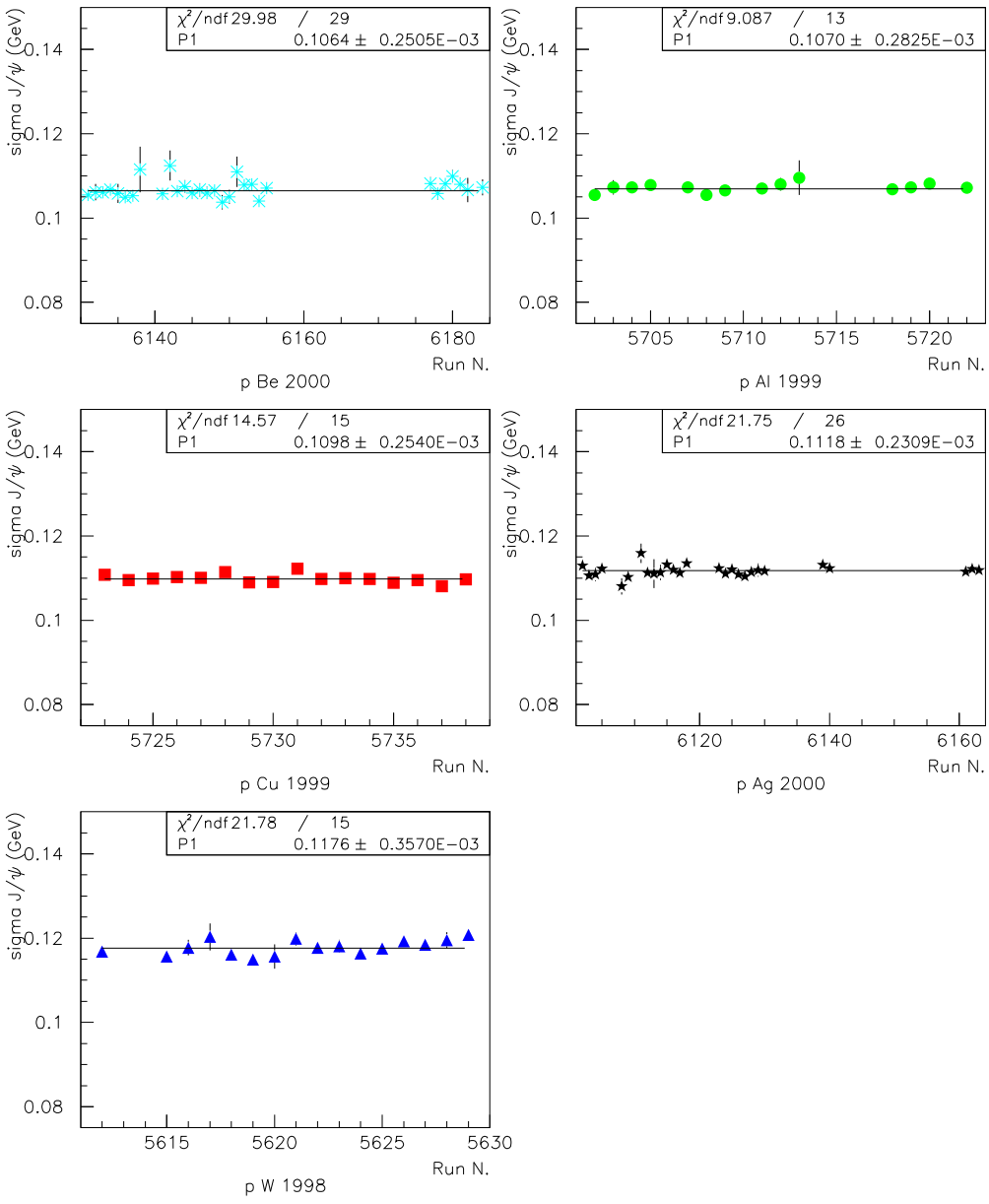

Figure 3.17: Fitted width of the J/ψ in all proton nucleus runs.

Chapter 4

The signal and background sources

4.1 Monte Carlo simulation of physical sources

The measured invariant mass spectrum in proton nucleus collisions is the sum of different components coming from different sources: the resonance decays, the DY continuum, the semi-leptonic decay of $c\bar{c}$ pairs and the combinatorial background of two muons coming from π and K decays.

In the data analysis we shall consider all the different sources and, with the aid of Monte Carlo techniques, obtain the expected shape of their invariant mass spectrum. The source shapes are used to fit the experimental data, obtaining the normalisations of the different contributions to the spectrum.

The Monte Carlo simulations also provide the estimation of the acceptances of every signal source, allowing to go back from the number of detected particles to the number of effectively produced particles in the phase space covered by the detector.

The determination of the mass shapes and the calculation of the acceptances, require the knowledge of the production mechanism as well as a detailed knowledge of the deforming action of the experimental apparatus.

The generation of the events is performed by a dedicated program (DIMUJET) that simulates the generation of the muon pairs and then tracks them through the experimental setup. After that it generates hits in the trigger scintillators and in the tracking chambers. At this point the reconstruction program (DIMUREC) is used to perform the reconstruction of the events. In this way the simulated events are treated in the same way real data are.

4.2 Principles

In order to completely define a particle, from a kinematic point of view, one needs to know its charge, mass and momentum. So in the study of a particle pair there are ten independent parameters. Since the NA50 experiment is studying neutral particles decaying into two muons, some of the ten parameters are constrained by charge and four-momentum conservation.

It turns out that four independent variables are needed to characterise the original particle. In the simulation the following quantities are used:

- the mass ($M_{2\mu}$),
- the rapidity in the center of mass of the collision ($y^*_{2\mu}$),
- the transverse momentum ($|P_{T\,2\mu}|$),

- the dimuon azimuthal angle.

The decay introduces two more degrees of freedom that can be chosen to be:

- the cosine of the polar angle ($cos\theta_{CS}$),
- the azimuthal angle (φ_{CS}) of one of the two muons in the Collins-Soper[1] reference frame.

The study of the present work is limited to the high mass region and intermediate mass region of the dimuon invariant mass spectrum ($M_{2\mu} > 2.0\,GeV/c^2$) and this excludes any contribution from ρ , ω and ϕ resonances.

It is convenient to study in the simulation only the region where the acceptance of the spectrometer is significantly different from zero:

$$-0.5 < cos\vartheta_{CS} < 0.5 \tag{4.1}$$

and

$$-0.4 < y^*_{2\mu} < 0.6 \tag{4.2}$$

The rapidity in the laboratory can be obtained from the rapidity in the center of mass through the relation

$$y_{lab} = y^* + y_{cms} \tag{4.3}$$

where y_{cms} is the rapidity of the center of mass system.

In this way 4.2 corresponds in the laboratory to

$$3 < y_{2\mu\,lab} < 4 \tag{4.4}$$

These cuts define the nominal acceptance of the spectrometer. The simulated events are generated on a phase space region larger than the acceptance of the spectrometer in order to take properly into account the smearing effect of the apparatus. Then, for the calculation of the acceptance, the previous kinematic cuts 4.1 and 4.2 are applied to the generated and reconstructed events.

A quality cut of 1% in the $PROB(P * DTarg)$ distribution (see Section 3.3.3) is also applied.

Finally, the reconstructed events are fitted with ad-hoc functions. The shapes obtained in this way are the used to fit the experimental data.

[1] See Section 3.5.2

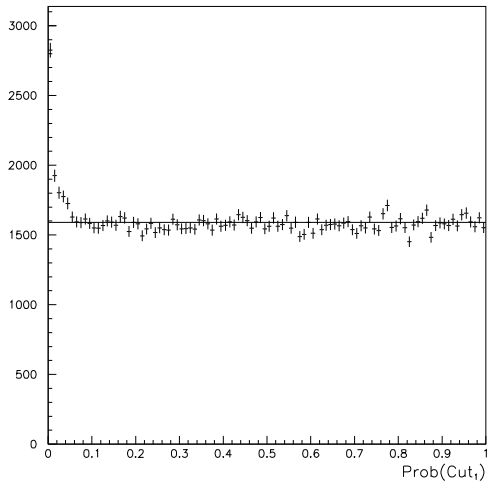

Figure 4.1: $Prob(P*DTarg)$ distribution for Monte-Carlo simulated J/ψ in p-Al collisions.

4.3 Global cuts

A problem with global cuts arises from the fact that the Monte Carlo simulation is not able to reproduce exactly the width of the $P*Dtarg$ distributions. This variable in fact is extremely sensitive to the multiple scattering in the absorber. It appears that the Monte Carlo simulation overestimates the widths of these distributions by about 10% . Using the global cut coefficients tuned on experimental data could therefore lead to an underestimation of the acceptances and to a biased calculation of the line shapes. Therefore the coefficients where then tuned separately for the Monte Carlo simulation and for the data.

4.4 The Drell Yan

As mentioned before, this process is the electromagnetic annihilation of a quark and anti-quark of the same flavour, with the creation of a virtual photon that decays into a lepton pair.

The DY distributions are calculated with the following parametrisations of the kinematical variables:

- *Mass and rapidity distribution*
  The program DIMUJET uses the leading order perturbative QCD cross section that is known to underestimate the real cross section by a factor K. This factor is of the order of 2 and is quite independent from the mass of

the virtual photon. So this distribution can be safely used to reproduce the shape of the distribution.

$$M^3 \frac{d^2\sigma}{dM\, dy^*} = \frac{8\pi\alpha^2}{9}\tau \sum_i e_i^2 \left[f_1^i\left(\sqrt{\tau}e^{y^*}\right) \overline{f}_2^i\left(\sqrt{\tau}e^{-y^*}\right) + \overline{f}_1^i\left(\sqrt{\tau}e^{y^*}\right) f_2^i\left(\sqrt{\tau}e^{-y^*}\right)\right] \tag{4.5}$$

where:
α is the fine structure constant,
M is the invariant mass of the dilepton pair,
$\tau = \sqrt{s}$ is the center of mass energy,
f_1^i and f_2^i are the proton parton distribution functions,
i is the quark flavour,
e_i is the corresponding quark electric charge,
y^* is the dilepton rapidity in the center of mass of the collision.

- *p_T differential distributions*
  It has been phenomenologically generated as a Bessel function of the transverse mass M_T :

  $$\frac{d\sigma}{dp_T} \propto p_T m_T K_1\left(\frac{m_T}{T}\right)$$

  K_1 is the first order modified Bessel function, i.e.

  $$K_1\left(\frac{m_T}{T}\right) = \frac{e^{-(m_T/T)}}{\sqrt{(m_t/T)}} \cdot P_6(T/m_T)$$

  where P_6 is a polynomial of order 6 and T=0.236 GeV/c^2

- *$\cos(\theta_{CS})$ and φ_{CS} distributions*
  The experimental angular distribution has been used:

  $$\frac{d\sigma}{d\cos(\theta_{CS})} \propto 1 + \lambda\cos^2(\vartheta_{CS}) \tag{4.6}$$

  where $\lambda = 1$ as measured by the NA10 experiment.
  A flat distribution in φ_{CS} has been used.

Different sets of parton distribution function have been used:

- From the MRS set, the functions n. 41 (MRS G, $Q^2_{min} = 5$, $\overline{MS}$) and 43 (MRS A $Q^2_{min} = 0.625$, $\overline{MS}$),
- the GRV 94 HO ($Q^2_{min} = 0.4$, $\overline{MS}$).

system	par_2 GeV/c^2	par_3 GeV/c^2	par_4 GeV/c^2	par_5 $(GeV/c^2)^{-1}$	par_6 $(GeV/c^2)^{-1}$
p Be	1.149± .005	0.642± .001	-1.313± .006	4.919± .045	-2.394± .018
p Al	1.154± .005	0.641± .001	-1.312± .006	4.889± .062	-2.401± .017
p Cu	1.148± .005	0.641± .001	-1.309± .006	4.872± .050	-2.418± .017
p Ag	1.148± .005	0.642± .001	-1.325± .006	4.950± .055	-2.386± .017
p W	1.167± .005	0.641± .001	-1.331± .006	4.982± .055	-2.333± .017

Table 4.1: Values of the parameters of the DY fitting function for the various nuclei obtained with the MRS A 43 structure function. A cut of 1% on the $PROB(P * DTarg)$ distribution is applied.

In Figure 4.2 the relevant kinematic variables for DY generation are plotted for p-Al collisions. In Figure 4.3 the invariant mass spectrum is detailed with the events at generation, at the input of the simulation (after kinematical cuts) and after reconstruction.

In Figure 4.4 the five invariant mass spectra are plotted and in Figure 4.5 they are compared with the p-Al spectrum.

In the figure 4.6 I compare the invariant mass spectrum obtained with the use of different structure functions. The differences are within 10% for a wide range of the spectrum.

For the standard analysis the MRS A 43 set has been employed.

4.4.1 Fit of the DY mass distribution

The DY Monte-Carlo mass distribution has been fitted with the following ad-hoc function:

$$\frac{dN}{dM} = par_1 \cdot \left(e^{-a_1} + par_5\, e^{-a_2} + par_6\, e^{-a_3}\right) \tag{4.7}$$

where

$$a_1 = M/par_2 \tag{4.8}$$
$$a_2 = M/par_3 \tag{4.9}$$
$$a_3 = (M/par_4)^2 \tag{4.10}$$

The values of the parameters obtained with the MRS A 43 structure function are listed in Table 4.1.

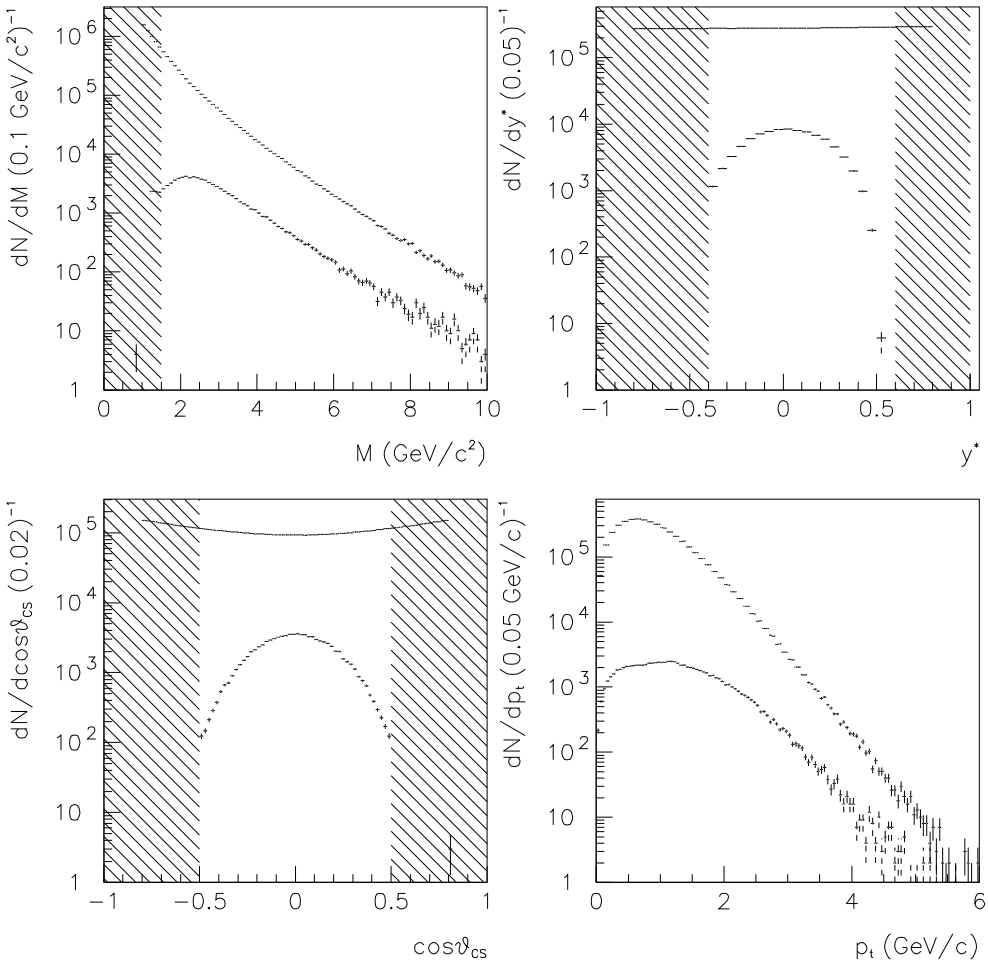

Figure 4.2: Simulation of DY process: spectra of generated (upper points) and reconstructed (lower points) events. The differential spectra in mass, center of mass rapidity, $cos\vartheta_{CS}$ and p_t are shown, integrated at each time on the other kinematic parameters. The shaded regions show the kinematic windows excluded from the analysis. This simulation uses structure function MRS 43 for the projectile and the target.

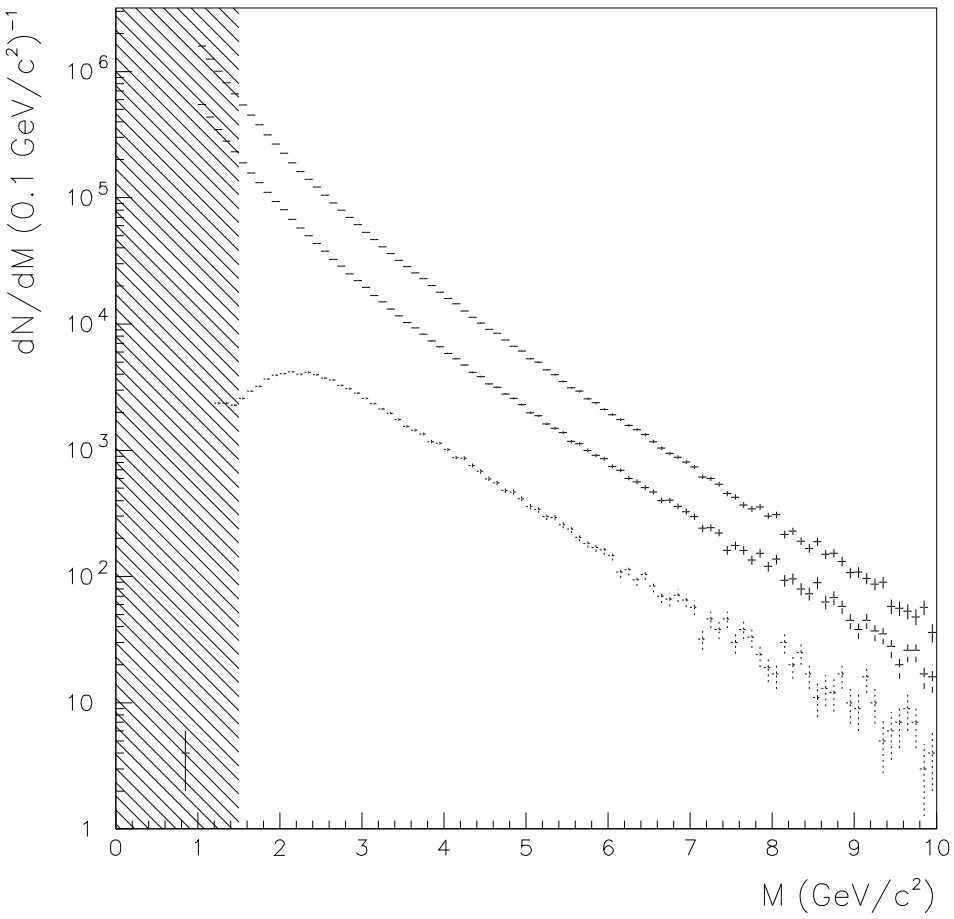

Figure 4.3: An enlarged view of the simulated DY mass spectrum, using the MRS 43 structure function for the projectile and for the target. The up-most points are the invariant mass distributions of the generated events before applying the kinematic cuts. The middle points are the invariant mass distribution for the generated events after applying the kinematic cuts. The lower points are for the reconstructed events. The shaded region is excluded from fits.

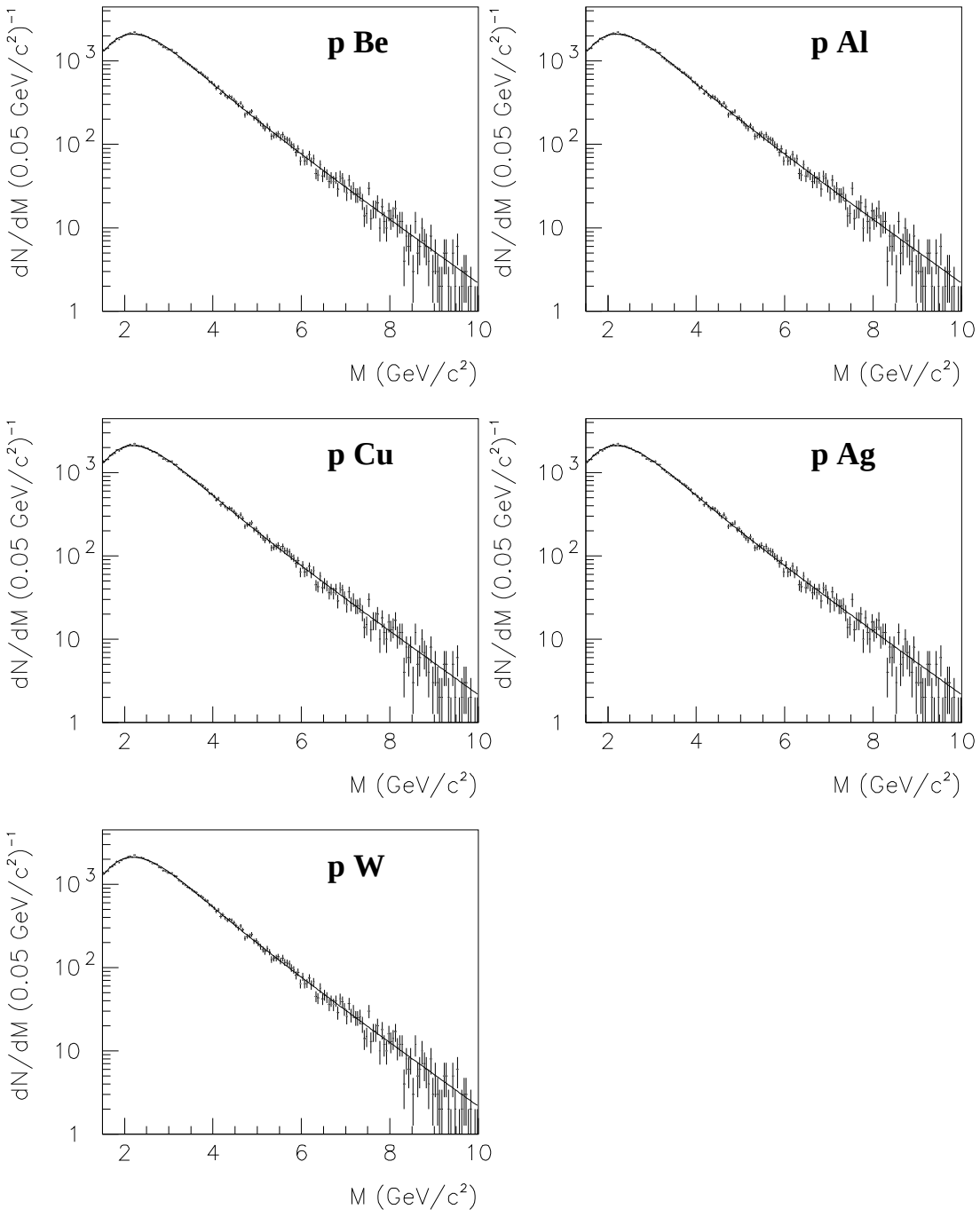

Figure 4.4: DY invariant mass spectra with structure function MRS 43 for the five nuclei.

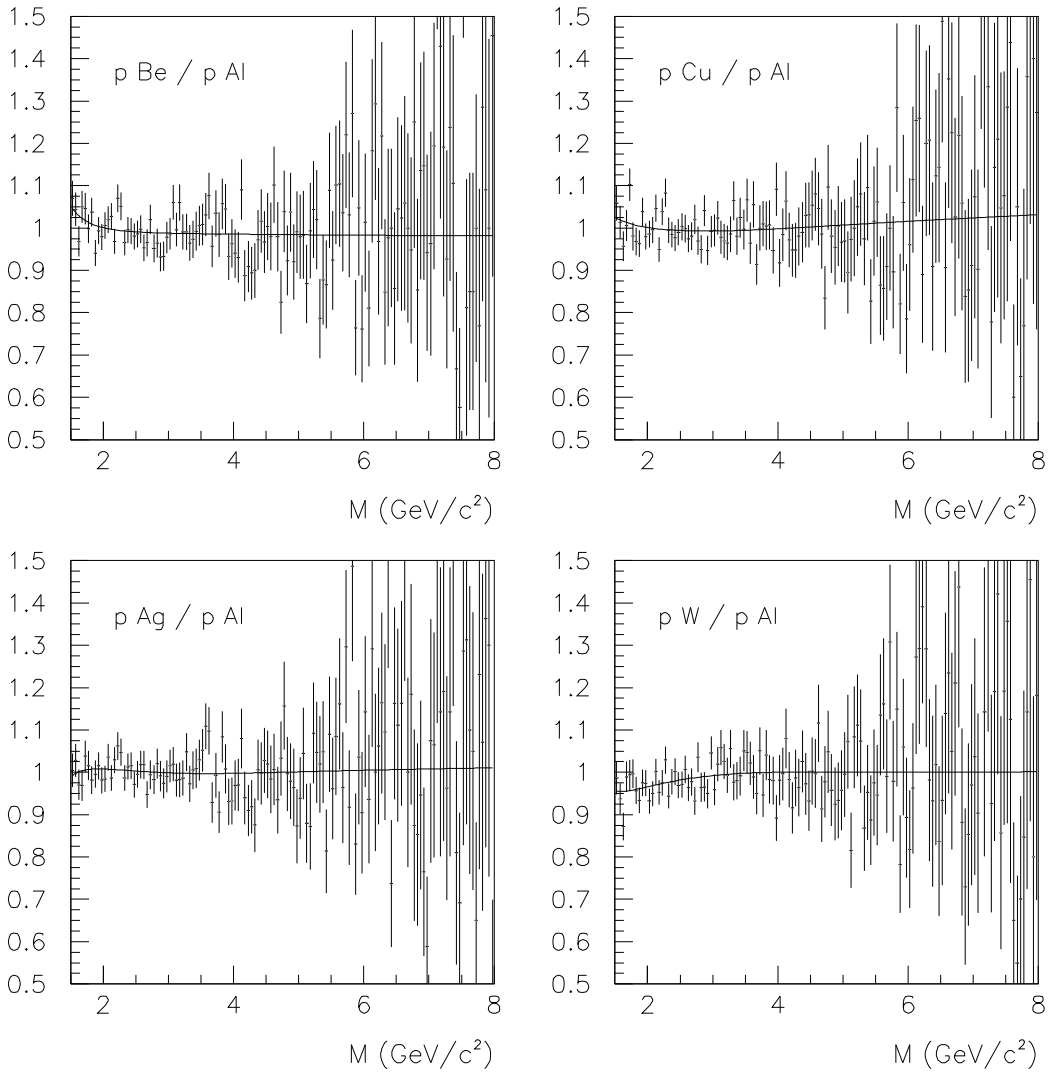

Figure 4.5: Comparison between the different shapes with the shape of proton aluminium collisions. The solid curve is the ratio of the fitted curves. The points with error bars are the ratios of the spectra bin by bin, starting from the same number of generated events.

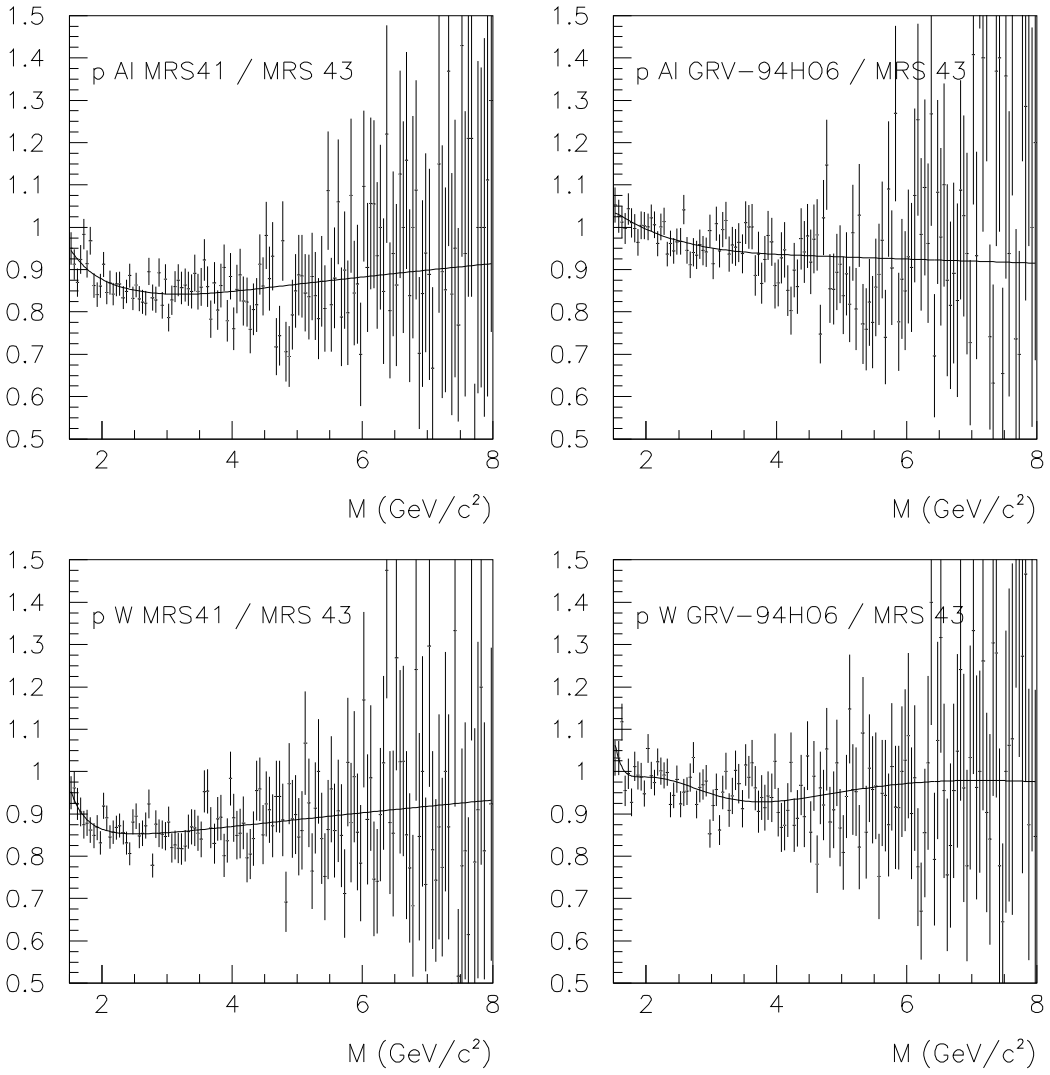

Figure 4.6: For the proton aluminium and proton Tungsten collision are shown the differences between the shapes obtained using structure functions: MRS 43, MRS 41, GRV 94 HO.

System	par_2	par_3	par_4	par_5
p Be, p Al	1.931± 0.009	0.37± 0.02	0.35± 0.04	1.5± 0.1
p Cu	1.977± 0.007	0.36± 0.03	0.34± 0.03	1.3± 0.2
p Ag	1.977± 0.008	0.36± 0.03	0.34± 0.03	1.3± 0.2
p W	1.916± 0.008	0.37± 0.03	0.36± 0.03	1.5± 0.3

Table 4.2: Values of the parameters of the Monte-Carlo open charm fitting function

The normalisation parameter par_1 is the only parameter that will be left free left free in the fits to the measured spectra in order to extract the size of the DY contribution.

4.5 The Monte-Carlo open charm generation

The Monte-Carlo open charm generation makes use of the PYTHIA event generator, since it has been previously verified that it reproduces well the differential distributions of D mesons produced in proton and pion induced reactions.

The reconstructed invariant mass differential distributions are fitted with an ad-hoc function:

$$\frac{dN}{dM} = par_1 \cdot e^{\{-\frac{1}{2}[(M-par_2)/\sigma]^2\}} \tag{4.11}$$

where

$$\sigma = \begin{cases} par_3 & \text{for M} < par_5 \\ par_3[1 + par_4(M - par_5)] & \text{for M} > par_5 \end{cases} \tag{4.12}$$

The values of the parameters are reported in Table 4.2.

4.6 The J/ψ and ψ' resonances

The J/ψ and ψ' Monte-Carlo mass distributions have been obtained using the following parametrisations:

- *Mass differential distributions*
  Fixed mass:

$$M_{J/\psi} = 3.097\,\mathrm{GeV}/c^2 \tag{4.13}$$

$$M_{\psi'} = 3.686\,\mathrm{GeV}/c^2 \tag{4.14}$$

- *Rapidity differential distributions*
  Gaussian with

  $$\mu_{y^*} = 0 \tag{4.15}$$

  and

  $$\sigma_{y^*} = 0.6 \tag{4.16}$$

- *Transverse momentum distribution*
  The same p_T distribution used for DY

- $\cos\vartheta_{CS}$ *distribution*
  Uniform distribution

In Figure and Figure the mass, rapidity, $\cos\vartheta_{CS}$ and p_T distributions are shown for the J/ψ and for the ψ' .

4.6.1 Fit of the charmonia line-shape

The reconstructed invariant mass spectrum of the J/ψ resonance has a very peculiar shape which poses some problem in the choice of the fitting function. We have adopted the procedure described hereafter.

The spectrum of the ψ is divided into three regions: left region ($M < y_1$) , central ($y_1 \leq M \leq y_2$) , and right region ($M > y_2$) . In the central region the ψ is considered Gaussian while in the other regions the tails are conveniently modified.

The J/ψ spectrum is described as follows:

$$\frac{dN_\psi}{dM} = par_1 * e^{-\frac{1}{2}\left(\frac{M-par_2}{\sigma}\right)^2} \tag{4.17}$$

Where

- par_1 is the normalisation factor,
- M is the mass expressed in GeV,
- par_2 is the mass of the resonance,

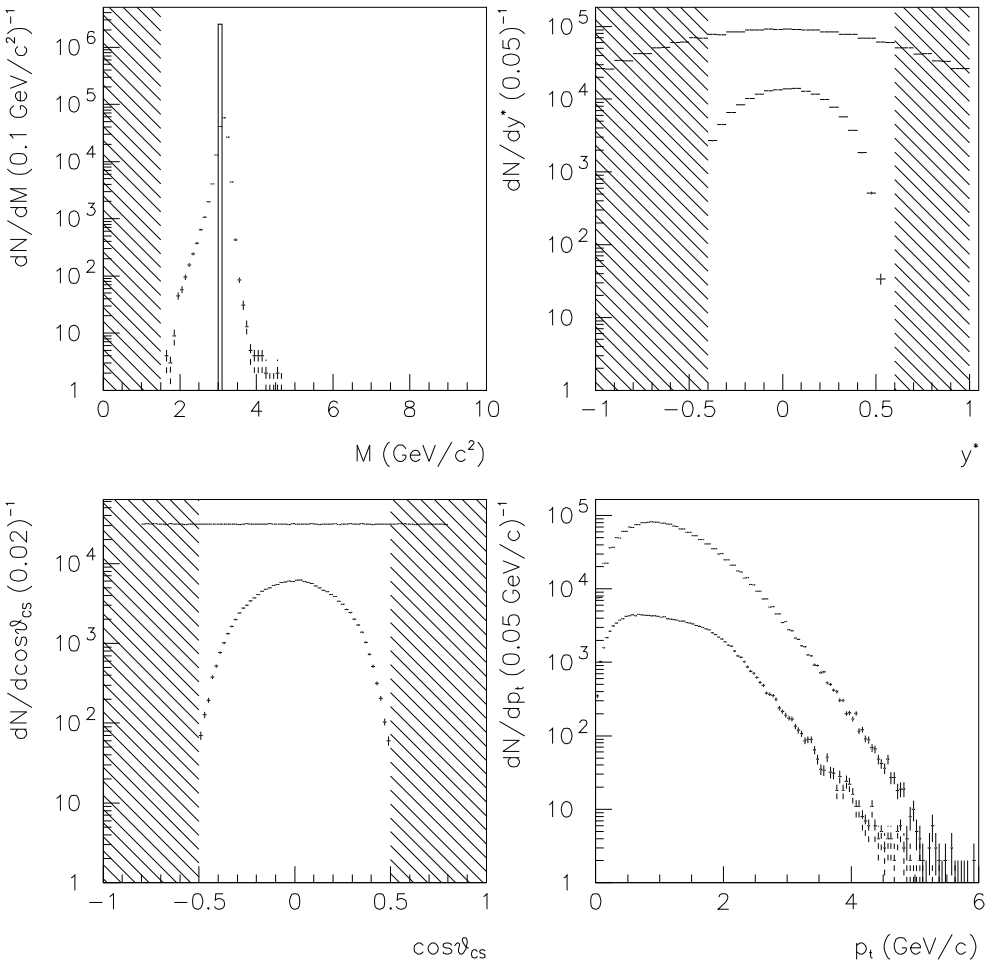

Figure 4.7: J/ψ Monte-Carlo simulation. Spectra of generated (upper points) and reconstructed (lower points) events. The differential spectra in mass, center of mass rapidity, $cos\vartheta_{CS}$ and p_t are shown, integrated at each time on the other kinematic parameters. The applied kinematic cuts are represented by shaded areas.

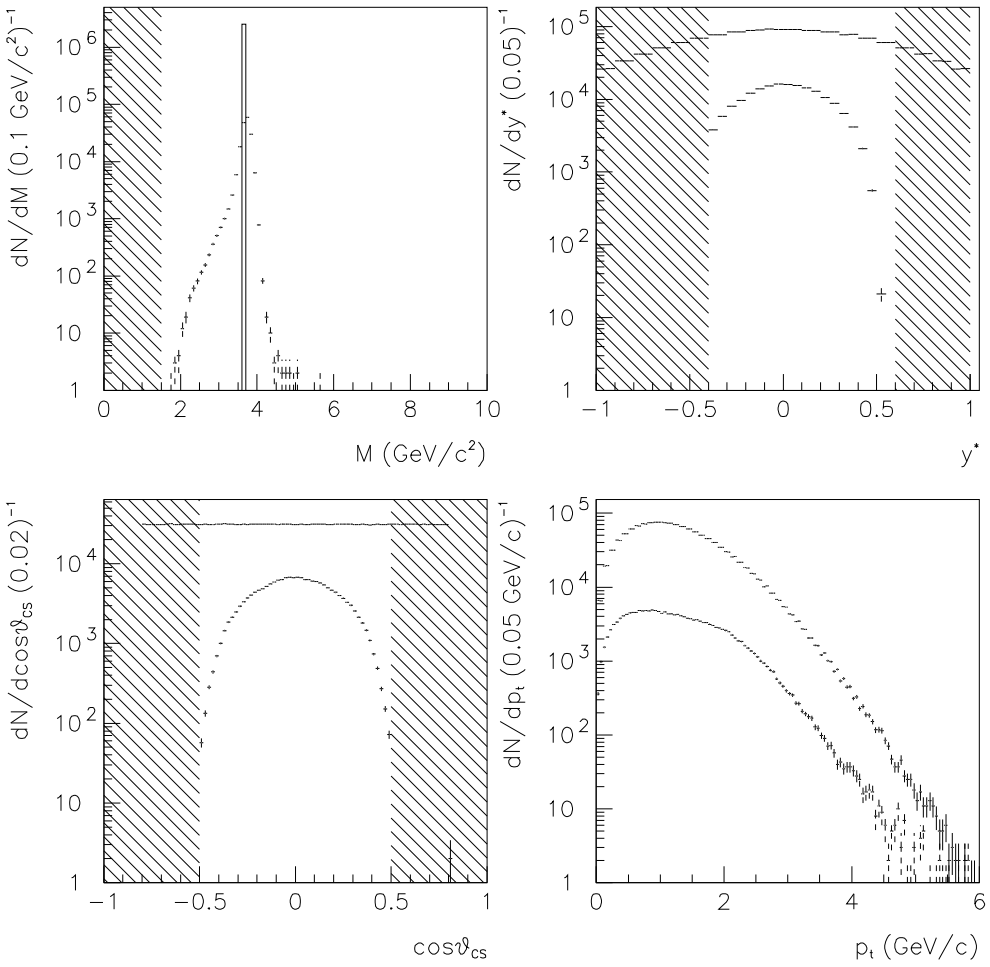

Figure 4.8: ψ' Monte-Carlo simulation. Spectra of generated (upper points) and reconstructed (lower points) events. The differential spectra in mass, center of mass rapidity, $cos\vartheta_{CS}$ and p_t are shown, integrated at each time on the other kinematic parameters. The applied kinematic cuts are represented by shaded areas.

- σ is the width of the Gaussian and has a value depending on M .
  In the central region σ has a fixed value that is estimated through a third free parameter: par_3
  outside this region it is parametrised as follows:

$$\sigma = par_3 * \left(1 + \left(par_4 * (y_1 - M)^{(par_5 - par_6 * \sqrt{y_1 - M})}\right)\right) \quad (4.18)$$

$$\sigma = par_3 * \left(1 + \left(par_7 * (M - y_2)^{(par_8 - par_9 * \sqrt{M - y_2})}\right)\right) \quad (4.19)$$

  for $M < y_1$ and $M > y_2$ respectively.

- y_1 and y_2 are defined as

$$y_1 = par_{10} * par_2$$
$$y_2 = par_{11} * par_2$$

The same technique is used to describe the J/ψ and the ψ' .

In Figure 4.9 the fits to the five Monte-Carlo spectra are plotted.

4.7 Acceptance

The acceptance is defined as the ratio between the number of reconstructed events in a particular phase space window and the number of generated events in that particular window.

For example, once a particular kinematic window in y^* , p_t , $\cos\vartheta_{cs}$ has been defined, the acceptance function in a certain invariant mass region is:

$$A = \frac{\int_{M_0}^{M_1} \frac{dN_{rec}}{dm} dm}{\int_{M_0}^{M_1} \frac{dN_{gen}}{dm} dm} \quad (4.20)$$

where:

- m is the mass of the dimuon pair,
- M_0 - M_1 is the mass window where the acceptance is calculated.

The events are generated in a kinematic window larger than the one where one wants to calculate the acceptance. In this way the smearing effect of the apparatus is taken into account properly: some events are in fact brought inside (or outside)

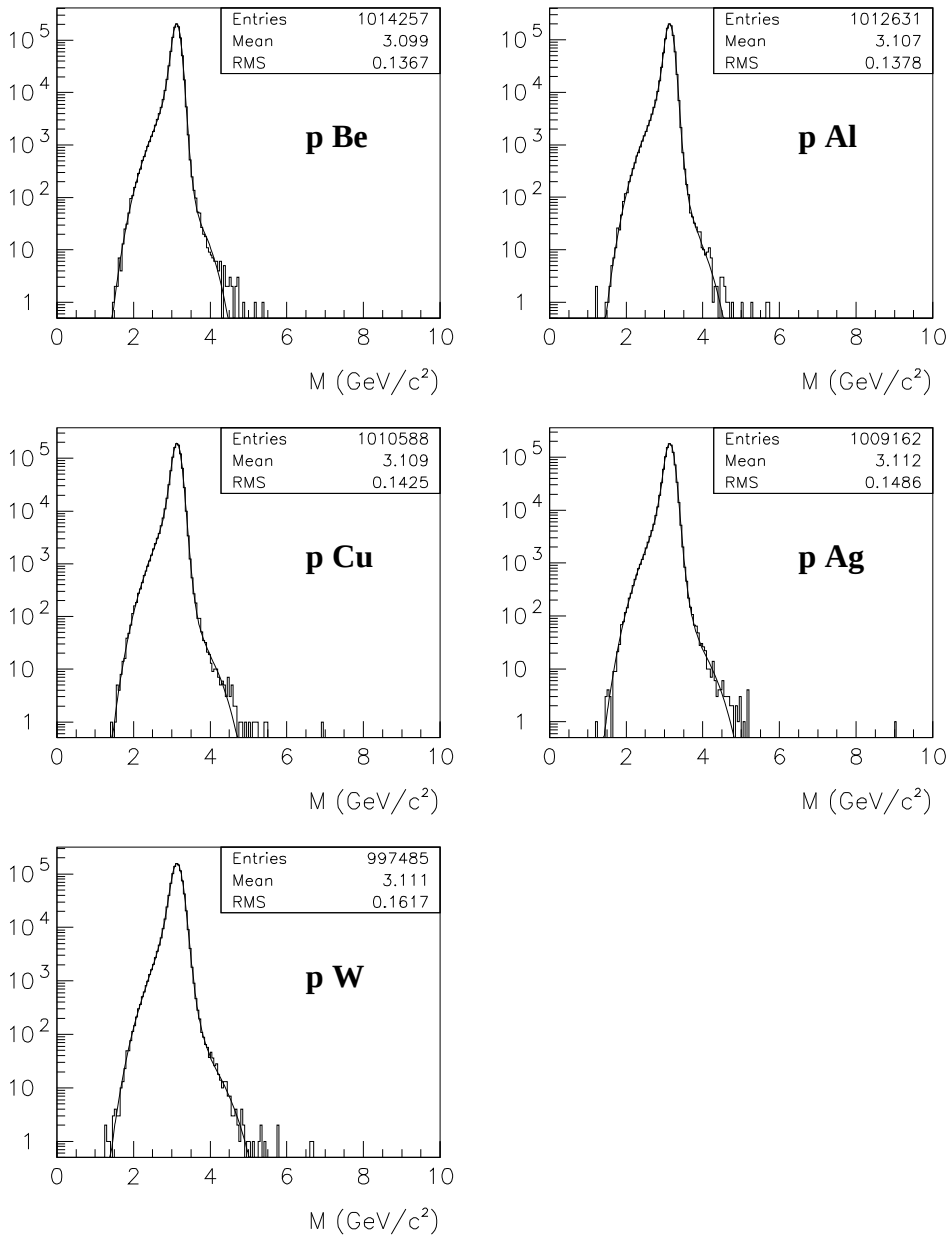

Figure 4.9: Fit to the reconstructed J/ψ mass distributions for the five p-A setups.

	p Be	p Al	p Cu	p Ag	p W
J/ψ	0.1408	0.1405	0.1401	0.1397	0.1386
ψ'	0.1664	0.1642	0.1637	0.1635	0.1628
DY	0.1379	0.1392	0.1393	0.1397	0.1389

Table 4.3: Calculated acceptances for J/ψ , ψ' and DY with 1% global cut on the target variable calculated with the refined procedure as explained in Section 3.3.4. The DY acceptances are calculated in the mass window $[2.9 : 4.5]\,\mathrm{GeV/c^2}$ using structure function MRS 43 and global cut coefficients tuned on the Monte Carlo simulations.

	p Be	p Al	p Cu	p Ag	p W
J/ψ	0.0910	0.0905	0.0901	0.0896	0.0895
ψ'	0.1057	0.1052	0.1048	0.1048	0.1049
DY	0.0882	0.0887	0.0889	0.0894	0.0893

Table 4.4: Calculated acceptances for J/ψ , ψ' and DY with 20% global cut on the target variable calculated with the refined procedure as explained in Section 3.3.4. The DY acceptances are calculated in the mass window $[2.9 : 4.5]\,\mathrm{GeV/c^2}$ using structure function MRS 43 and global cut coefficients tuned on the Monte Carlo simulations.

the acceptance region because of the finite resolution on the various physical variables.

When a cut on the quality of the tracks is performed at the reconstruction level for real data, this cut has of course to be taken it into account in the acceptance calculation.

In Table 4.3 and 4.4 the estimated acceptances for J/ψ , ψ' and Drell Yan are reported for MRS 43 structure function. A 1 % (Table 4.3) and 20 % (Table 4.4) global cut with coefficients tuned on the simulations themselves is included.

In order to ease the comparison of the results of this work with previous NA50 results, the number of Drell Yan pairs will be estimated in the mass window $[2.9 : 4.5]\,\mathrm{GeV/c^2}$. Therefore the acceptances for this process are calculated in this particular window.

4.7.1 Uncertainties on the acceptance calculation

The statistical error on the acceptances depends on the number of generated events and can be made arbitrarily small. Treatment of systematic errors is more delicate.

In this work I estimated the J/ψ cross section in the rapidity range $-0.4 < y^* <$

0.6 to ease the comparison with the NA51 results and with previous NA38 result. However the experimental setup was slightly changed in NA50. The acceptance at 450 GeV/c is now more centred around mid-rapidity. A more appropriate choice would be $-0.5 < y^* < 0.5$ as can be seen in Figure 3.6. I tried to estimate the systematic error connected with the different choices. I repeated the analysis in the second rapidity window for the p-Al data sample. I then rescaled the resulting cross section to the $-0.4 < y^* < 0.6$ range. A 0.5% difference is found compared to the direct cross section calculation.

This confirms that the errors on the acceptance calculations are negligible compared with the errors on the luminosity measurement that are discussed later in Section 5.7.

4.8 The combinatorial background

Several methods exist for the treatment of the combinatorial background in a dilepton experiment. The method used in this work is based on the distributions of the like-sign muon pairs.

This is due to the fact that the π and K decays,

$$\pi^+(or\, K^+) \rightarrow \mu^+\nu_\mu \tag{4.21}$$

and

$$\pi^-(or\, K^-) \rightarrow \mu^-\overline{\nu}_\mu \tag{4.22}$$

contribute both to the opposite sign and like sign spectrum.

From simple statistical arguments the spectrum of the opposite sign pairs can be derived from the like sign.

Be $< N^+ >$ the mean number of positive muons and $< N^- >$ the same quantity for μ^- generated in N interactions. The positive muons have a probability p^+ to satisfy the trigger condition, therefore

$$< N^+ >= p^+ < N^+ > \tag{4.23}$$

will give the single muon signal.

The probability of forming a $\mu^+\mu^+$ pair is

$$p^{++} = p^+ * p^+ \tag{4.24}$$

so, on average a number of $< N^{++} >$ triggers will be given on $\mu^+\mu^+$ pairs.

The p^+ can be written as

$$p^+ = \sqrt{\frac{< N^{++} >}{N}} \tag{4.25}$$

The number of opposite sign dimuon pairs can then be estimated as

$$< N^{+-} > = 2 * N * p^+ p^- \tag{4.26}$$

$$< N^{+-} > = 2 * N \sqrt{\frac{< N^{++} >}{N}} \sqrt{\frac{< N^{--} >}{N}} \tag{4.27}$$

$$< N^{+-} > = 2\sqrt{N^{++} N^{--}} \tag{4.28}$$

The above formula makes the assumption that the acceptance for $\mu^+\mu^+$,$\mu^-\mu^-$ and $\mu^+\mu^-$ is the same. If not the estimation provided by the 4.28 has to be corrected for the acceptances:

$$< N^{+-} >= 2\sqrt{N^{++} N^{--}} * \frac{A^{+-}}{\sqrt{A^{++} * A^{--}}} \tag{4.29}$$

In NA50 the acceptance for positive and negative muons is the same so the simple 4.28 formula is valid. This is achieved by the imposition of the image cut on data during reconstruction.

In order to correct for a possible inefficiency of this cut procedure, the sign of the magnetic field is regularly reversed. Half of the statistics is collected with one field and the other half with opposite polarity.

The equation 4.28 has to be modified:

$$< N^{+-} >= 2 \left\{ \sqrt{(N^{++} N^{--})_{(+)}} + \sqrt{(N^{++} N^{--})_{(-)}} \right\} \tag{4.30}$$

The above calculation is strictly valid only for events where no charge correlation is present. This is not the physical case because in each interaction the positive and negative charged mesons are constrained by total charge conservation law.

When the multiplicity of the produced particles is large (for example in central ion-ion collisions) or when there is the superposition of many interactions in the same trigger gate, the correlation is smeared out and the 4.30 holds.

Otherwise it is necessary to correct for these charge correlation effects and equation 4.30 has to be multiplied by and R_{bck} factor, that is expected larger than 1 in p-A collisions.

$$< N^{+-} >= 2R_{bck}\left\{\sqrt{(N^{++}N^{--})_{(+)}} + \sqrt{(N^{++}N^{--})_{(-)}}\right\} \tag{4.31}$$

In Figure 4.10 the four like-sign spectra are shown.

The calculated opposite sign background is then fitted with an ad-hoc function and used in the fit with the appropriate R_{bck} factor. In Figure 4.11 the background estimation for the p Al 1999 data sample is plotted.

4.9 The R_{bck} factor

The precise calculation of the R_{bck} factor has been performed according to the procedure described in Ref. [9] and [13], by means of a Monte-Carlo simulation shortly described hereafter.

Basically, using VENUS 4.12, a large number of p-A events has been generated and the π and K four-momenta have been stored.

For each meson the total decay probability is computed, taking into account the energy loss along the hadron path in the absorber and the interaction cross section with the absorber. Then, for each event the mesons are combined in all possible ways and each meson is forced to decay into a muon.

For each muon combination a dimuon is formed and the kinematical variables are computed. The NA50 acceptance cuts are applied to the dimuon, and, for the surviving dimuons, a weight equal to the product of the decay probabilities of the single mesons is assigned. The total number of N^{++} , N^{--} , N^{+-} pairs is computed taking into account the weights and the R_{bck} is finally extracted as:

$$R_{bck} = \frac{N^{+-}}{2\sqrt{N^{++}N^{--}}} \tag{4.32}$$

The possible interaction pile-up in the same trigger gate is taken into account in the simulation assuming a poissonian distribution of the arrival times of the protons on the target.

4.10 The empty target contribution

The empty target contribution has been measured in high intensity runs and has been fitted with an ad hoc function as shown in Figure 4.12. A smooth continuum is visible, two peaks at $M \sim 2.9$ and $M \sim 3.2\,\mathrm{GeV/c^2}$ laying on it. The two peaks are both formed by J/ψ events. The low mass peak is formed by J/ψ

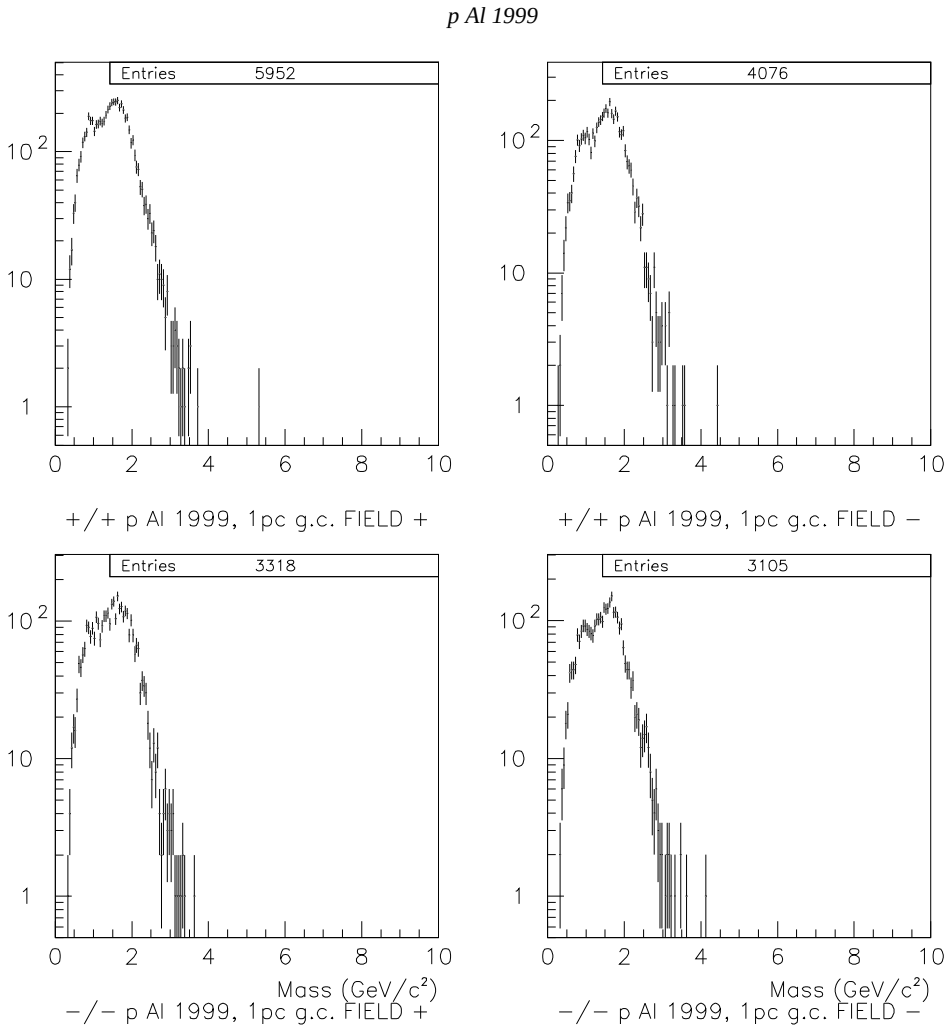

Figure 4.10: Like sign dimuon spectra for the p Al 1999 data set.

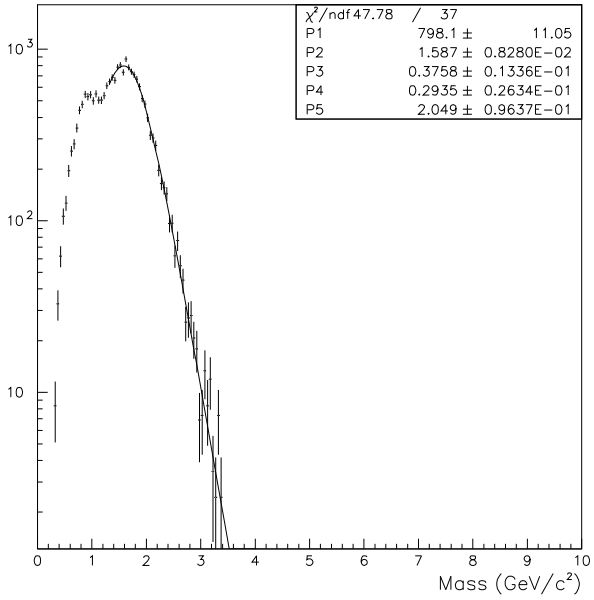

Figure 4.11: Opposite sign background calculated with the described method for the p Al 1999 data set.

that are produced downstream the target in the beryllium absorber that starts ≈ 30 cm after the target. The reconstruction program assumes that they come from the target in the invariant mass calculation. Therefore they are assigned a lower opening angle that results in a mass shift. The high mass peak vice versa is formed by J/ψ produced upstream the target (for example in proton-air interactions or in the argon counters).

The spectrum has been normalised to the number of argonion counts (see Section 2.3.2).

Because of the extremely low trigger rate, the combinatorial background contribution in the empty target runs is negligible.

4.11 The DY scaling

In order to compare data taken with incident protons of 450 GeV/c momentum with other experimental data one must know the scaling of DY cross sections with respect to $\sqrt{s}$ and to different phase space regions. An isospin dependence due to the fact that $\sigma_{pp}^{DY} \neq \sigma_{pn}^{DY} \neq \sigma_{nn}^{DY}$ must also be taken into account.

The calculation of the correction factors is done through an ad-hoc program (CROSS) that calculates DY cross section at Leading Order.

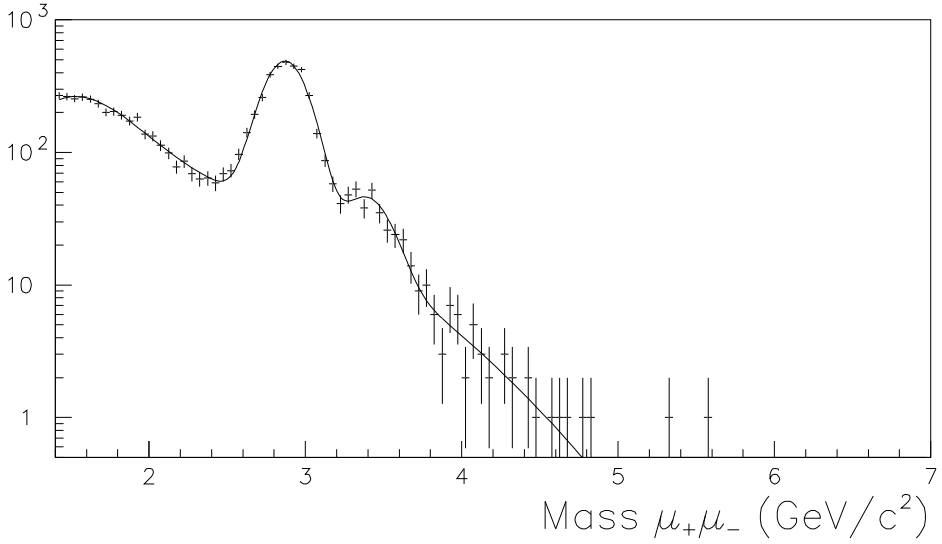

Figure 4.12: Empty target invariant mass spectrum for opposite sign muon pairs within the standard cinematic windows and after global cuts

Having measured, for example, σ_{DY} at 450 GeV/c, the scaling to 200 GeV/c is obtained as:

$$\sigma_{DY}(200\,GeV) = \sigma_{DY}(450\,GeV) \cdot \frac{\sigma_{DY}^{calc}(200\,GeV)}{\sigma_{DY}^{calc}(450\,GeV)} \tag{4.33}$$

The scaling factors are of course calculated for a particular phase space region. Since NA38 has taken data also at 200 GeV, in the rapidity domain $0 < y^* < 1$, the comparison with NA50 data, taken at 450 GeV in the rapidity domain $-0.4 < y^* < 0.6$, can be done using the conversion factor

$$A_{y,E} = \frac{\sigma_{pA}(200\,GeV,\, 0 < y^* < 1)}{\sigma_{pA}(450\,GeV,\, -0.4 < y^* < 0.6)} \tag{4.34}$$

To correct for isospin dependence in DY production we consider the nucleus as being made only by protons. Therefore the following correction is applied:

$$\sigma_{DY\,pA}^{corr} = \sigma_{DY\,pA}^{meas} \cdot \frac{A \cdot \sigma_{DY\,pp}^{calc}}{\sigma_{DY\,pA}^{calc}} \tag{4.35}$$

In this way the scaling factors taking into account energy, rapidity and isospin dependence can be computed.

cross sections (nb)	$E_p = 200$ GeV	$E_p = 450$ GeV	**p p**
σ_{pp}	0.0296	0.0555	$-0.4 < y^* < 0.6$
σ_{pp}	0.0246	0.0483	$0 < y^* < 1$
cross sections (nb)	$E_p = 200$ GeV	$E_p = 450$ GeV	**p D**
σ_{pD}/A_D	0.0326	0.0584	$-0.4 < y^* < 0.6$
σ_{pD}/A_D	0.0281	0.0521	$0 < y^* < 1$

Table 4.5: DY cross sections in p-p and p-D interactions calculated using MRS 43 in the invariant mass window $2.9 < m_{DY} < 4.5$

Concerning the J/ψ , since its production is mainly due to gluon fusion, no isospin dependence has to be taken into account. The procedure used for the comparison of data taken at different $\sqrt{s}$ and in different rapidity windows will be described in Section 6.2.

cross sections (nb)	$E_p = 200$ GeV	$E_p = 450$ GeV	**p Be**
σ_{pBe}/A_{Be}	0.0329	0.0588	$-0.4 < y^* < 0.6$
σ_{pBe}/A_{Be}	0.0285	0.0525	$0 < y^* < 1$
			p Al
σ_{pAl}/A_{Al}	0.0327	0.0585	$-0.4 < y^* < 0.6$
σ_{pAl}/A_{Al}	0.0282	0.0522	$0 < y^* < 1$
			p Cu
σ_{pCu}/A_{Cu}	0.0329	0.0587	$-0.4 < y^* < 0.6$
σ_{pCu}/A_{Cu}	0.0284	0.0524	$0 < y^* < 1$
			p Ag
σ_{pAg}/A_{Ag}	0.0330	0.0588	$-0.4 < y^* < 0.6$
σ_{pAg}/A_{Ag}	0.0286	0.0526	$0 < y^* < 1$
			p W
σ_{pW}/A_{W}	0.0332	0.0590	$-0.4 < y^* < 0.6$
σ_{pW}/A_{W}	0.0288	0.0528	$0 < y^* < 1$
			p U
σ_{pU}/A_{U}	0.0333	0.0591	$-0.4 < y^* < 0.6$
σ_{pU}/A_{U}	0.0289	0.0529	$0 < y^* < 1$

Table 4.6: DY cross sections in different p-A interactions calculated using MRS 43 in the invariant mass window $2.9 < m_{DY} < 4.5$

cross sections (nb)	$E_S = 200$ GeV	**S U**
σ_{SU}	188.	$0 < y^* < 1$
$A_S \cdot A_U\, \sigma_{pp}$	187.	$0 < y^* < 1$

Table 4.7: Cross sections for DY production in Sulfur on Uranium collisions at the beam energy of $200\, A \cdot GeV$ and invariant mass window $2.9 < m_{DY} < 4.5$

Collisions	Isospin correction
p D	0.950
p Be	0.944
p Al	0.949
p Cu	0.945
p Ag	0.944
p W	0.941
p U	0.939

Table 4.8: Isospin correction factors for DY production in the invariant mass window $2.9 < m_{DY} < 4.5$ from $E_p = 450\, GeV$, $-0.4 < y^* < 0.6$ to $E_p = 200\, GeV$, $0 < y^* < 1$ calculated using structure function MRS 43 for both projectile and target.

Collisions	$A_{y,E}$ rapidity and energy	A_I isospin
p p	0.443	1.
p D	0.481	0.875
p Be	0.485	0.863
p Al	0.482	0.872
p Cu	0.484	0.866
p Ag	0.486	0.860
p W	0.488	0.854
S U	//	1.00

Table 4.9: Scaling factors for DY production in the invariant mass window $2.9 < m_{DY} < 4.5$ from $E_p = 450\,GeV$, $-0.4 < y^* < 0.6$ to $E_p = 200\,GeV$, $0 < y^* < 1$ calculated using structure function MRS 43 for both projectile and target.

Chapter 5

Data analysis

In this chapter the analysis tools described in the previous chapters are applied to the NA50 p-A experimental data. Basically, the contributions of the various physical processes to the measured invariant mass spectra are extracted by means of a fitting procedure. Charmonia and DY cross sections, as well as ratios of cross sections are estimated. Finally statistical and systematic errors on the results are discussed.

5.1 Principles

The dimuon invariant mass spectrum is the sum of different contributions. The combinatorial background and the empty target contribution are determined by prior knowledge; the others (signals) are extracted by means of a fit. The fits are performed on the raw invariant mass spectra. The fitting function takes into account all the contributions: the signals and the two fixed components. This allows to preserve the poissonian behaviour of the bin content[1] and consequently the maximum likelihood method can be used for the fits.

5.2 The fitting methods

As it has already been pointed out in Chapter 4, the Monte-Carlo simulation slightly underestimates the resolution on the invariant mass of muon pairs and therefore is not able to reproduce exactly the shape of the invariant mass spectrum of the reconstructed events. While this effect is almost negligible for the components of the spectrum that have a smooth shape the simulated line shape of the resonance peaks is narrower than the experimental one.

To account for this effect the Monte Carlo shapes have to be slightly adjusted to properly fit the experimental data. Various smearing methods can be adopted for this purpose.

A good description of the J/ψ line shape is not really essential for the correct estimation of the number of J/ψ itself. In fact, given the low background environment in mass region around 3 GeV/c^2 , the number of J/ψ could be estimated easily with an event counting procedure, i.e. without any fit.

On the contrary the description of the shape of the J/ψ has a strong influence on the estimation of the other components of the spectrum. As will be clear in the following, this is particularly true for the ψ' .

5.2.1 "Standard" resonance smearing

In this section I will address a method that has been used to adjust the resonance shapes. I will call it the "standard smearing" method.

As it has been explained in Section 4.6 the line shape of the reconstructed J/ψ mass is a gaussian-like function:

[1] In fact the sum of poissonian distributions does still have a poissonian distribution while the difference doesn't.

$$\frac{dN_\psi}{dM} = par_1 * e^{-\frac{1}{2}\left(\frac{M-par_2}{\sigma}\right)^2} \tag{5.1}$$

where σ is a function of the independent variable M . To properly describe the simulation output a total of 11 parameters are tuned on the simulations. In the central part the σ function is constant (i.e. the resonance has a gaussian shape) while outside its tails broaden.

When fitting the experimental data some of these 11 parameters are left free in order to compensate for the difference between the real and the simulated resonance. In Particular:

- the pole position of the ψ has to be left free. This allows to compensate a possible shift of the value of the magnetic field with respect to the nominal one and possible incorrect estimations in the compensation of the energy loss of the muons in the hadron absorber (1 parameter).
- The width of the psi in the central region has to be left free because the Monte Carlo simulation underestimates the experimental value (1 parameter).
- The fitted tails of the ψ (see Section 4.6.1) use as a scaling parameter the width of the resonance in the central part. This tail scaling is a highly non linear function of the width of the ψ so once the J/ψ width is left free the effects on the tails must be carefully kept under control. In the "standard" smearing method this is done as follows:

  1. the parameter that rules the tail scaling is not the fitted experimental width of the J/ψ but is still the simulated width,
  2. the starting points of the non-gaussian tails are left free in the fit. Together with condition 1 this ensures that such tails are not overestimated (2 parameters). In Figure 5.1 the effect of uncontrolled scaling of the tails is shown.
  3. To get better agreement with data one must however enlarge a little the resonance tails. This is done adding to the σ function a constant term $\Delta\sigma$. This is not a further free parameter but it is the same smearing that has been added in the central region to stick to the experimental width, i.e.: $\Delta\sigma = \sigma_{experimental} - \sigma_{simulated}$ (in the central region).

To summarise four parameters (of the final fit) are left free to account for the smearing of the shape of the J/ψ :

1. mass ($FPar_4$)

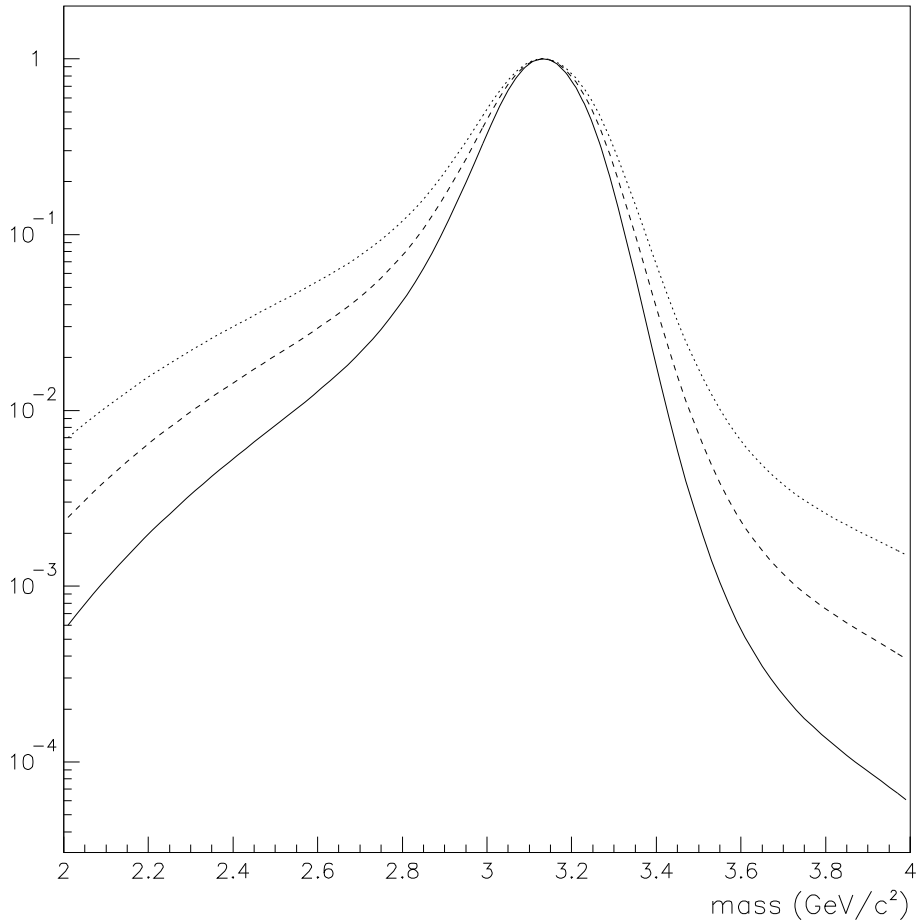

Figure 5.1: Uncontrolled influence of the central width of the fitted J/ψ on the non-gaussian tails. The solid line has $\sigma = 0.090$ GeV/c^2 from Monte-Carlo p-Al simulation, the dashed line has $\sigma = 0.100$ GeV/c^2 , the dotted line has the experimental width $\sigma = 0.110$ GeV/c^2 extracted from p-Al data.

2. width ($FPar_5$)
3. left and (y_1)
4. right tail starting points (y_2)

Parameters 3. and 4. are rather expressed in terms of fraction of the J/ψ mass:

$$\begin{aligned} y_1 &= FPar_7 * m_\psi \\ y_2 &= FPar_8 * m_\psi \end{aligned}$$

In Figure 5.2 the value of the σ function for the J/ψ extracted from the Monte-Carlo simulation is compared with the one adjusted on the p-Al data.

Since one expects the same kind of broadening for the real ψ' with respect to the simulated one, we propagate the smearing on the J/ψ resonance to the ψ' , since the events in the measured ψ' peak can not constrain the resonance shape by themselves due to the small statistics.

The propagation is done in the following way:

- the mass difference between ψ' and J/ψ is fixed from Monte-Carlo simulation,
- the width in the gaussian region is adjusted according this formula:

$$\sigma_{\psi'}^{FIT} = \left(\frac{\sigma_{\psi'}^{SIM}}{\sigma_{\psi}^{SIM}} \right) \sigma_{\psi}^{FIT}$$

- the tails of the ψ' are treated in the same way as for the J/ψ and the starting points of the tails are determined using the equations:

$$\begin{aligned} y'_1 &= FPar_7 * m_{\psi'} \\ y'_2 &= FPar_8 * m_{\psi'} \end{aligned}$$

5.2.2 Another fitting procedure: "uniform smearing"

Of course the results could be sensitive to the arbitrary choice of the smearing method. It is therefore useful for the estimation of the systematic errors to adopt at least another smearing method for the resonances.

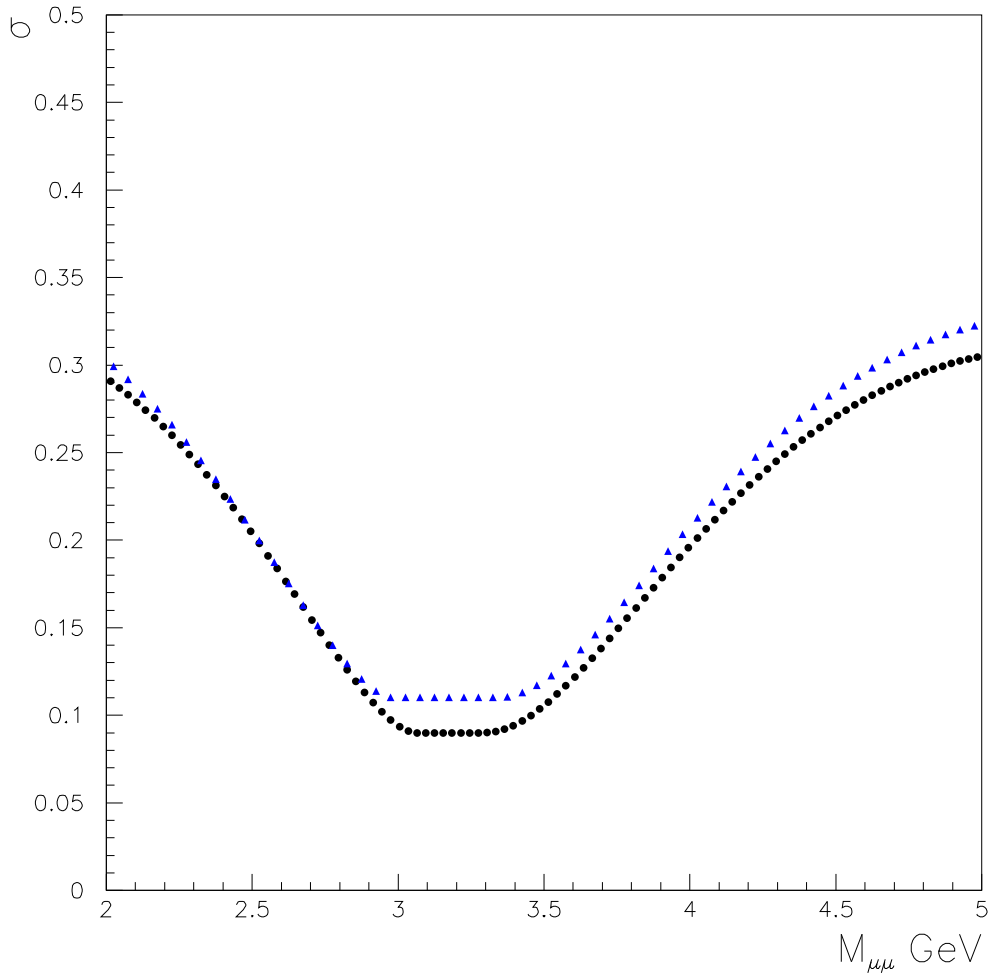

Figure 5.2: The value of the $\sigma(M)$ for the reconstructed mass J/ψ resonance in p-Al collisions (see Equation 5.1). The closed circles refer to the simulation output while the blue triangles are for the the line shape resulting from the fit to the experimental data. The pole position of the J/ψ resonance is 3.132$\pm$ 0.001 GeV/c^2 in the simulation and 3.096$\pm$ 0.001 GeV/c^2 from the fit to the experimental data.

The method presented in this section is somehow complementary to the previous one. In this case we don't focus on the tails of the J/ψ shape but an "uniform" smearing is applied all over the mass spectrum. All parts of the resonance spectrum are treated in the same way by adding a Gaussian noise to the reconstructed invariant mass coming from J/ψ simulation.

Even if the resolution of the spectrometer is not constant over the whole mass range, this is approximately true for the restricted mass region corresponding to the charmonia. In this method the $\mu^+\mu^-$ invariant mass for J/ψ simulated events is considered. To every value m_i a smearing contribution Δm_i is added. This is extracted from a distribution of zero mean and a width varying from 40 to 60 MeV, depending on the target type. The resulting values for the smeared mass $(m_i + \Delta m_i)$ are used to build the new line shape. The resulting mass shape is sampled and is used directly in the fit interpolating the simulated points with a second degree polynomial.

In this case the shapes of the resonances are adjusted prior to the final fit. The width of the smearing distribution is chosen in order to get the minimum $\chi^2/n.d.f.$ in the central zone of the J/ψ line shape. In this case the same smearing is applied for the ψ' as for the J/ψ . In the final fit to the invariant mass spectrum only the signal normalisations and the position of the J/ψ pole are left free, the position of the the ψ' pole is scaled as in the previous method. Hence only five parameters have to be estimated; i.e.:

1. the DY normalisation,
2. the number of J/ψ ,
3. the number of ψ' ,
4. the position of the pole of the J/ψ
5. the $D\overline{D}$ normalisation.

In Figure 5.3 the effect of two smearing methods on the J/ψ line shape is compared for two targets. The shapes for each target differ in the tail region. We have noted that the differences between the two methods decrease with the mass number of the target.

5.3 Parameter correlations

The parameters resulting from the fit are correlated, as shown in Table 5.1. The most important correlations are the ones among the J/ψ parameters that manage to adjust the shape to data and the strong correlation between the $D\overline{D}$

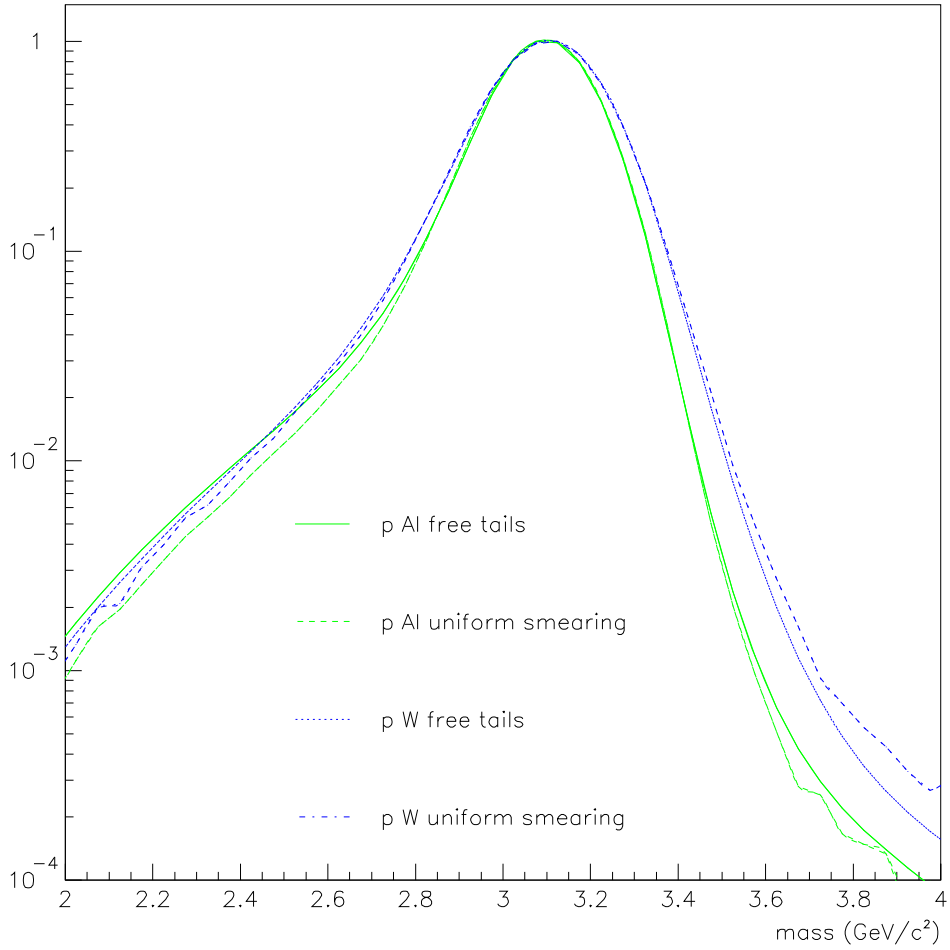

Figure 5.3: Comparison between smeared line shapes for the J/ψ for the two methods and for two nuclei. The "standard" smearing leads to fatter tails in p-Al while for p-W the situation is mixed.

normalisation and DY normalisation. This is a very delicate point in our fitting procedure because it shows that indeed there is a correlation between the high mass region, where DY is the dominant contribution, and the intermediate mass region where the charm contribution is important.

The DY normalisation is mainly determined by the events in the high mass region (above 4.5 GeV/c^2 where DY is the only contribution) while the $D\overline{D}$ is important in the intermediate mass region where it is quantitatively comparable to DY . The correlation between these two parameters reflects the fact that $D\overline{D}$ is not the dominant component in any region of the spectrum so that it can not be easily constrained without ambiguity. Moreover the intermediate mass region contains many signal sources and therefore different contributions of the various signals can describe equally well this region. Through the correlation between $D\overline{D}$ and DY , possible problems in the description of this intermediate mass region can influence to some extent the estimation of the Drell-Yan normalisation.

This point will be carefully investigated in the following sections.

In Table 5.2 the error matrix for the "uniform smearing" method is shown. The correlation between $D\overline{D}$ and DY is important also in this case.

5.4 Error calculation

In order to give a proper error estimate one has to take into account the correlation between the different parameters.

The variance of an estimator f that is function of the parameters of the fit $FPar_i$ is:

$$\sigma_f^2 = \sum_{i=1}^{NPar} \sum_{i=1}^{NPar} \frac{\partial f}{\partial FPar_i} \frac{\partial f}{\partial FPar_j} \sigma_i \sigma_j C_{ij}$$

where:

- f can be, for example, the number of J/ψ , the number of ψ' , the number of DY pairs, or the ratio ψ/DY
- $NPar$ is the number of free parameters
- σ_i are the uncertainties on each parameter $FPar_i$
- C_{ij} is the correlation coefficient between parameter i and parameter j

	DY norm.	J/ψ norm.	ψ' norm	m_ψ	σ_ψ	$D\overline{D}$ norm.	left tail	right tail
DY norm.	1.0000	-0.0333	-0.1960	-0.0340	-0.0001	*-0.5182*	-0.0939	0.3192
J/ψ norm.	-0.0333	1.0000	0.0020	0.2189	*-0.6146*	-0.0151	0.3074	-0.3055
ψ' norm	-0.1960	0.0020	1.0000	0.0100	0.0357	0.0366	-0.0110	0.2290
m_ψ	-0.0340	0.2189	0.0100	1.0000	*-0.5045*	-0.0924	*0.6048*	0.2063
σ_ψ	-0.0001	*-0.6146*	0.0357	*-0.5045*	1.0000	0.0719	*0.7580*	*0.5459*
$D\overline{D}$ norm.	*-0.5182*	-0.0151	0.0366	-0.0924	0.0719	1.0000	-0.2291	-0.1891
left tail	-0.0939	0.3074	-0.0110	*0.6048*	*0.7580*	-0.2291	1.0000	-0.4303
right tail	0.3192	-0.3055	0.2290	0.2063	*0.5459*	-0.1891	-0.4303	1.0000

Table 5.1: Error matrix for the "standard" fitting method. These values refer to a fit on the p Al 1999 spectrum. The unity diagonal terms are written in green while in red italics are written those terms that are greater than 0.5 .

	DY norm.	N. ψ	N. ψ'	m_ψ	$D\overline{D}$ norm.
DY norm.	1.0000	-0.1819	-0.3757	-0.0133	*-0.6019*
N. ψ	-0.1819	1.0000	0.0162	-0.0321	0.0125
N. ψ'	-0.3757	0.0162	1.0000	-0.0249	0.1527
m_ψ	-0.0133	-0.0321	-0.0249	1.0000	0.0480
$D\overline{D}$ norm	*-0.6019*	0.0125	0.1527	0.0480	1.0000

Table 5.2: Error matrix for the "uniform smearing" fitting method. These values refer to a fit on the p Al 1999 spectrum. The unity diagonal terms are written in green while in red italics are written those terms that are greater than 0.5 .

5.5 Fits on the five spectra

In Figures 5.4-5.8 the fits on the experimental spectra are plotted. Data are binned in 50 MeV bins. The events have been selected with the criteria described in Section 3.3. The events fall in the nominal acceptance of the NA50 experiment for 450 GeV/c beam momentum:

$$-0.4 < y^* < 0.6$$

$$|\cos\theta_{cs}| < 0.5$$

as explained in Section 3.4. To obtain these spectra a 1% cut on $PROB(P * DTarg)$ distribution has been applied. The refined version of the global cut estimation has been used as explained in Section 3.3.4. This is, a priori, a more correct way to perform the estimation of the $PROB(P * DTarg)$ variable but it has been shown that the fit results do not change significantly using the standard global cut estimation or the refined one.

The "R factor" for background estimation has been calculated as reported in Section 4.8.

The range of the fits is between 2 GeV and 8 GeV for all the plots. We have checked that fit results are stable when the starting point of the fit is in the region 2 ± 0.2 GeV.

I do not include in the fit the low mass region for several reasons. First of all, the validity of calculations of hard processes like DY in a "soft" range as the low mass region is, is questionable. Secondly, even if we have reasonable description of $D\overline{D}$ and combinatorial background below $M \sim 2\,\mathrm{GeV/c^2}$, we have seen (Section 5.3) that, via the DY, a correlation between high mass and low mass exists. Since we are focusing in this analysis on the high mass region, we want to avoid that possible systematic errors on the shapes and normalisation of the processes in the

low mass region, which we know to be of the order of 20%, influence too much the DY determination in the high mass region.

At the same time, we want to have a sizeable $D\overline{D}$ in our fitting range, since its incorrect evaluation could lead to systematic errors in the high mass region, especially concerning the ψ' determination. Therefore we can not start the fit at a much higher mass than 2 GeV/c^2 .

In Figure 5.9 the fit of the p Al 1999 data (Figure 5.5) is shown again, together with the contribution of each bin to the global χ^2 . For each bin used in the fit the variable

$$\frac{(entries - estimated)^2}{estimated} \tag{5.2}$$

is plotted. This positive quantity is given the sign of

$$(entries - estimated)$$

to identify more precisely undershoot or overshoot zones ("χ^2 with sign" in the plots).

In the last plot of Figure 5.9 the χ^2 defined in Equation 5.2 is integrated up to the n^{th} bin. This integrated χ^2 is compared with lines representing 1 χ^2 unit gain for every bin[2]. The same kind of plot is shown for all the targets in Figure 5.10.

In Figure 5.11 and 5.12 the fits to the p Be 2000 and p W 1998 spectra with the "uniform smearing" method are shown. The study of the χ^2 contribution is also shown. One can see that the uniform smearing method gives better description of the J/ψ resonance when increasing of the Z of the target.

However, despite the poor $\chi^2/n.d.f.$ of the p Be 2000 fit with the uniform smearing procedure, it can be seen that all the contribution in excess comes from the a restricted region of the left tail of the J/ψ . The influence of this region on the estimation of the number of J/ψ is however limited. The bias on the number of J/ψ is of the order of 0.6% (comparing standard smearing, which gives better results for this target, with uniform smearing).

We also noted that the right tail of the J/ψ , that has an important influence on the ψ' normalisation, is well reproduced with both smearing methods.

[2]For simplicity in these plots the solid lines represent a contribution of 1 unit per bin to the total χ^2 and not 1 unit per degree of freedom.

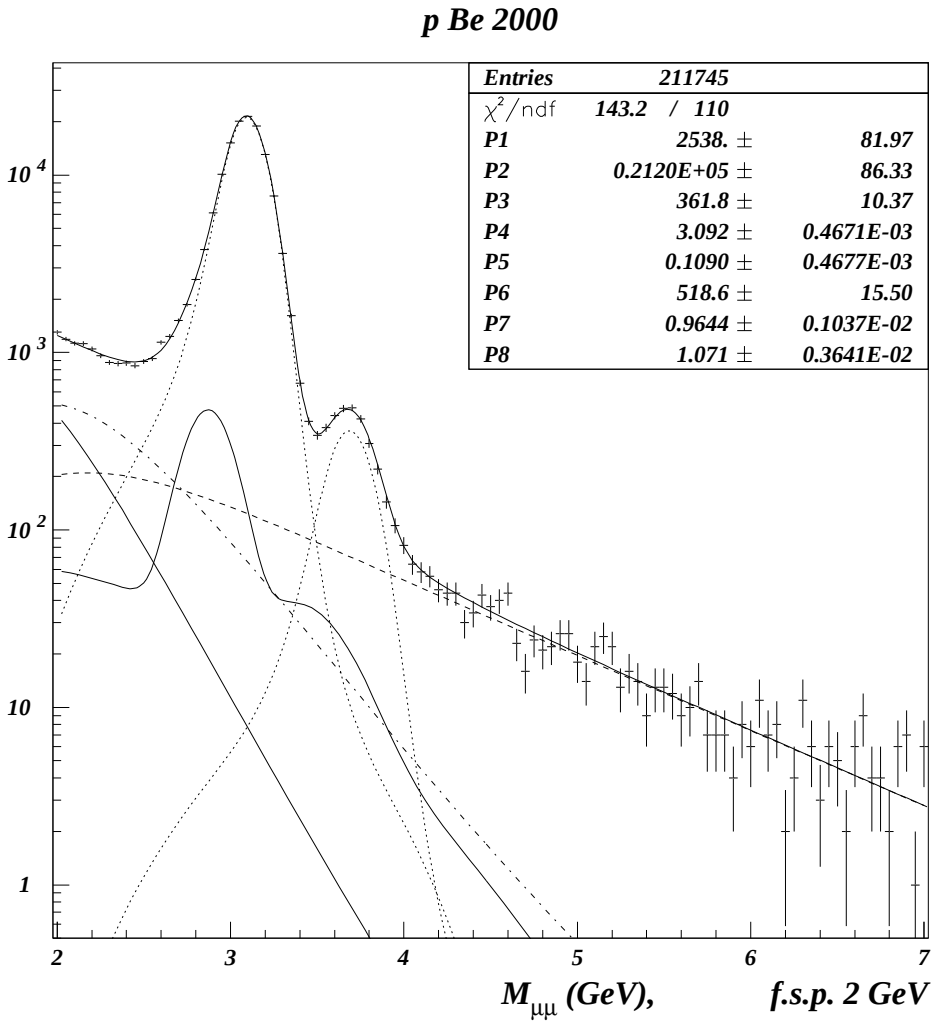

Figure 5.4: Fit on the p Be 2000 data, 1% global cut, DY shape calculated with MRS43, "standard" fitting method. The upper continuous line is the sum of all the signal contributions: J/ψ and ψ' resonances (dotted lines), the DY continuum (dashed line), the open charm continuum (dashed-dotted line), the background and empty target contributions (continuous lines). The number of entries in the mass range up to 10 GeV is shown. The fitted values of the parameters are shown. The starting point of the fit (f.s.p.) is indicated.

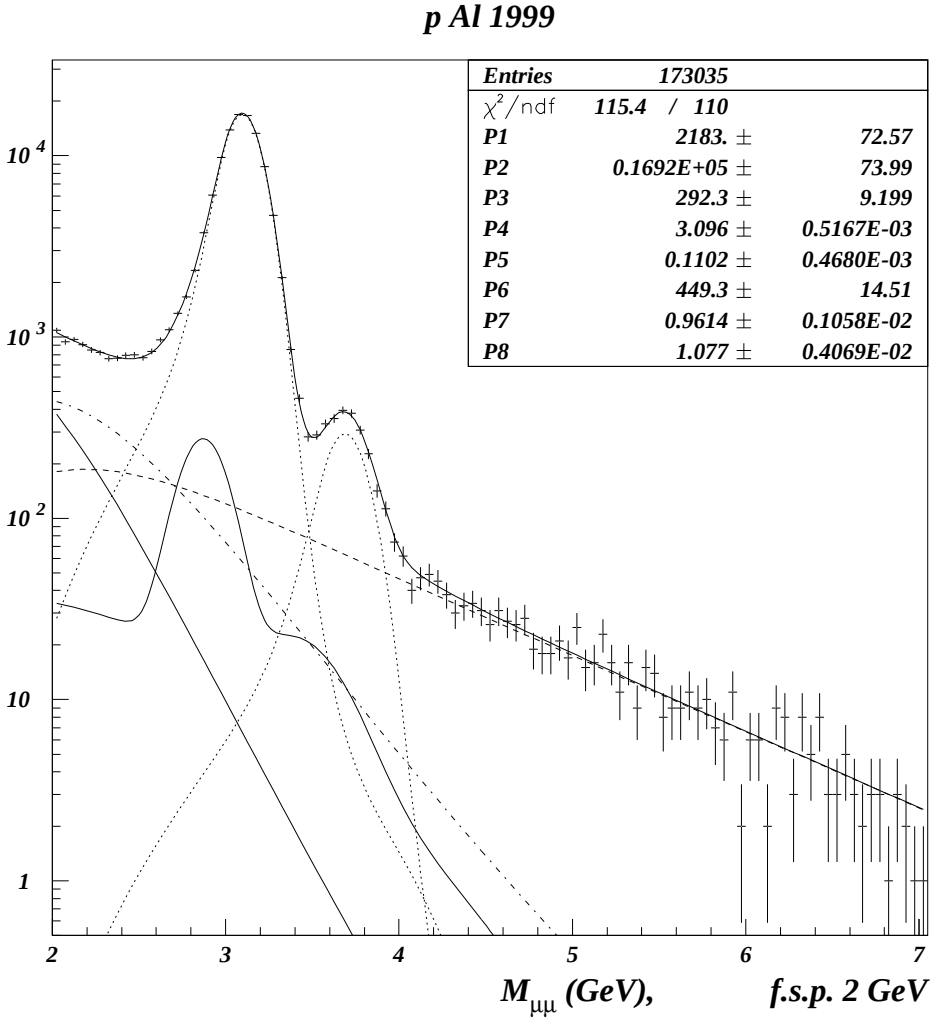

Figure 5.5: Fit on the p Al 1999 data with the "standard" fitting method. See Figure 5.4 for description.

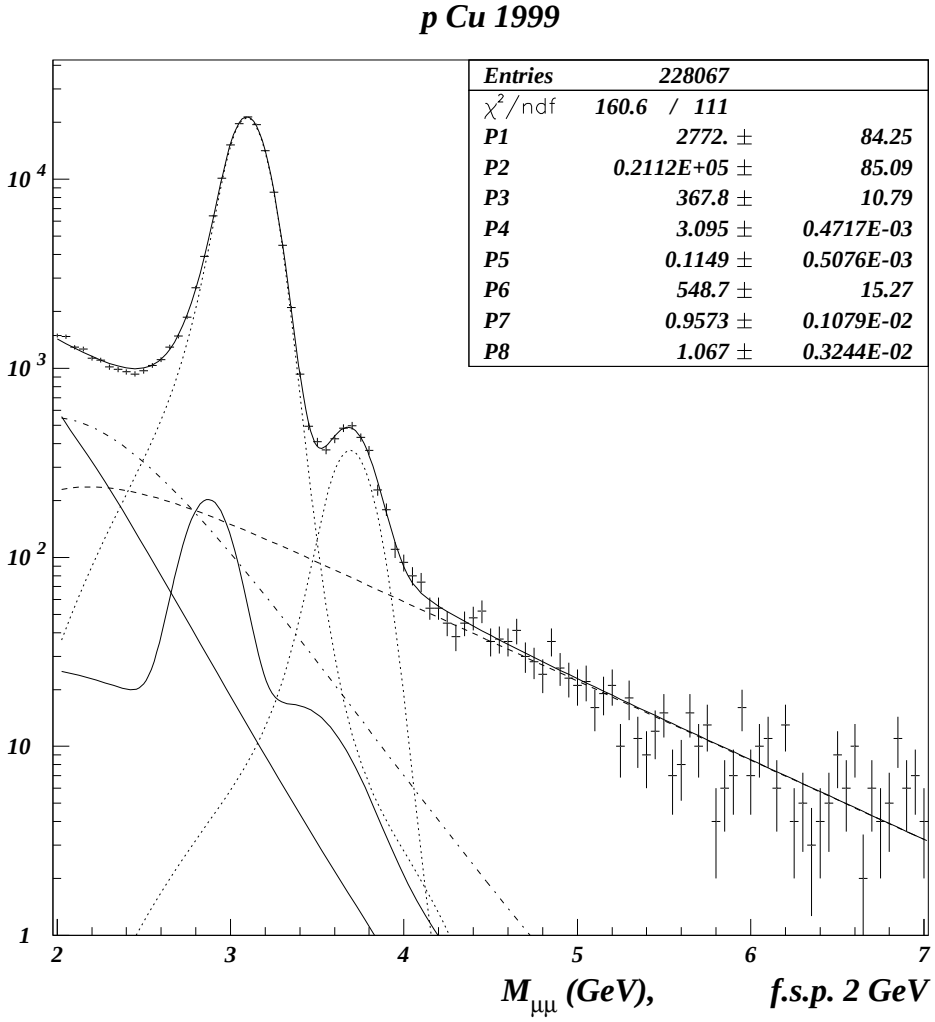

Figure 5.6: Fit on the p Cu 1999 data with the "standard" fitting method. See Figure 5.4 for description.

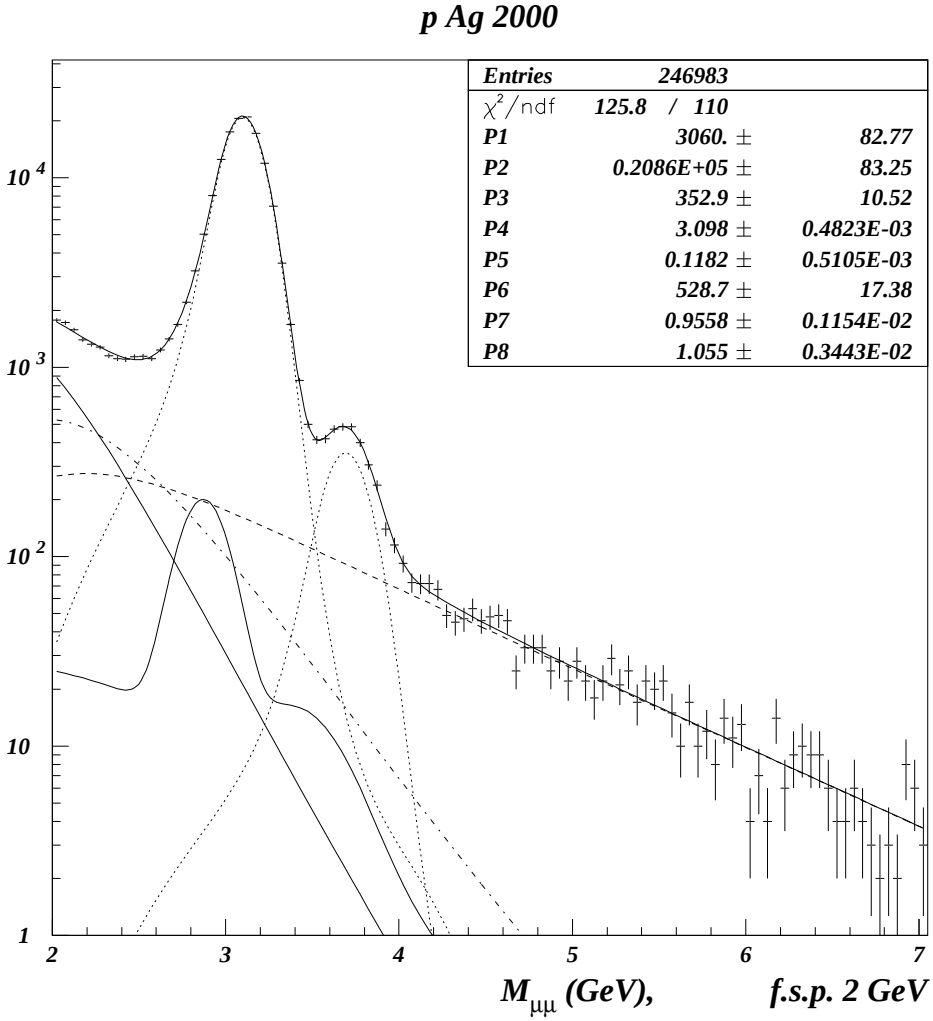

Figure 5.7: Fit on the p Ag 2000 data with the "standard" fitting method. See Figure 5.4 for description.

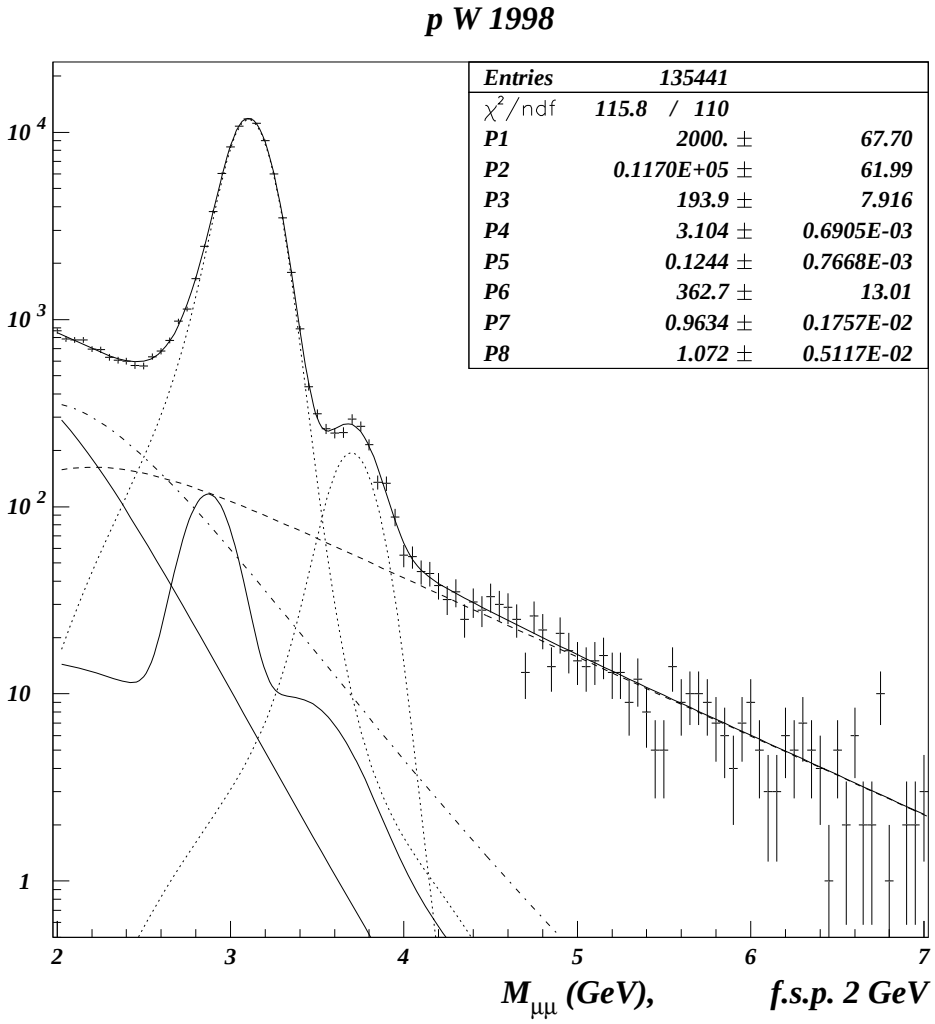

Figure 5.8: Fit on the p W 1998 data with the "standard" fitting method. See Figure 5.4 for description.

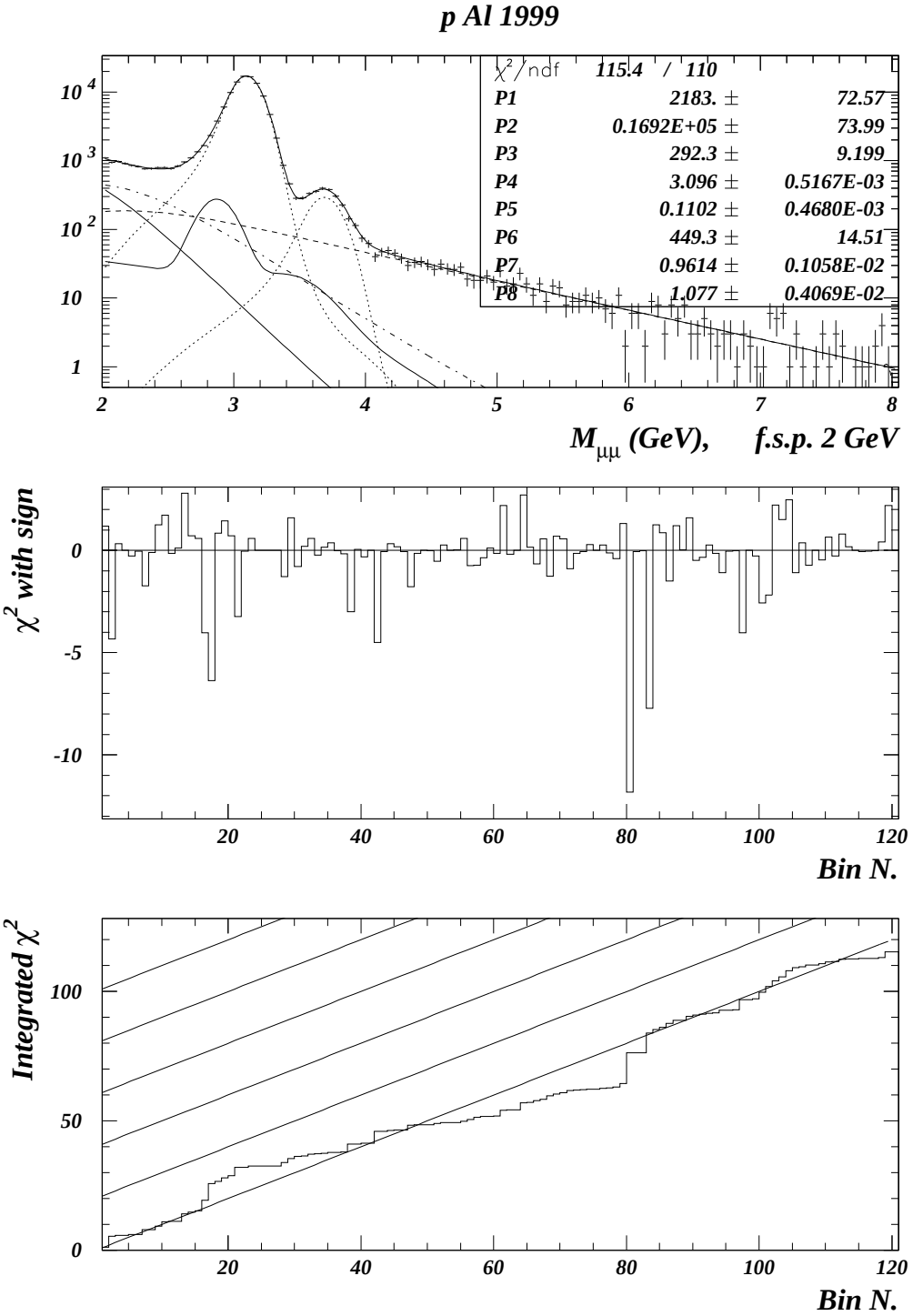

Figure 5.9: Fit on the p Al 1999 data, 1% global cut, DY shape calculated with MRS43, "standard" fitting method. The histogram of Figure 5.5 is shown together with the contribution to the fit χ^2 for each bin used in the fit: negative (positive) values means less (more) data than estimated from the fit. The integrated χ^2 in the same region is shown. The continuous lines represent for 1 unit χ^2 gain for each bin.

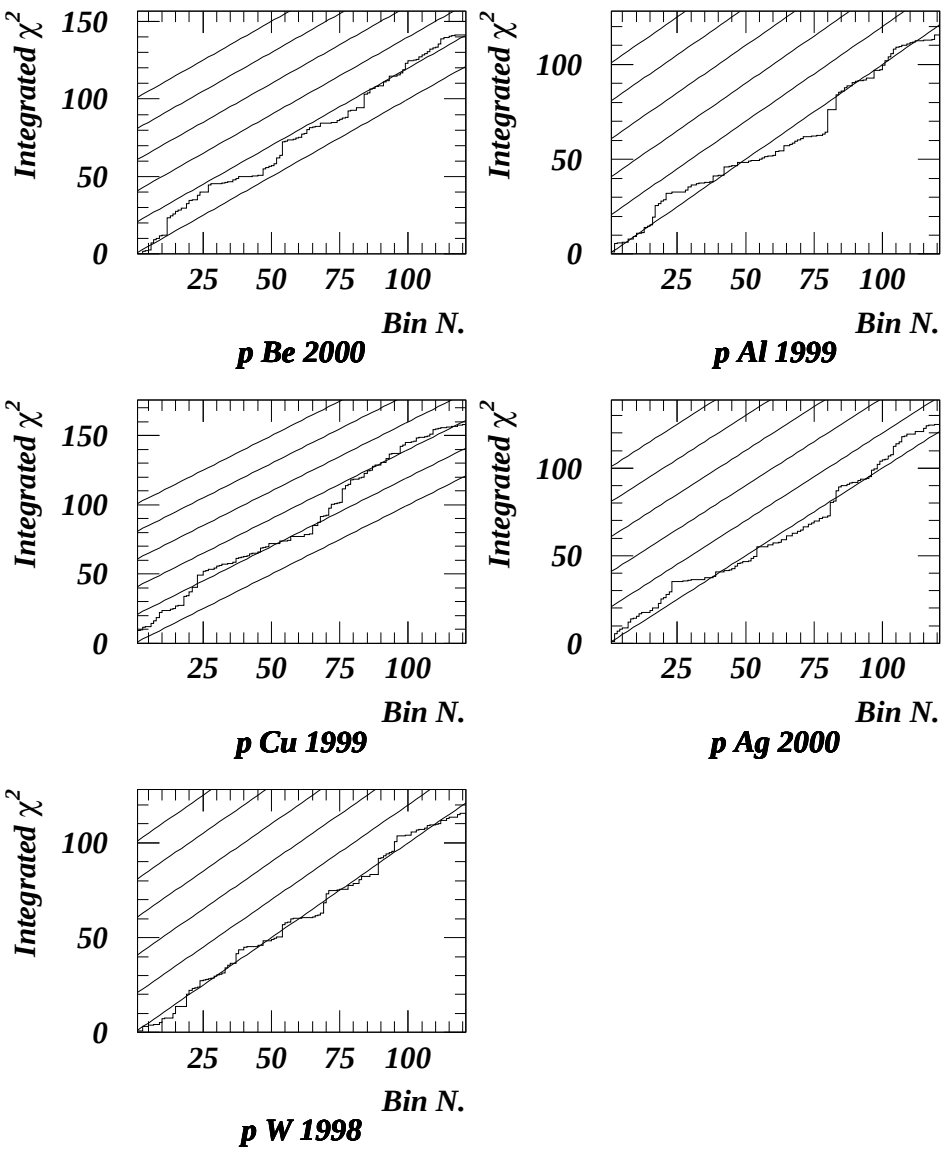

Figure 5.10: The integrated χ^2 is shown for the five data sets of Figures 5.4-5.8. The continuous lines represent 1 unit χ^2 gain for each bin.

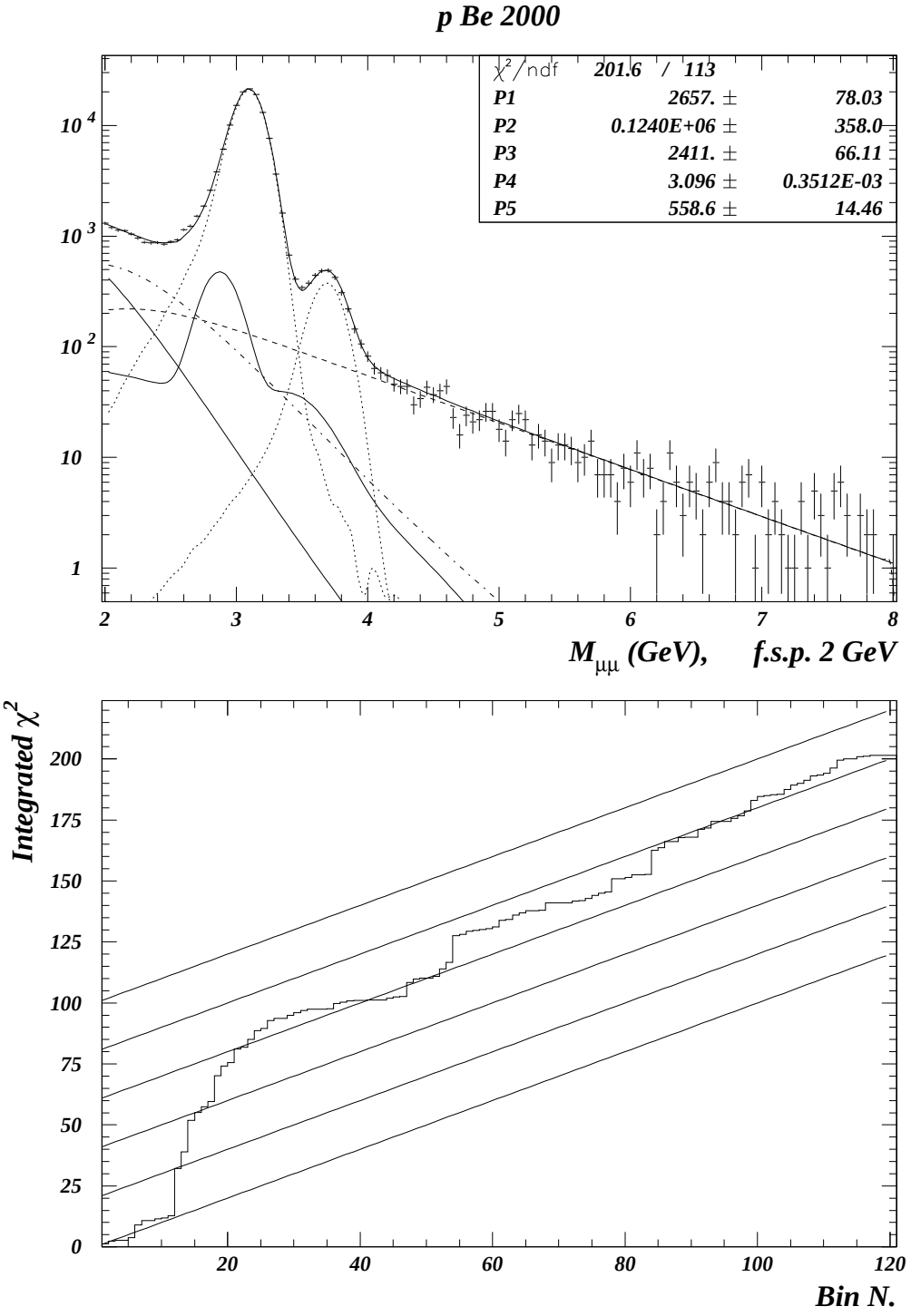

Figure 5.11: Fit on the p Be 2000 data sample, 1% global cut, DY shape calculated with MRS43, "uniform" fitting method. The upper continuous line is the sum of all the signal contributions: J/ψ and ψ' resonances (dotted lines), the DY continuum (dashed line), the open charm continuum (dashed-dotted line), the background and empty target contributions (continuous lines). The fitted values of the parameters are shown. The starting point of the fit is indicated. A plot of the integrated χ^2 over the range of the fit is shown.

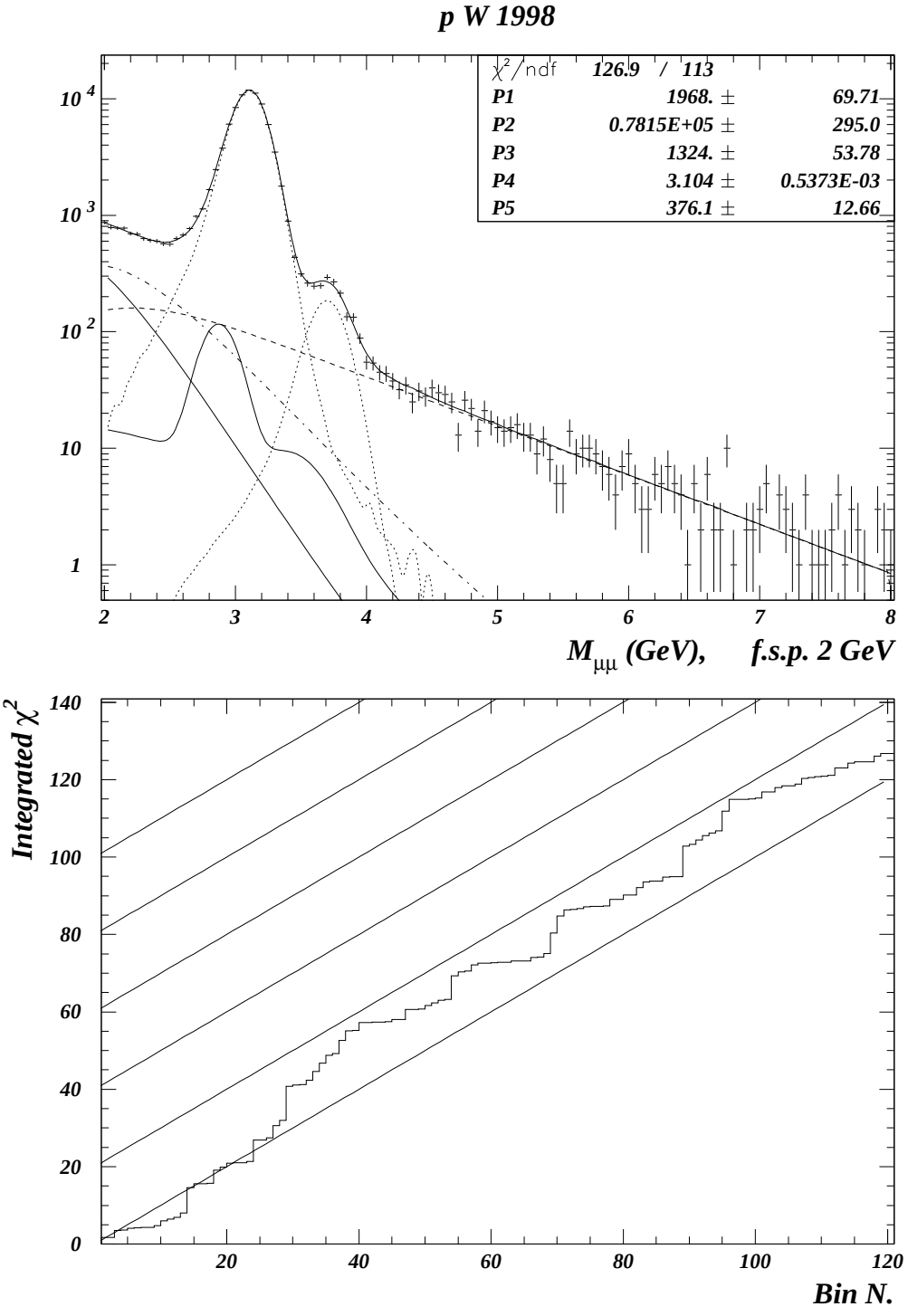

Figure 5.12: Fit on the p W 1998 data sample, 1% global cut, DY shape calculated with MRS43, "uniform" fitting method. See Figure 5.11 for description.

5.6 Results

In Table 5.3 and Table 5.4, the results of the two fitting procedures are summarised for the five target nuclei.

The fitted values for J/ψ , ψ' and DY production are shown. The DY production is integrated over the mass range between 2.9 and 4.5 GeV to make easier the comparison with previously published NA50 results.

The ratios of ψ/DY and ψ'/ψ are given. These two values have been corrected for acceptances (that are reported in Table 4.3). The quoted errors are estimated according to the procedure explained in Section 5.4, i.e. taking into account the correlations between the different fitted parameters.

The branching ratios of J/ψ and ψ' have not been factorised.

The R factor has been fixed by means of simulations which take into account the beam intensities of each data taking (see Section 4.9).

The ratio $D\overline{D}$ /DY is defined as follows:

$$\frac{\int_{1.5}^{7} \frac{dN_{D\overline{D}}}{dM} dM}{\int_{1.5}^{7} \frac{dN_{DY}}{dM} dM} \frac{Acc_{DY}}{Acc_{D\overline{D}}} \tag{5.3}$$

where M is the invariant mass of the dimuon pair expressed in GeV and Acc_{DY} and $Acc_{D\overline{D}}$ are the acceptances for the two processes in the mass range between 1.5 and 7 GeV.

The fitted values are compatible with a previously published value by the NA50 collaboration: 4.2± 0.9. However our two sets of results both show a systematic trend with the mass number of the target.

The $D\overline{D}$ and DY production are both hard scattering processes. In principle, if there are no re-absorption effects, they should both scale with the mass number of the target so that this ratio should remain constant. On the contrary we observe a decrease of $D\overline{D}$ /DY with the mass number of the target. The J/ψ suppression should rather increase the number of $D\overline{D}$ pairs as a function of A but quantitatively the effect is very small. In fact the J/ψ cross section is much smaller than open charm cross section. In the framework of the "Colour evaporation model" it is of the order of a few percent of the total cross section for $c\overline{c}$ production (the small charm contribution to the invariant mass spectrum is only due to the low branching ratio for the decay into muons).

The ratio DYHM refers to the number of DY pairs between 5 and 8 GeV. The number of entries between these mass limits are compared with the ones estimated from the fit and the ratio of entries over estimated (e/c) is presented. This region of the spectra has been chosen because it represents a pure sample of DY events.

	p Be 00	p Al 99	p Cu 99	p Ag 00	p W 98
J/ψ	124754 ± 400	100703 ± 400	130582 ± 420	132136 ± 370	78156 ± 290
ψ'	2429± 70	2016± 65	2509± 75	2458± 75	1392± 60
DY	2445± 80	2184± 70	2726± 80	3179± 85	1950± 70
ψ /DY	49.6± 1.6	46.3± 1.6	47.0± 1.4	41.4± 1.1	40.5± 1.4
ψ'/ψ	0.0168 ± 0.0005	0.0174 ± 0.0006	0.0166 ± 0.0005	0.0160 ± 0.0005	0.0153 ± 0.0006
R	1.12	1.13	1.10	1.09	1.14
$D\overline{D}$ /DY	3.90± 0.21	3.71± 0.22	3.70± 0.20	3.01± 0.17	2.92± 0.20
χ^2	1.30	1.05	1.45	1.14	1.05
DYHM	401	369	431	529	310
DYHM e/c	1.080	1.079	1.017	1.048	1.036

Table 5.3: Results for the "standard" fitting method. The number of J/ψ , ψ' , DY pairs from 2.9 GeV to 4.5 GeV are reported. The ratio ψ /DY and ψ'/ψ corrected for acceptances are reported. The fixed R factor used for the combinatorial background normalisation is reported. The ratio $D\overline{D}$ /DY, the χ^2 of the fits, the number of entries between 5 and 8 GeV and the ratio DYHM e/c are reported.

Given the low statistics in this high mass region the uncertainty on the number of DY pairs is between 4.3 and 5.7 %. All ratios "DYHM e/c" are marginally compatible with 1 (as it has been shown in Figure 5.10 the high mass region is quite well reproduced). However there seems to be a systematic underestimation of the number of entries by the fit.

These two facts suggest the presence of some systematic errors in the description of the DY and $D\overline{D}$ line shapes. This question has been investigated and will be analysed in detail in Sections 5.9, 5.11, and 5.12.

For cross section calculations we use more severe run selection, as explained in Section 3.7. The results of the "standard" method for this sample are reported in Table 5.5.

5.7 Uncertainties on the J/ψ and DY cross sections

Given the high statistics collected in the J/ψ region, the uncertainty on the number of J/ψ (see Table 5.3) is much smaller than the systematic errors connected with the normalisation. From previous studies by the NA50 Collaboration

	p Be 00	p Al 99	p Cu 99	p Ag 00	p W 98
J/ψ	123950 ± 400	99961 ± 310	129677 ± 400	131698 ± 400	78147 ± 290
ψ'	2411± 66	1923± 62	2477± 68	2442± 73	1324± 54
DY	2559± 75	2272± 72	2797± 79	3175± 87	1918± 67
ψ /DY	47.1± 1.4	44.1± 1.4	45.5± 1.3	41.4± 1.2	41.2± 1.5
ψ'/ψ	0.0168 ± 0.0005	0.0167 ± 0.0005	0.0165 ± 0.0005	0.0159 ± 0.0005	0.0145 ± 0.0006
R	1.12	1.13	1.10	1.09	1.14
$D\overline{D}$ /DY	4.03± 0.20	4.08± 0.22	4.11± 0.19	3.39± 0.17	3.39± 0.21
χ^2	1.78	1.48	1.61	1.21	1.12
DYHM	401	369	431	529	310
DYHM e/c	1.031	1.037	0.991	1.050	1.053

Table 5.4: Results for the "uniform smearing" fitting method. The number of J/ψ , ψ' , DY pairs from 2.9 GeV to 4.5 GeV are reported. The ratio ψ /DY and ψ'/ψ corrected for acceptances are reported. The fixed R factor used in the estimation of the combinatorial background normalisation is reported. The ratio $D\overline{D}$ /DY, the χ^2 of the fits, the number of entries between 5 and 8 GeV and the ratio DYHM e/c are reported.

	p Be 00	p Al 99	p Cu 99	p Ag 00	p W 98
J/ψ	95705 ± 360	84458 ± 310	104155 ± 360	104665 ± 340	45555 ± 220
ψ'	1860± 65	1686± 60	1959± 65	1948± 65	889± 40
DY	1880± 70	1865± 65	2156± 75	2576± 80	1155± 50
ψ /DY	49.5± 1.8	45.3± 1.7	47.4± 1.6	40.5± 1.3	39.9± 1.8
ψ'/ψ	0.0167 ± 0.0006	0.0173 ± 0.0006	0.0163 ± 0.0006	0.0160 ± 0.0005	0.0168 ± 0.0008
R	1.12	1.13	1.10	1.09	1.14
$D\overline{D}$ /DY	3.90± 0.24	3.71± 0.23	3.70± 0.22	3.01± 0.18	2.92± 0.25
χ^2	1.26	1.12	1.46	1.21	1.1
DYHM	309	319	341	432	185
DYHM e/c	1.082	1.093	1.010	0.946	1.018

Table 5.5: Results for the "standard" fitting method with run selection. The number of J/ψ , ψ' , DY pairs from 2.9 GeV to 4.5 GeV are reported. The ratio ψ /DY and ψ'/ψ corrected for acceptances are reported. The fixed R factor used for the combinatorial background normalisation is reported. The ratio $D\overline{D}$ /DY, the χ^2 of the fits, the number of entries between 5 and 8 GeV and the ratio DYHM e/c are reported.

	all runs	selected runs
p Be 2000	0.031	0.025
p Al 1999	0.016	0.017
p Cu 1999	0.021	0.018
p Ag 2000	0.026	0.022
p W 1998	0.065	0.030

Table 5.6: Relative uncertainties on the cross sections estimated from ψ /ARGO1 ratio. The severe run selection improves the stability of the dimuon yield.

these systematic errors have been estimated to be $\approx 7\%$. This value includes the different sources of systematic uncertainty:

- the calibration of the argon counters
- the estimation of trigger efficiency
- the estimation of reconstruction efficiency

In this analysis I tried to evaluate more precisely this systematic uncertainty, studying the stability of J/ψ production along time. In a run-by-run analysis the number of reconstructed J/ψ per count in the argon counters has been calculated. The number of J/ψ has been corrected for the reconstruction efficiency estimated by the reconstruction program and plotted versus the run number.

The dispersion of the $\psi/ARGO$ ratio can be used as a more careful estimation of the uncertainty on the cross section due to short range variations of reconstruction and trigger efficiencies, or to instabilities in the luminosity determination. When comparing results relative to the same period of data taking the dispersion of $\psi/ARGO$ ratio should be used as systematic error bars. On the contrary, when fitting together all the points taken in different periods the systematic errors should include all the sources.

In Figure 5.13 we show the $\psi/ARGO1$ ratio for the runs selected for cross section calculation.

The uncertainties on the ψ cross sections are calculated using the dispersion of the measured $\psi/ARGO$ values for every run[3]. In Table 5.6 the relative uncertainties are reported.

[3]The use of the error on the weighted mean instead of the $\psi/ARGO$ dispersion could lead to an underestimation of the fluctuations. Here we are not interested in determining the "average" performance of the apparatus. We are indeed interested in the estimation of the fluctuations of the performance of the apparatus along time and therefore the dispersion has been used. The run with low statistics are rejected from this calculation.

	ARGO1/ARGO2	ARGO1/ARGO3	ARGO2/ARGO3
1996	1.355	1.151	0.849
1998	1.229	1.122	0.912
1999	1.205	1.108	0.919
2000	1.233	1.126	0.913

Table 5.7: Stability of argon counters over the period 1996-2000, the 1996 values refer to the calibration runs.

The stability of the argon counter used for luminosity calculation can be monitored using the ratios between its counts and those of other beam counters. In Figure 5.14 the ratios of the different Argon counters versus the run number are shown and the mean values for each period are reported in Table 5.7. The ARGO2 and ARGO3 agree for the five periods of data taking, while ARGO1, which is the one commonly used for luminosity determination, shows a $\approx 2\%$ shift with respect to the other two in the 1999 runs. The ARGO2 is known to have calibration problems and this explains the big difference of the ratios ARGO1/ARGO2 and ARGO2/ARGO3 between 1998, 1999 and 2000 periods with the calibration runs at very low intensity of 1996.

To summarise the error on cross section calculation can be estimated as:

- oscillation of argon response between the different years of data taking: 2%,
- error on the estimation of reconstruction efficiency: 1%,
- error on the trigger efficiency: 2% ,
- residual short range fluctuations on dimuon yield: 1.5-3% depending on the target.

The error on the absolute calibration is estimated in a 4% from the stability of the ratio ARGO1/ARGO3 and is not included in the plots.

For the J/ψ cross section the statistical error is found to be negligible. For the DY, due to lower statistics, it is found to be comparable with the systematic error.

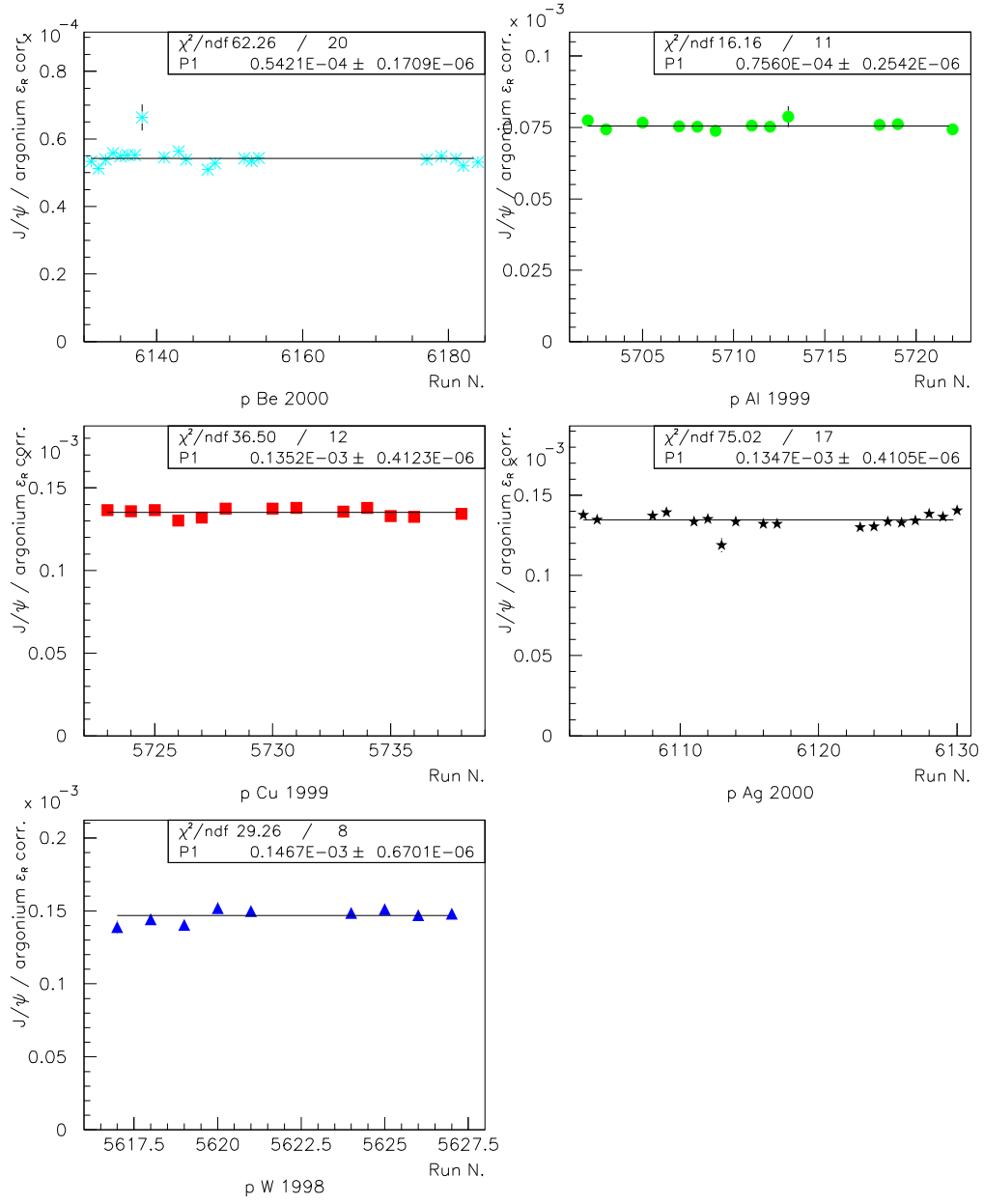

Figure 5.13: The $\psi/ARGO.1$ ratio for the selected runs, corrected for the estimated reconstruction efficiency.

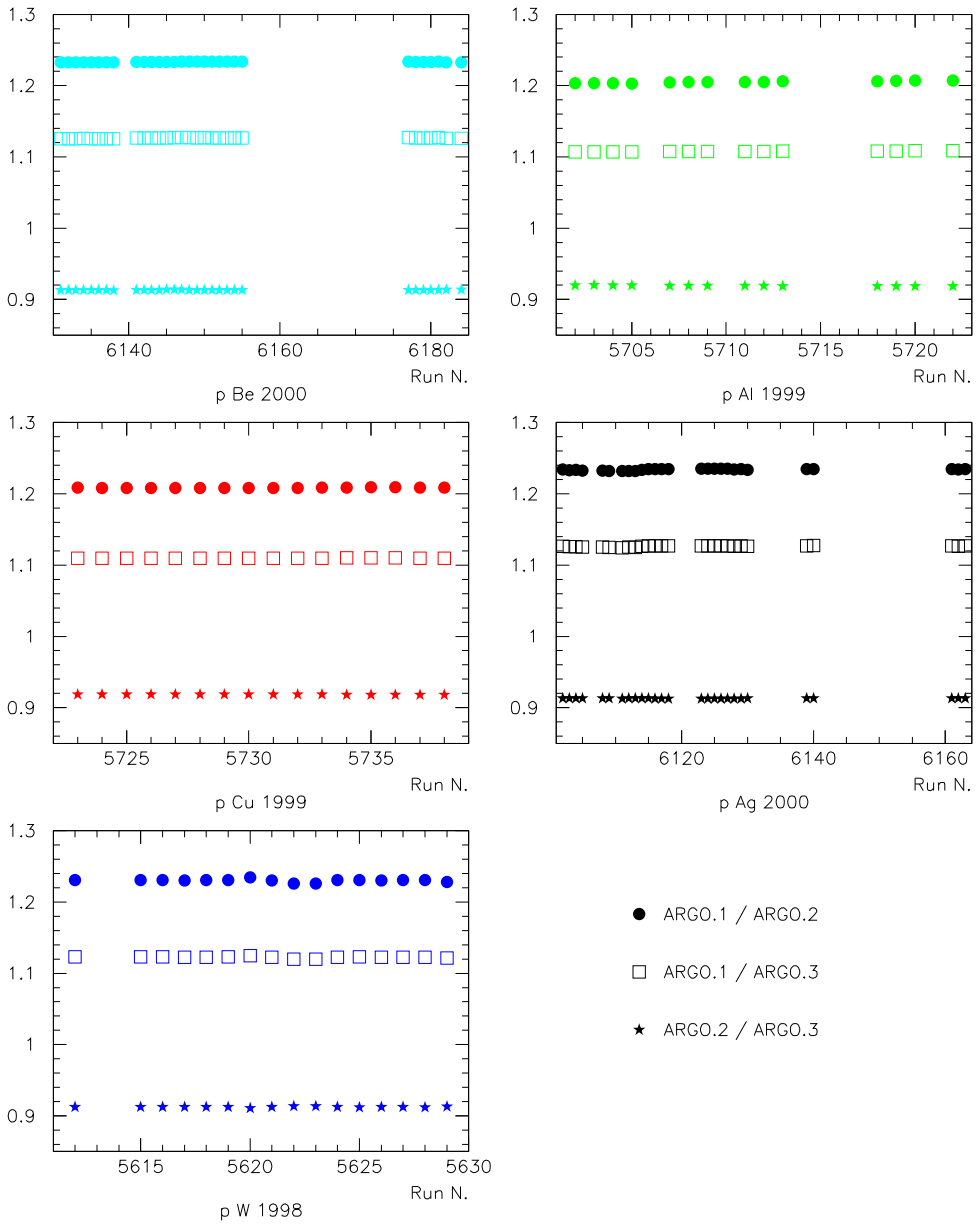

Figure 5.14: The ratios of the argon counter responses in the five periods.

5.8 The J/ψ , ψ' and DY cross sections

For the calculation of the J/ψ , ψ' and DY cross sections only the selected group of runs is used in order to have a data sample collected in very stable conditions of the apparatus. In Table 5.8 the target characteristics are summarised again and the calculation of the cross sections is shown for the "standard" fitting procedure.

In Figure 5.15 the J/ψ cross section per target nucleon is plotted against the target mass number and in Figure 5.16 the same is done for the ψ' .

In Figure 5.17 the cross section for DY per target nucleon integrated between 2.9 and 4.5 GeV is plotted. The isospin dependence of DY production has been corrected using MRS 43 structure function. This structure function has been calculated including the published results of the NA51 Collaboration about flavour asymmetry in the sea quarks ($\overline{u} \neq \overline{d}$) [16]. The resulting plotted cross section refers to a nucleus made of A protons, i.e. we plot the quantity:

$$\sigma_{pA}^{corrected} = \sigma_{pA}^{measured} \cdot \frac{A \cdot \sigma_{pp}^{calculated}}{\sigma_{pA}^{calculated}} \tag{5.4}$$

The measured cross sections are fitted with the function:

$$\sigma_{p-A} = \sigma_{p-p} * A^{\alpha}$$

where A is the mass number of the target.

The value of α is connected with nuclear effects. If $\alpha = 1$ the hard process does not suffer any absorption in the final state or shadowing (anti-shadowing) effect in the initial state.

The extracted α values for the J/ψ are given in the following table. Different fits to the cross section values have been used, namely:

- a fit to the NA50 proton nucleus points of this work:
  - using only the statistical errors on the number of J/ψ estimated from the fit,
  - including the systematic errors estimated from the ψ /ARGO dispersion and from the other sources as explained in the previous section,
  - with fixed global 7% error, i.e. using the previous estimation of the systematic error used in the NA50 experiment,
- a fit introducing a scaling factor between 1999 points and the other three points to take into account possible oscillations in the argonia calibration for that year, as data seem to suggest

The NA51 results are not included in the fits because the A^α parametrisation poorly approximates the correct calculation at low A when the α exponents is quite different from unity as for the J/ψ . Usually, in literature, the α value is extracted from a fit to proton-nucleus data only.

points used in the fit	α of the J/ψ	scaling factor	χ^2
NA50 with stat. errors only	0.925 ± 0.002		128.
NA50	0.925 ± 0.018		0.68
NA50 with old 7% error estimation	0.925 ± 0.029		0.31
NA50 with scaling factor	0.929 ± 0.019	1.065 ± 0.043	≈ 0

The nuclear dependence of J/ψ production extracted with these fits is very stable even changing the fitting strategy. The χ^2 of the fit reflects the fact that systematic errors may be overestimated. The introduction of the 7% systematic error on NA50 points seems to increase the overestimation of the errors. In spite of that the results do not change. The introduction of a scaling factor between the 1999 points and the other points does not change the results. This means that the measured α dependence of 1999 and 1998-2000 are compatible and the shift between the two data sets is due to some unknown uncertainty in the normalisation. The χ^2 in this case is very low because of the introduction of an additional parameter.

In Figure 5.15 we plot the fit to the proton nucleus data analysed in this work.

For the ψ' the nuclear dependence extracted from the fit (Figure 5.16) is reported in the following table. Due to the large statistical errors the fit with the introduction of a scaling factor between 1999 data sets and the other points is not meaningful and was not performed. A small difference between $\alpha_{J/\psi}$ and $\alpha_{\psi'}$ is present. This will be studied in detail in Section 5.15 where the ratio of ψ' and J/ψ cross sections is studied. This allows to reduce some of the systematic uncertainties present in the calculation of absolute cross sections. The comparison with published NA50 and NA51 results will be done, for the ψ'/ψ ratio, in Section 6.4.

points used in the fit	α of the ψ'	χ^2
NA50 with stat. errors only	0.914 ± 0.015	2.4
NA50	0.913 ± 0.024	0.94

For the DY the A^α dependence has been similarly extracted by means of a fit, but we also test the hypothesis $\alpha = 1$. The fit has been performed with three

different strategies similar to the ones used for the J/ψ . The results are quite stable. As for the ψ' the introduction of a scaling factor between 1999 data sets and the other points is not meaningful. All the measured α for the DY are compatible with unity.

points used in the fit		σ (pb)	χ^2	
NA50 with stat. errors only	$\alpha_{DY} = 0.996 \pm 0.016$		2.4	
NA50 with stat. errors only	$\alpha_{DY} = 1$	103.6 ± 1.7	1.8	hyp.
NA50	$\alpha_{DY} = 0.995 \pm 0.024$		0.99	
NA50	$\alpha_{DY} = 1$	103.6 ± 2.6	0.75	hyp.

From the results on DY cross sections we exclude strong shadowing effect. On the other hand such effects are not foreseen by theory as will be shown in Section 5.10. Therefore another way to study the J/ψ behaviour is through the ratio of J/ψ and DY cross sections. In this way most systematic errors on the normalisation cancel out.

5.9 A study of the slope of the DY spectrum

The results reported in Table 5.3 and Table 5.4 show that some systematic errors could be present in the description of the DY and $D\overline{D}$ line shapes.

As we know, the DY process is the only contribution to the high mass region of the invariant mass spectrum. The study of its line shape in this region can therefore be used to make a check of the Monte-Carlo simulation.

We have therefore studied the invariant mass spectra in the region between 4.5 GeV and 7. GeV and we have directly compared the slope measured in the experiment with the slope predicted by the simulation. The comparison is quite easy since in this region the spectra can be described by an exponential, i.e. with a single shape parameter.

In Figure 5.18 the five exponential fits are shown. The extracted slopes are reported in Table 5.9 where a comparison is made with three Monte-Carlo simulations of DY line shape.

Three structure functions sets have been used in the generation of DY pairs. The muons have been tracked through the spectrometer and then reconstructed. Cuts have been applied and the simulated slope has been extracted.

Given also the low statistic in the high mass region no structure function appears to give results incompatible with the data. Therefore the underestimation of the data by the fit does not come from a different slope between data and simulation

	Be 2000	Al 99	Cu 99	Ag 2000	W 98
Z	4	13	29	47	74
A	9.01	26.98	63.55	108	183.84
ρ (g/cm^3)	1.85	2.7	8.96	10.5	19.1
λ_i $(g/cm^2$)	75.2	106.4	134.9	156	185
λ_i (cm)	40.65	39.41	15.06	14.86	9.69
L (cm)	13	12	7.5	7.5	4.5
L_{eff} (cm)	11.13	10.35	5.91	5.89	3.6
N. argonium 10^9	1.882E+09	1.185E+09	8.204E+08	8.204E+08	3.283E+08
N. protons 10^{12}	1.206E+13	7.593E+12	5.257E+12	5.257E+12	2.103E+12
$\epsilon_{trigger}$	0.857	0.901	0.901	0.876	0.873
$\epsilon_{reconstruction}$	0.985	0.987	0.968	0.978	0.992
Luminosity $(10^{36}\ cm^{-2}$)	14.0	4.21	2.34	1.54	0.412
Acc_ψ	0.1408	0.1405	0.1401	0.1397	0.1386
N_ψ	95705	84458	104155	104665	45555
σ_ψ (nb)	48.48	142.7	317.4	486.2	798.0
σ_ψ/A (nb)	5.380	5.287	4.994	4.502	4.341
$Acc_{\psi'}$	0.1664	0.1642	0.1637	0.1635	0.1628
$N_{\psi'}$	1860	1686	1959	1948	889
$\sigma_{\psi'}$ (nb)	0.8069	2.437	5.109	7.732	13.26
$\sigma_{\psi'}/A$ (nb)	0.0896	0.0903	0.0804	0.0716	0.0721
Acc_{DY}	0.1379	0.1392	0.1393	0.1397	0.1389
N_{DY}	1880	1865	2156	2576	1155
σ_{DY} (nb)	0.9724	3.179	6.607	11.97	20.20
σ_{DY}/A (nb)	0.1079	0.1178	0.1040	0.1108	0.1099

Table 5.8: The J/ψ , ψ' and DY cross sections from the "standard" fitting method, acceptance corrected, 1% global cut.

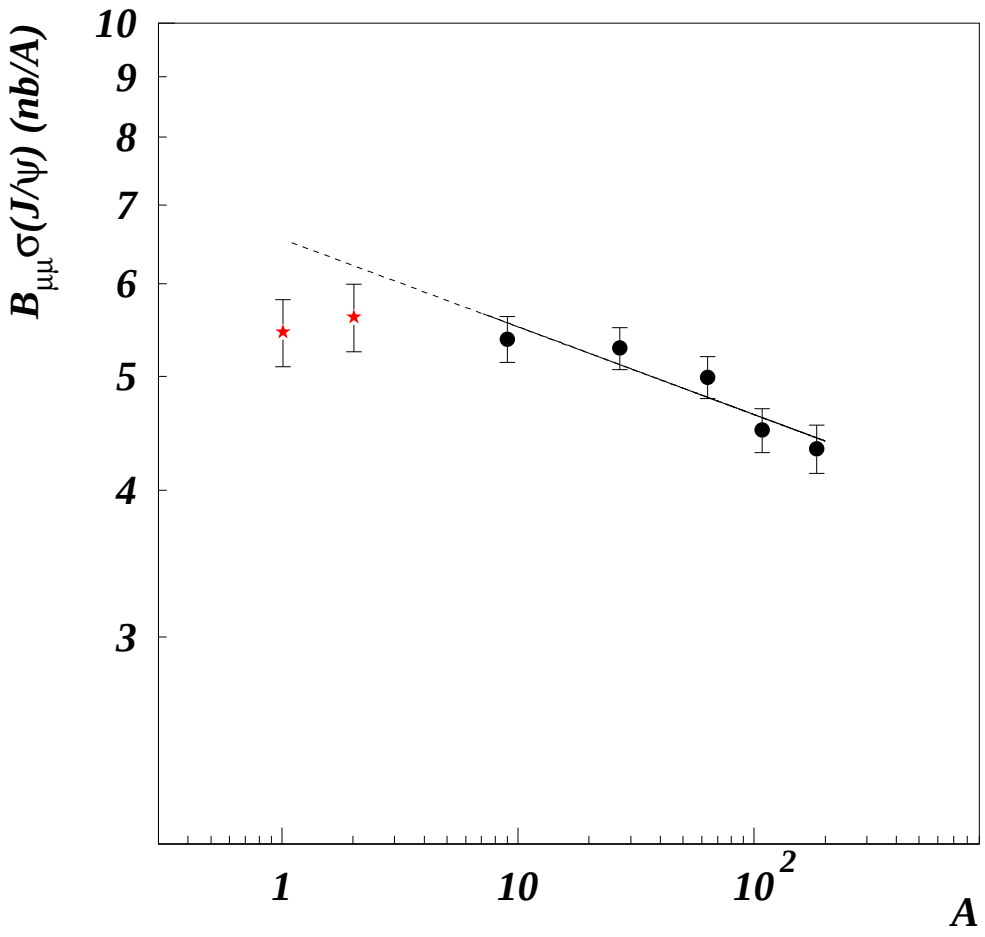

Figure 5.15: The J/ψ cross section from the "standard" fitting method, acceptance corrected, 1% global cut as a function of A (the mass number of the target). The two red stars are for proton-proton and proton-deuterium cross sections measured by the NA51 collaboration at the same beam energy of 450 GeV. The errors on these points include absolute systematic errors on the normalisation. The NA50 points measured in the present work (closed circles) have two error bars: the internal error bars are the statistical errors (smaller than the symbol size), the external error bars represent the global (statistical+systematic) uncertainty. The fit to the NA50 points is shown.

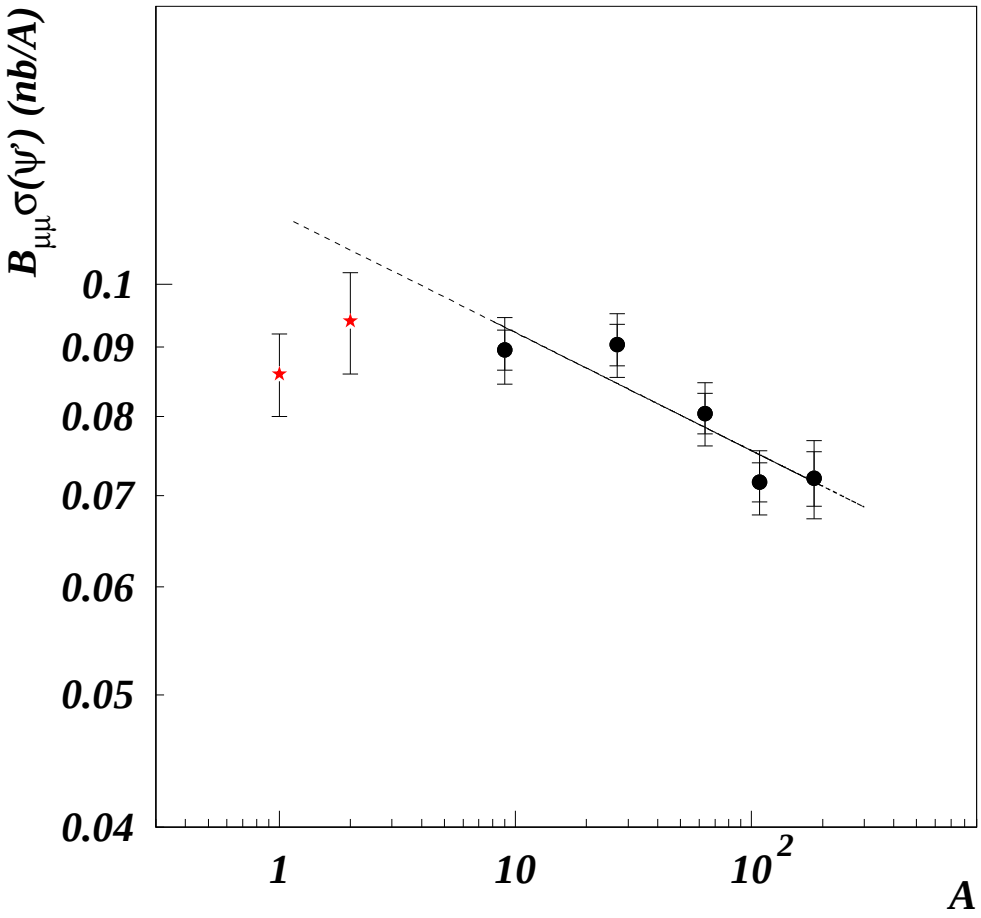

Figure 5.16: ψ' cross section from the "standard" fitting method, acceptance corrected, with 1% global cut, as a function of A (the mass number of the target). The small error bars show statistical uncertainties on ψ' production. The external error bars include both statistical and systematic errors. The fit to NA50 points (filled circles) is shown.

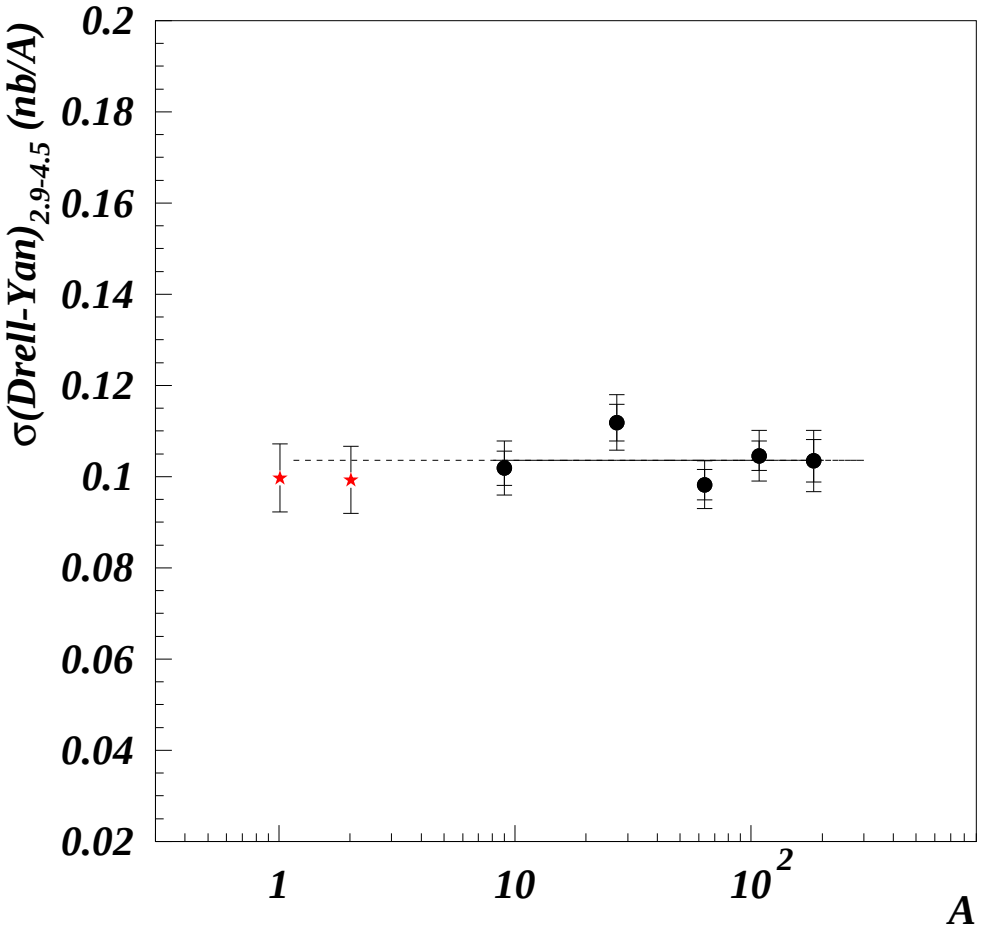

Figure 5.17: DY cross section from the "standard" fitting method, acceptance corrected, with 1% global cut, isospin corrected, as a function of A (the mass number of the target). The two red stars are for proton-proton and proton-deuterium cross sections measured by the NA51 collaboration. The closed circles are from this work. For these points the small error bars include statistical uncertainties on DY production. The external error bars include both statistic and systematic errors. The constant fit to the NA50 points is shown.

GeV^{-1}	Data	MRS (G) 41	MRS (A) 43	GRV (94 HO) 6
p-Be	-0.94 ± 0.06	-0.940 ± 0.025	-0.948 ± 0.020	-0.938 ± 0.021
p-Al	-1.05 ± 0.07	-0.912 ± 0.021	-0.974 ± 0.020	-0.950 ± 0.021
p-Cu	-0.90 ± 0.06	-0.942 ± 0.021	-0.943 ± 0.020	-0.957 ± 0.021
p-Ag	-0.97 ± 0.05	-0.943 ± 0.020	-0.939 ± 0.020	-0.919 ± 0.020
p-W	-1.00 ± 0.07	-0.922 ± 0.021	-0.944 ± 0.020	-0.915 ± 0.021

Table 5.9: Comparison between DY slopes extracted form proton nucleus data and slopes extracted from simulation.

in the high mass region. The MRS (A) 43 has therefore been employed to be coherent with NA50 published results and to allow easier comparisons.

5.10 Nuclear shadowing effects on DY

Calculations about nuclear modifications to Drell-Yan production in p-A and A-A collisions have recently became available. It is known that the free parton distribution functions are modified when the nucleons are bound into a nucleus and this may influence the differential DY cross section.

However a recent calculation [14] shows that the net nuclear corrections remain small in p-A collisions at 450 GeV. An estimation of nuclear shadowing effects is provided in the acceptance region of the NA50 experiment for p-Be and p-W collisions. The ratio of shadowed over non-shadowed Drell-Yan cross section is plotted as a function of the invariant mass of the DY pair. Both LO and NLO calculations are reported.

We have used these results to modify our unshadowed DY mass shapes and have performed again the fit to the mass spectra.

The results of the fit are reported in Table 5.10. The effects of line shape modifications on DY estimation result to be negligible, if compared with the statistical uncertainties. This allows to conclude that, in our phase space region, nuclear shadowing effects on DY production are unimportant.

5.11 DY fit on the high mass region (HMDY)

The "standard" fitting method appears to slightly underestimate the DY production in the high mass region (between 5 and 8 GeV) as it is shown in Table 5.3.

A possible overcome of this systematic effect is to focus on this high mass region in the determination of the DY normalisation. A possible way is to count the number

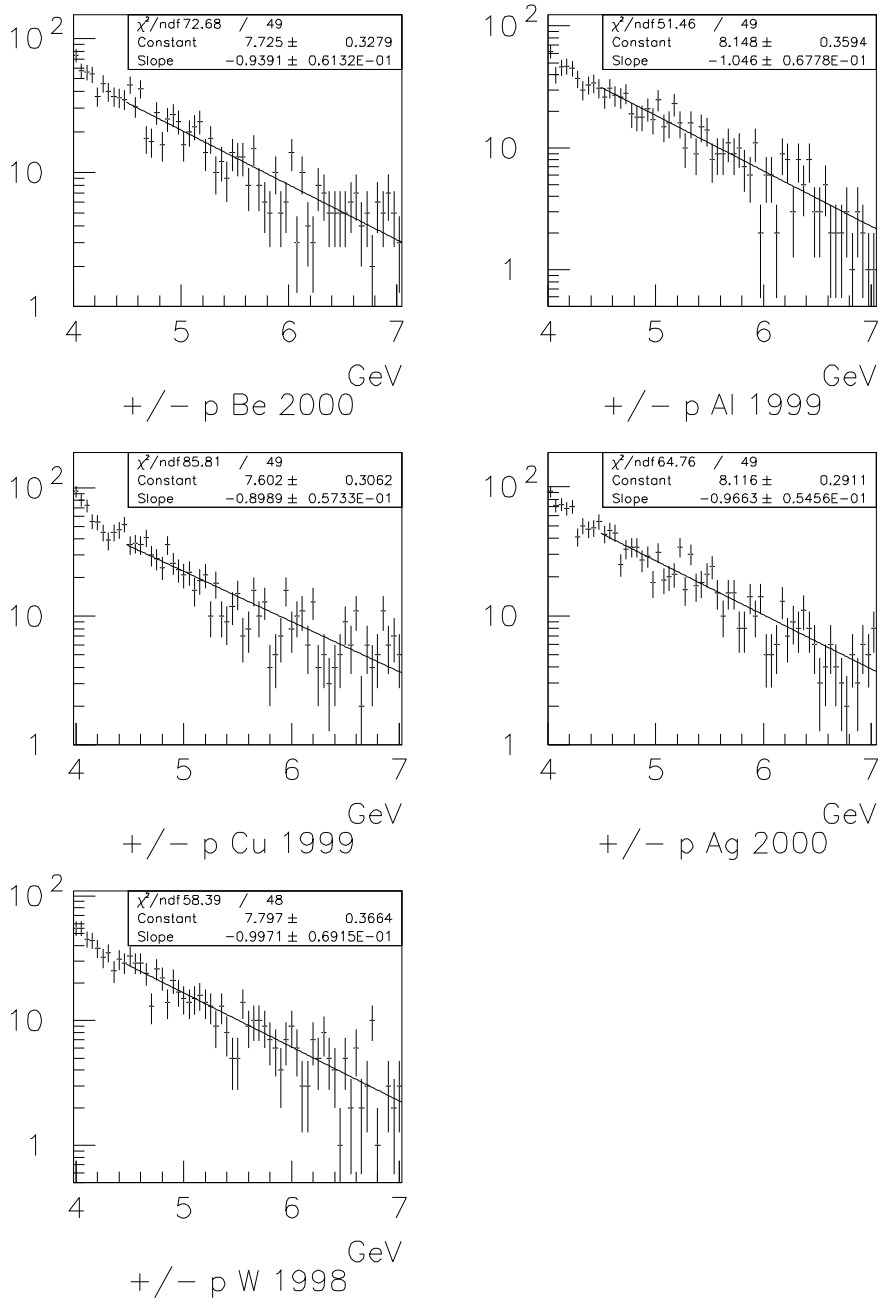

Figure 5.18: Fit with an exponential function to the invariant mass spectra in the high mass region for the various proton-nucleus collisions.

	p Be		p W	
	N. DY	χ^2	N. DY	χ^2
no shadowing	2445± 80	1.30	1950± 70	1.05
shadowing from [14]	2448± 80	1.30	1952± 70	1.05

Table 5.10: Effect of the shadowing corrections to DY line shapes on the estimation of DY production. The number of fitted DY pairs between 2.9 and 4.5 GeV/c^2 is reported for the "standard" fitting procedure. The results already given in table 5.3 are reported for comparison.

of entries between 5 and 8 GeV and to use them to fix the DY normalisation. The fit to the global spectrum is then performed.

In Figure 5.19 and Figure 5.20 two fits using the "standard" fitting method modified by this criterion (HMDY) are presented. The results are given in Table 5.11.

The error on DY normalisation is estimated by the uncertainty on the number of events in the region between 5 and 8 GeV. The small statistics in the region used to fix the DY normalisation reflects in a larger uncertainty on DY for this method.

In Figure 5.21 the DY cross sections per nucleon are plotted versus the mass number of the target.

The nuclear dependence is extracted and is given in the following table together with the test on the $\alpha = 1$ hypothesis. As will be shown later the low statistics on DY make this method much less precise than the "standard" fitting method for the estimation of the ψ/DY ratio.

points used in the fit		σ (pb)	χ^2	
NA50 with stat. errors only	$\alpha_{DY} = 0.975 \pm 0.021$		2.8	
NA50 with stat. errors only	$\alpha_{DY} = 1$	107.8 ± 2.4	2.4	hyp.
NA50	$\alpha_{DY} = 0.973 \pm 0.029$		1.6	
NA50	$\alpha_{DY} = 1$	107.8 ± 3.2	1.5	hyp.

5.12 Other fitting approaches

The number of possible fitting approaches is of course very large. In this section we concentrate on alternative descriptions of the intermediate mass region.

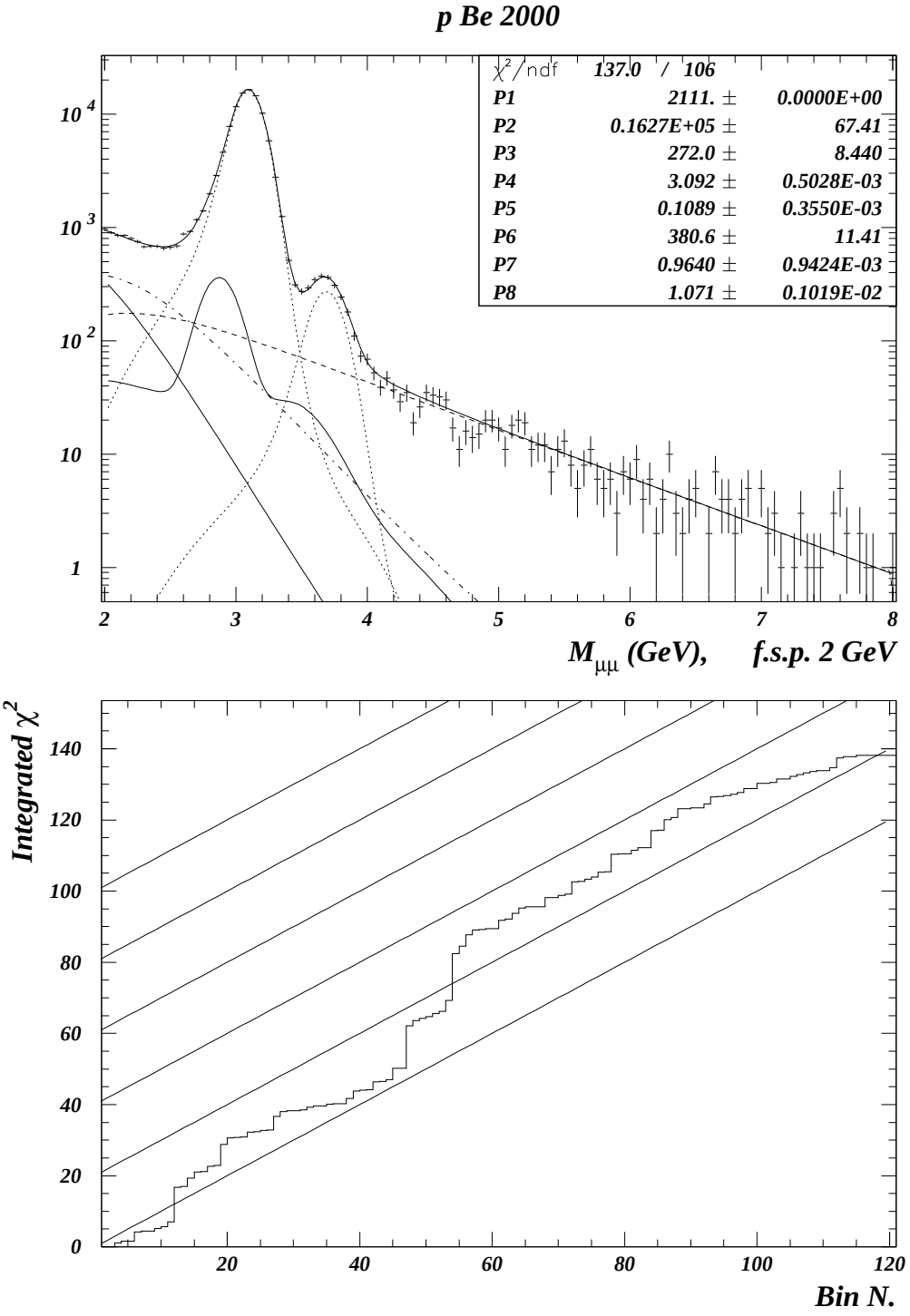

Figure 5.19: Fit on the p Be 2000 data sample, 1% global cut, DY shape calculated with MRS43, "standard" fitting method and "HMDY" criterion. The upper continuous line is the sum of all the signal contributions: J/ψ and ψ' resonances (dotted lines), the DY continuum (dashed line), the open charm continuum (dashed-dotted line), the background and empty target contributions (continuous lines). The fitted values of the parameters are shown. The starting point of the fit (f.s.p.) is indicated. A plot of the integrated χ^2 over the range of

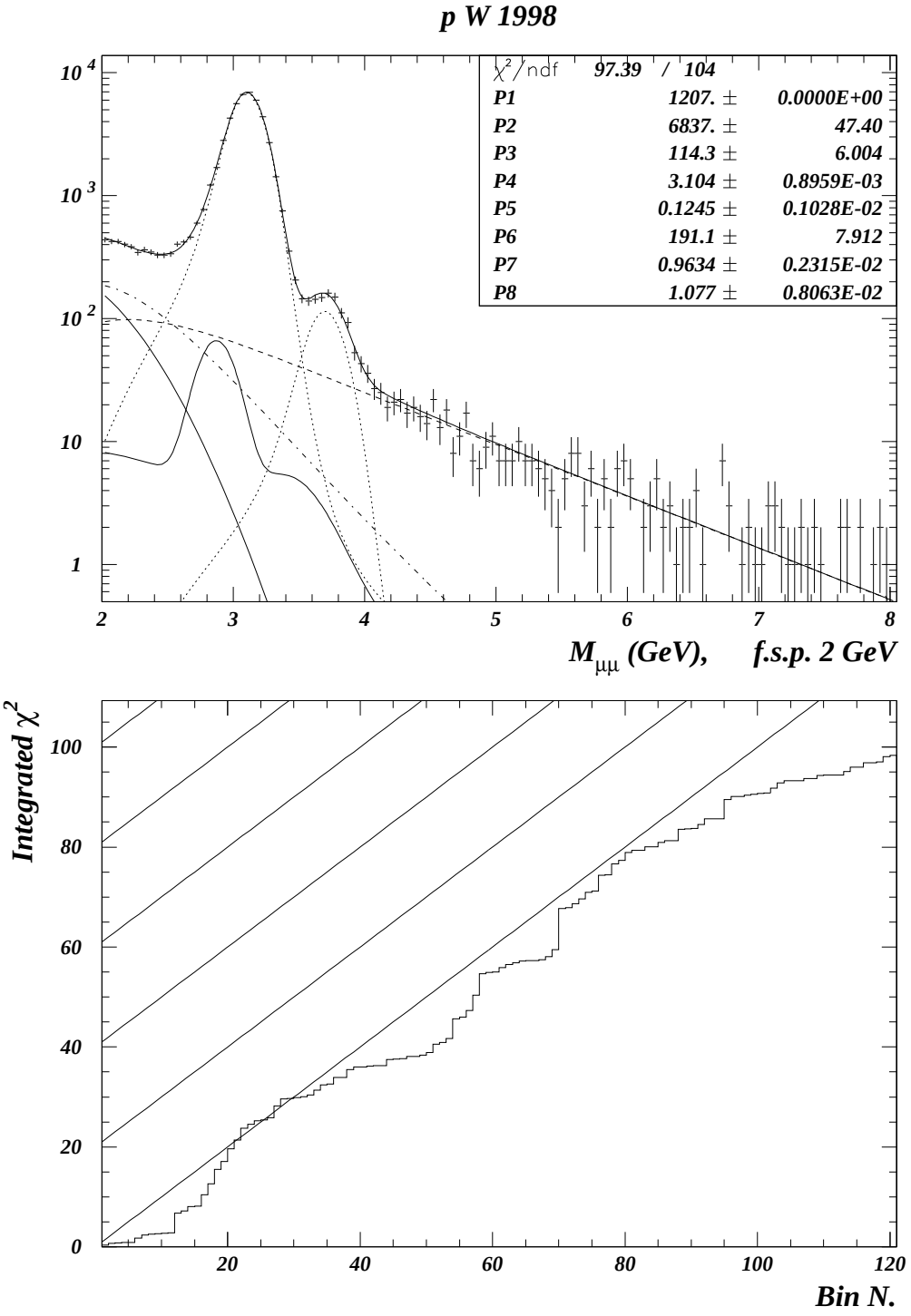

Figure 5.20: Fit on the p W 1998 data sample, 1% global cut, DY shape calculated with MRS43, "standard" fitting method and "HMDY" criterion. See Figure 5.19 for description of the curves.

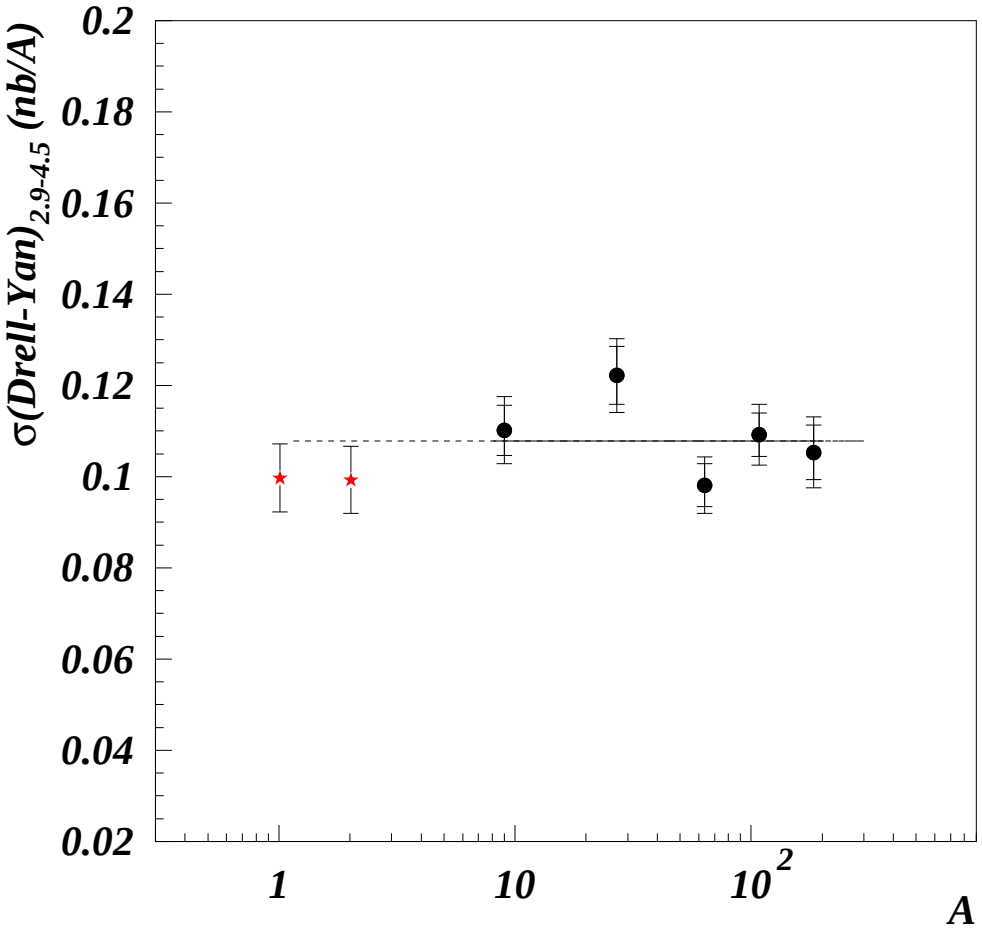

Figure 5.21: DY cross section from the "standard" fitting method and "HMDY" criterion, acceptance corrected, with 1% global cut , isospin corrected, as a function of A (the mass number of the target). The two red stars are for proton-proton and proton-deuterium cross sections measured by the NA51 collaboration. The closed circles are from this work. For these points the small error bars include statistical uncertainties on DY production. The external error bars include both statistic and systematic errors.

	p Be 00	p Al 99	p Cu 99	p Ag 00	p W 98
J/ψ	95596 ± 400	84335 ± 410	103135 ± 450	103542 ± 400	45626 ± 320
ψ'	1823± 60	1644± 60	1936± 65	1864± 60	820± 45
DY	2034± 100	2037± 110	2154± 100	2690± 115	1176± 70
ψ /DY	45.7± 2.3	41.4± 2.2	47.0± 2.3	38.4± 1.7	39.2± 2.2
ψ'/ψ	0.0164 ± 0.0005	0.0169 ± 0.0006	0.0162 ± 0.0005	0.0155 ± 0.0005	0.0154 ± 0.0008
R	1.12	1.13	1.10	1.09	1.14
$D\overline{D}$ /DY	3.44± 0.35	3.21± 0.35	3.77± 0.30	2.82± 0.27	2.8± 0.35
χ^2	1.29	1.35	1.37	1.10	0.94
DYHM	309	319	341	432	185

Table 5.11: Results for the "standard" fitting method with run selection with "HMDY" criterion. The number of J/ψ , ψ' , DY pairs from 2.9 GeV to 4.5 GeV are reported. The ratio ψ /DY and ψ'/ψ corrected for acceptances are reported. The fixed R factor used for the combinatorial background normalisation is reported. The ratio $D\overline{D}$ /DY, the χ^2 of the fits, the number of entries between 5 and 8 GeV are reported.

- A first approach is to try to fix a constant $D\overline{D}/$ DY ratio for all the nuclei, as one expects for hard scattering processes. This condition has been imposed using two criteria:

  1. the mean value of the measured $D\overline{D}/$ DY value extracted from the various fits has been used for all the nuclei
  2. a simultaneous fit has been performed on the five spectra in order to extract the global $D\overline{D}/$ DY.

Both these approaches give an unsatisfactory description of the intermediate mass region. We know that problems in this region can reflect on the DY description in the high mass region.

- In order to have a better description of the intermediate mass region one can tentatively let the R value for the background normalisation as a free parameter in the fit in the intermediate mass region. This can be done:

  1. fixing $D\overline{D}$ /DY to its average value from the fits to the various p-A systems,
  2. using the $D\overline{D}$ /DY from the simultaneous fit of the five spectra.

When R is left free, its final values from the fit become meaningless (< 1).

As a general remark, all these fitting criteria have shown problems in their reliability. This is mainly because there are many different sources in the intermediate mass region and our knowledge of line shapes is worse than in the high mass region.

Nevertheless, we discuss for completeness two of these approaches.

5.12.1 $D\overline{D}$ /DY fixed from a global fit on the five spectra

The NA50 collaboration has published the value $D\overline{D}/DY = 4.2\pm$ 0.9 for p-A at 450 GeV [13]. This value had been extracted from high intensity proton nucleus data taken before 1998 not used in this thesis. Following a similar procedure a $D\overline{D}$ /DY value has been extracted for the data analysed here.

A simultaneous fit on the five spectra has been performed. The fit has 35 free parameters corresponding to the DY normalisations, J/ψ normalisations, ψ' normalisations , the five pole position for the ψ , the five widths of the ψ and the ten parameters describing the ψ tails. The $D\overline{D}$ normalisation is governed by the 36^{th} free parameter and is common for the five data sets. From the simultaneous fit the resulting $D\overline{D}$ /DY is $4.27\pm$ 0.13.

The result is in good agreement with the published result but is somehow in contradiction with the results of the "standard" fitting method reported in Table 5.3 especially for p-W.

However, it must be noted that the low statistic data samples, as p-W, are unfavoured by this procedure. In fact each data set has an equal contribution to the global χ^2 and this results in a worse description of the low statistics data samples.

We have used the resulting $D\overline{D}$ /DY to fit separately each target. The results on the description of the high mass region are rather poor, as can be seen in the following table where the ratio of the number of entries between 5 and 8 GeV over estimated from the fit is given for the five targets.

	p Be	p Al	p Cu	p Ag	p W
DYHM e/c	1.12	1.10	1.07	1.19	1.17

The disagreement at high mass is essentially due to the fact that, in order to constrain the intermediate mass region, the fit uses the DY lever at the expense of the description of the high mass region.

5.12.2 $D\overline{D}$ /DY fixed at 4.27± 0.13 and R free

When the $D\overline{D}$ /DY is fixed at 4.27± 0.13, the R factor for the scaling of the background contribution can be left free, to ameliorate the description of the IMR.

The limit of the R factor for a low intensity proton beam has been measured by the NA38 collaboration and is ≈ 1.22. The high intensity limit when different events overlap in the same trigger gate is 1.

The resulting R factor for this fitting procedure is given in the following table. The DY has more freedom to adjust itself to the high mass region of the spectra and the ratios DYHM e/c are closer to 1, but the R factor resulting from the fit is outside the physical limits, i.e. smaller than 1.

	p Be	p Al	p Cu	p Ag	p W
DYHM e/c	1.11	1.06	1.08	1.12	1.09
R	0.99± 0.07	0.92± 0.08	1.03± 0.05	0.86± 0.04	0.87± 0.09

5.13 The ψ/DY ratio

When ratios of cross sections are considered, most of the systematic errors cancel. All the uncertainties connected with the normalisation (absolute calibrations, efficiencies) are cancelled by the ratio. The errors on the acceptance calculation are not cancelled but are reduced since ratios of acceptances are rather considered. Problems with inefficiencies localised in some part of the spectrometer and in some particular run, affect essentially all the mass spectrum in a similar way.

The comparison of resonance cross sections with DY process is useful because DY production is proportional to the number of nucleon-nucleon collisions. Therefore the ratio ψ/DY is proportional to the cross section per nucleon-nucleon collision exactly as $\sigma_{J/\psi}/A$. Unfortunately using the ratio ψ/DY we introduce larger statistical errors because of the small DY cross section.

In Figure 5.22 we plot the ratio

$$\frac{B_{\mu\mu}\,\sigma_{J/\psi}}{\int_{2.9}^{4.5}\frac{d\sigma_{DY}}{dM}\,dM}$$

where $B_{\mu\mu}$ is the branching ratio of the J/ψ into two muons and $\frac{d\sigma_{DY}}{dM}$ is the cross section for the DY process, integrated over the mass range 2.9-4.5 GeV.

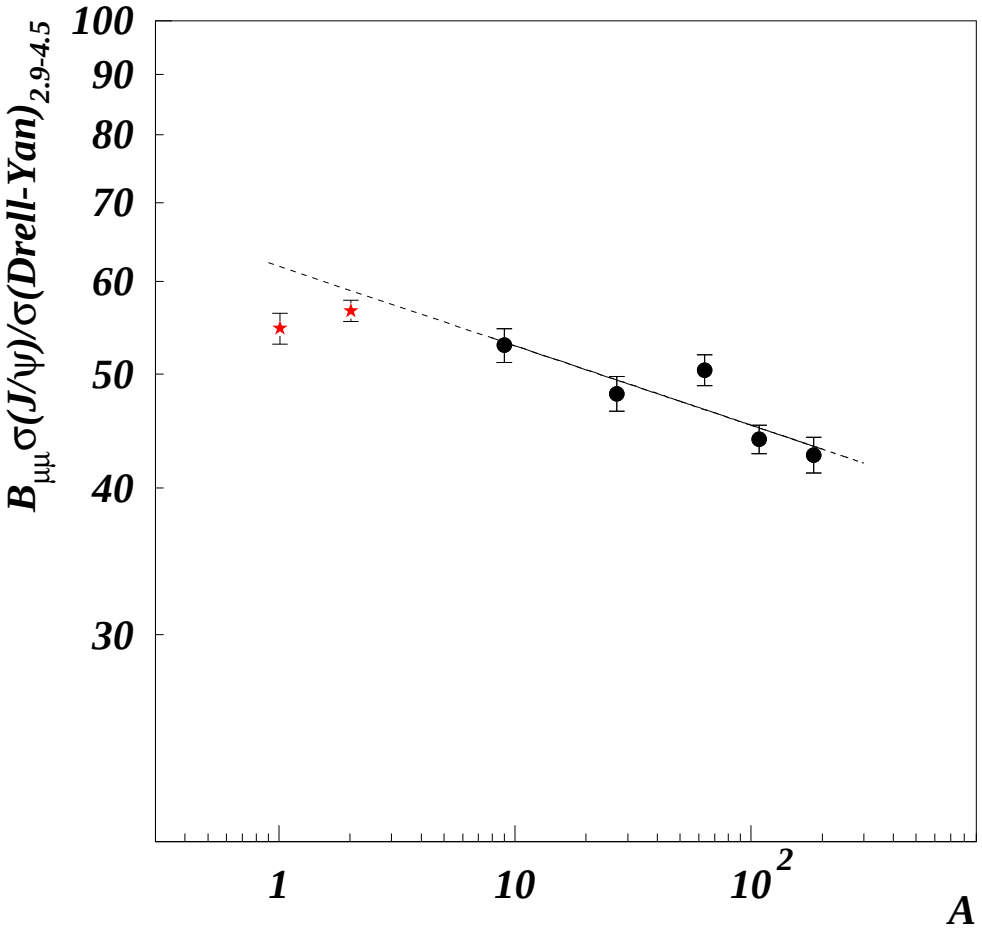

Figure 5.22: The ψ /DY ratio obtained with the "standard" fitting method (filled circles). A fit to these points to extract the α dependence is shown. The points published by NA51 (p-p and p-d) are shown but not included in the fit.

The nuclear dependence is extracted with a fit to the five NA50 points studied in this work. The NA51 points are plotted but not included in the fit.

The extracted α_ψ is 0.932± 0.014, with $\chi^2 = 2.5$. This is in good agreement with the α_ψ values extracted from the J/ψ cross sections. If the p-Cu point is excluded from the fit the results does not significantly change: α_ψ =0.929± 0.014 with $\chi^2 = 0.08$.

Again there is a certain disagreement between the p-p and p-d points with the p-A data. This can be due to the fact that the A^α parametrisation is inaccurate at low A .

In Figure 5.23 a fit to the points extracted using the HMDY approach is shown. The resulting α_ψ is 0.949± 0.021, with $\chi^2 = 2.0$ from the fit to the five points (α_ψ =0.943± 0.022 with $\chi^2 = 0.94$ when the p-Cu point is excluded). This result is compatible with the previous one but the statistical errors are much larger. It should be noted that the values are systematically lower with respect to the "standard method" results. This was expected, since with the standard method the fit slightly underestimates the high mass Drell-Yan. The errors connected with this procedure are large because of the lack of statistics in the high mass DY region.

In Figure 5.24 the standard fitting method is compared for the whole of the statistics and for the selected stable runs used in the cross section calculations. These runs take the information of the 76% of the collisions for p-Be, 84% for p-Al, 79% for p-Cu and p-Ag, 56% for p-W. The single points are in good agreement with each other and the fitted α_ψ is 0.929± 0.016, with $\chi^2 = 3.2$ in excellent agreement with the fit on full statistics. This verifies the hypothesis that problems in the efficiency of the spectrometer affect in the same way all the invariant mass spectrum and are cancelled in the ratios.

5.13.1 Target-out rejection

As it was explained in Section 3.3.5 the global cuts are extremely useful in reducing the target-out contamination in the data sample. In principle using target out runs one can easily subtract the contribution of interactions not taking place in the target. However, if the running conditions are not very stable, it might happen that the empty target runs are taken in different conditions with respect to part of the target-in runs. This could induce a small bias in the empty target subtraction.

To limit this effect we have raised the global cut level at 20%, to reduce as much as possible the target-out contamination in our data sample.

About 35% of the statistics is rejected by this strong cut (with respect to 1% global cut). The effect on the target-out data sample is much greater. More

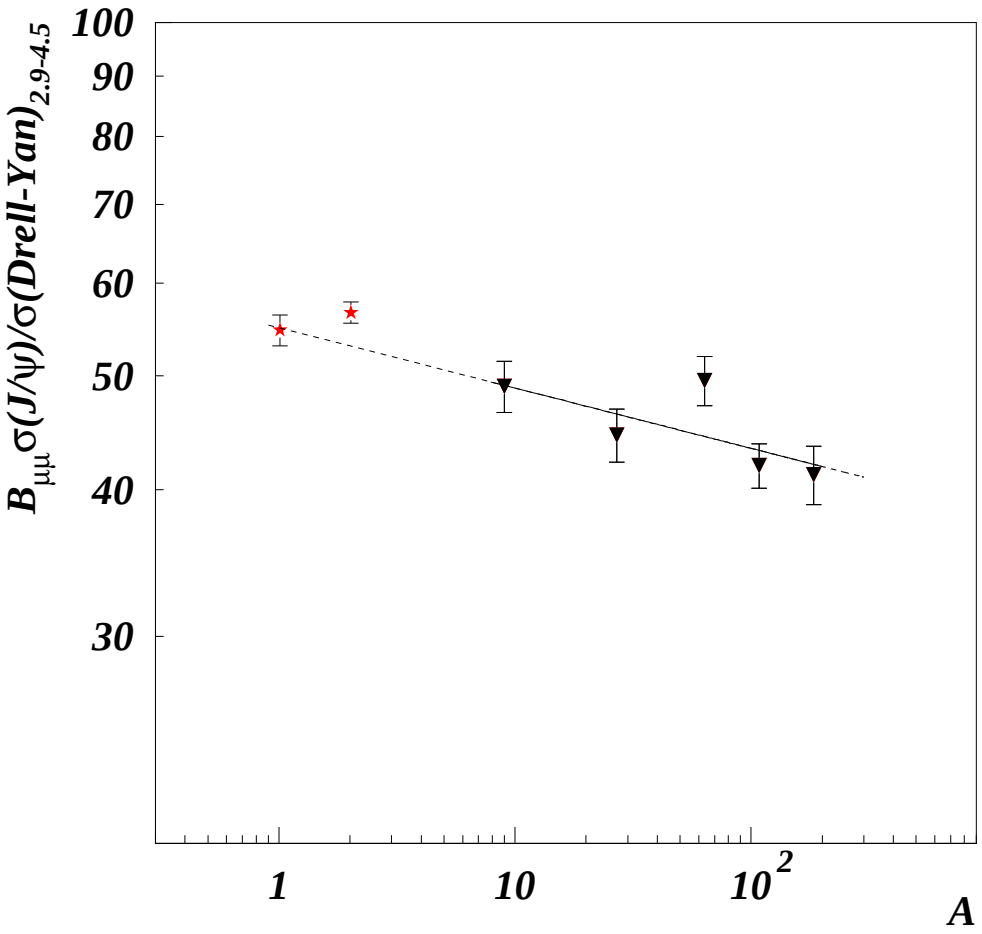

Figure 5.23: The ψ /DY ratio obtained with the "standard" fitting method and "HMDY" approach (filled triangles). A fit to these points to extract the α dependence is shown. The points published by NA51 (p-p and p-d) are shown but not included in the fit.

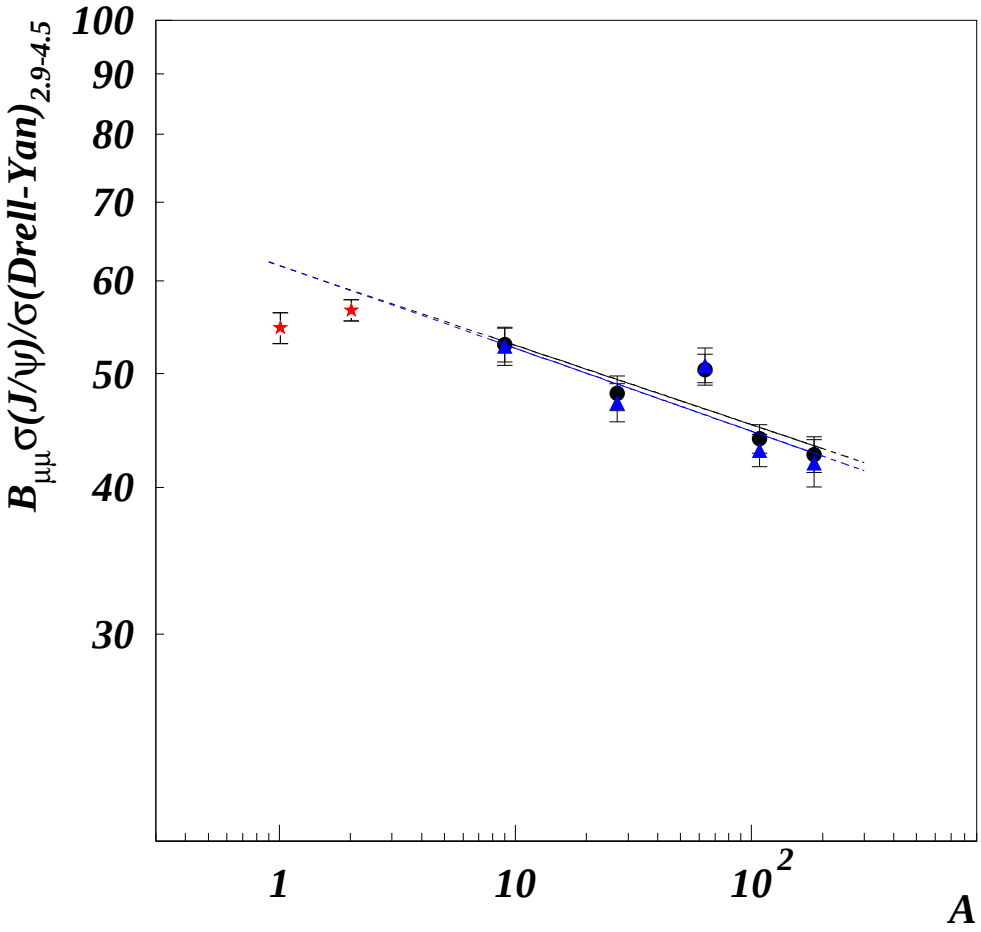

Figure 5.24: The ψ /DY ratio obtained with the "standard" fitting method (filled circles) on the whole statistics is compared with points extracted from the selected runs. A fit to these points to extract the α dependence is shown (dotted line for the full statistics and dashed line for the selected data sample). The points published by NA51 (p-p and p-d) are shown but not included in the fit.

than 54% of the remaining out-of target events should be rejected by this cut. Therefore this method provides an effective way to significantly reduce the out-of target contamination.

In Figure 5.25 the points extracted with the standard method (1% global cut) are compared with the 20% global cut results. There is excellent agreement between the points for each target and also for the fitted α value: 0.927± 0.017 with a $\chi^2 = 1.4$, to be compared with 0.932± 0.014, with $\chi^2 = 2.5$.

5.14 The $B_{\mu\mu}\sigma_{\psi'}/\sigma_{DY}$ ratio

The ratio ψ'/DY , with the DY cross section integrated between 2.9 and 4.5 GeV, is shown in Figure 5.26. The errors are much larger than on ψ /DY ratio for for two reasons. The first reason is that both event classes have low statistics, the second reason comes from the negative correlation between the DY normalisation and the ψ' normalisation. The consequence is that an overestimation of the number of ψ' causes a slight underestimation of the DY normalisation, or vice versa and underestimation of the ψ' normalisation makes the DY be overestimated. This effect is amplified in the ratio.

The nuclear dependence of ψ' production is: $\alpha_{\psi'} = 0.905 \pm 0.020$ with $\chi^2 = 1.7$ when all the points are included and $\alpha_{\psi'} = 0.899 \pm 0.021$ with $\chi^2 = 0.26$ when the p-Cu point is excluded from the fit. Both these results are compatible with the $\alpha_{\psi'}$ extracted from the ψ' cross section.

The pattern of the points resembles the ψ /DY especially for the p-Cu point being out of the general trend. This reinforces the hypothesis that a statistical fluctuation occurred in the high mass DY during the p-Cu 1999 data taking.

5.15 The ψ'/ψ ratio

The ratio of ψ' and J/ψ measured cross sections has also been studied. The choice of the fitting procedure can particularly affect this ratio, mainly because of the small number of ψ' in the data sample and because of the strong influences of the J/ψ tail parameters on the ψ' normalisation. This was in fact one of the major reasons to introduce (see Section 5.2.2) a second independent smearing method.

In Figure 5.27 the results for the "standard" fitting procedure and the "uniform smearing" fitting method are shown.

The results are summarised in the following table. The result of the approach that focuses on the high mass DY is also quoted.

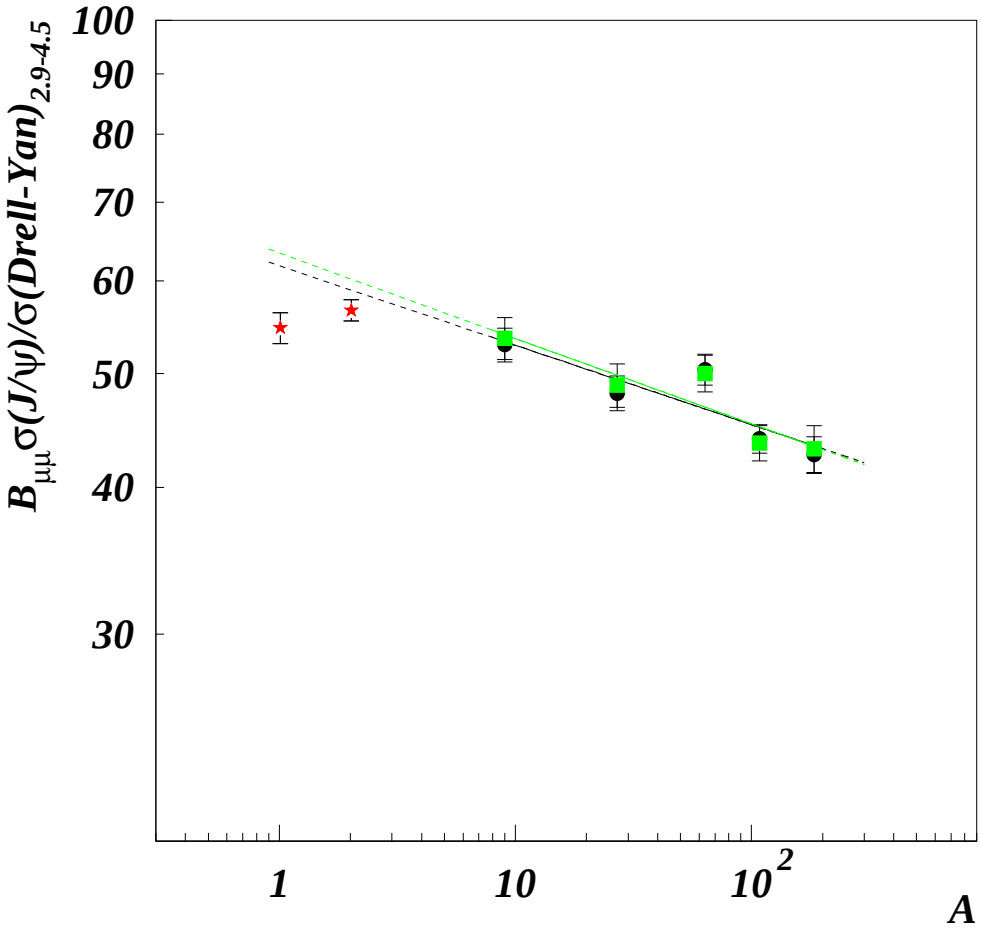

Figure 5.25: The ψ /DY ratio obtained with the "standard" fitting method and 1% global cut (filled circles) is compared with points with 20% global cut. A fit to these points to extract the α dependence is shown (dashed line for 1% global cut and dotted line for 20% global cut). The points published by NA51 (p-p and p-d) are shown but not included in the fit.

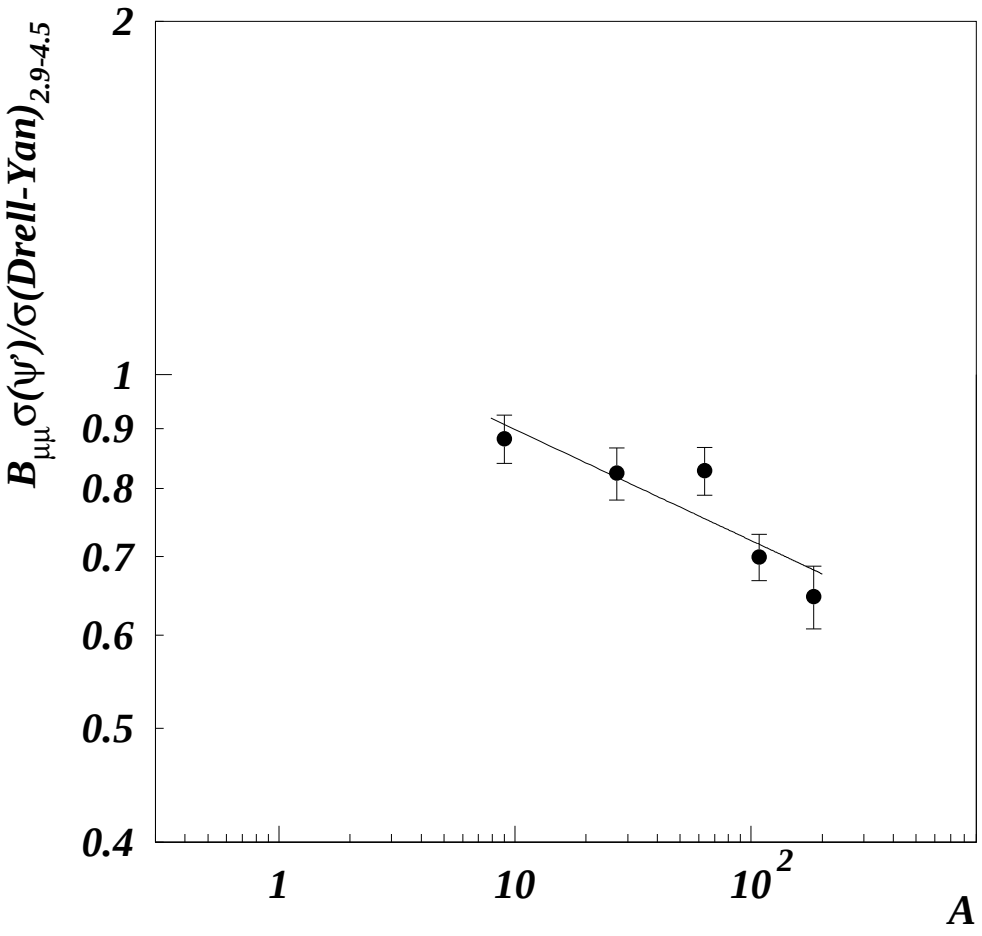

Figure 5.26: The ψ'/DY ratio for "standard" fitting method.

method	$\alpha_\psi - \alpha_{\psi'}$	ψ'/ψ	χ^2	
standard	$\Delta\alpha = -0.028 \pm 0.014$		0.88	
	$\Delta\alpha = 0$	0.0163 ± 0.0002	1.7	hypothesis
uniform	$\Delta\alpha = -0.033 \pm 0.013$		1.4	
	$\Delta\alpha = 0$	0.0161 ± 0.0002	2.7	hypothesis
HMDY	$\Delta\alpha = -0.025 \pm 0.013$		1.0	
	$\Delta\alpha = 0$	0.0161 ± 0.0002	1.7	hypothesis

The three methods are in good agreement with each other for the nuclear dependence. The ψ' has a stronger suppression than the J/ψ . The hypothesis of a constant ψ'/ψ gives a worse χ^2 in all cases. Different fitting methods tend to give systematically different results on the average ψ'/ψ (within 3%) but the size of nuclear effects estimated through α remains very stable.

5.16 The nuclear dependence of direct J/ψ

The observed discrepancy between the nuclear dependence of the ψ' and of the J/ψ imposes some caution in the interpretation of J/ψ results. The problem arises from the fact that, if the different $c\bar{c}$ states have different nuclear dependencies, the contribution of ψ' and χ_c decaying into J/ψ must be taken into account.

$\alpha_{\psi'}$ is directly measured, so that the $\approx 8\%$ contribution to the J/ψ signal coming from the ψ' can be easily subtracted. Unfortunately for the χ_c no measurements are available.

The χ_c has a lower binding energy than the J/ψ and an higher binding energy with respect to the ψ' . If what interacts with the nucleus is the fully formed resonance, one could expect that α_{χ_c} is related to $\alpha_{J/\psi}$ and $\alpha_{\psi'}$ by the relation:

$$\alpha_{\psi'} \leq \alpha_{\chi_c} \leq \alpha_{J/\psi} \tag{5.5}$$

Since the contribution to J/ψ signal coming from the χ_c is $\approx 40\%$, the indetermination of Eq. 5.5 introduces an uncertainty on the intrinsic α of native J/ψ states.

In the following table we give the results of a fit to the ψ/DY results with the standard fitting method with correction for ψ' and χ_c feed to J/ψ signal. Two different assumptions for the α_{χ_c} are made and in the last line the result given in Section 5.13 is reported for comparison.

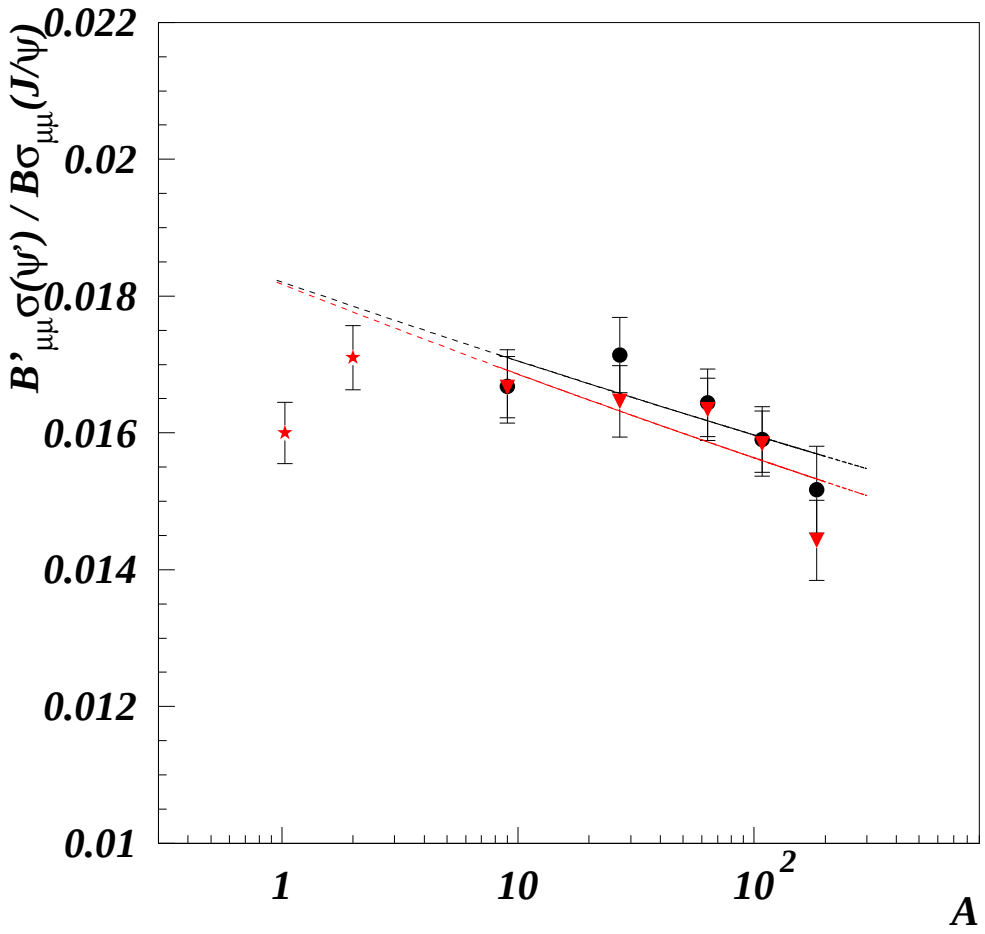

Figure 5.27: The ψ'/ψ ratio extracted using the standard fitting method (filled circles) and the uniform smearing fitting method (filled triangles). For the two data sets a power law fit is shown. The NA51 measurements (filled stars) are not included in the fits.

assumption	α of native J/ψ
$\alpha_{\chi_c} = \alpha_{\psi'}$	0.953 ± 0.022
$\alpha_{\chi_c} = \alpha_{\psi}$	0.934 ± 0.015
no correction	0.932 ± 0.014

It would be therefore very interesting to have a direct measurement of χ_c nuclear absorption. This is currently planned by the NA60 collaboration. The A-dependence of χ_c production in p-A collisions will be studied with an upgraded NA50 spectrometer [15].

Chapter 6

Comparison with nucleus-nucleus data

The main purpose of NA50 and NA38 experiments is the study of J/ψ production in ion-ion collisions. Many different systems have been studied: O-Cu, O-U, S-U at 200· A GeV/c (NA38) and finally Pb-Pb at 158· A GeV/c (NA50). With a similar apparatus the NA51 collaboration studied also p-p and p-d interactions at 450 GeV/c .

In Pb-Pb collisions an anomalous J/ψ suppression has been observed. For the most peripheral collisions the J/ψ shows an absorption pattern that can be explained in terms of interactions with ordinary nuclear matter. However, increasing the centrality of the collision, the J/ψ suppression shows a sudden increase, with a two step behaviour that can only be explained in the framework of a deconfinement scenario.

The study of J/ψ production described in this thesis aims at providing the necessary reference for "normal" J/ψ absorption.

Therefore I will compare here the results of Chapter 5 with the existing NA38-NA50-NA51 results.

E_{beam}	y range	mass range (GeV/c^2)	System	L.O. calc.
450	$-0.4 < y^* < 0.6$	$2.9 < M_{\mu\mu} < 4.5$	σ_{pp}	55.5 pb
450	$-0.4 < y^* < 0.6$	$2.9 < M_{\mu\mu} < 4.5$	σ_{pD}	117.0 pb
450	$-0.4 < y^* < 0.6$	$2.9 < M_{\mu\mu} < 4.5$	σ_{pBe}/A_{Be}	58.8 pb
450	$-0.4 < y^* < 0.6$	$2.9 < M_{\mu\mu} < 4.5$	σ_{pAl}/A_{Al}	58.5 pb
450	$-0.4 < y^* < 0.6$	$2.9 < M_{\mu\mu} < 4.5$	σ_{pCu}/A_{Cu}	58.7 pb
450	$-0.4 < y^* < 0.6$	$2.9 < M_{\mu\mu} < 4.5$	σ_{pAg}/A_{Ag}	58.8 pb
450	$-0.4 < y^* < 0.6$	$2.9 < M_{\mu\mu} < 4.5$	σ_{pW}/A_{W}	59.0 pb
200	$3 < y_{lab} < 4$	$1.5 < M_{\mu\mu} < 5.5$	σ_{SU}	2300 nb
158	$0 < y^* < 1$	$2.9 < M_{\mu\mu} < 8.0$	σ_{PbPb}	835 nb

Table 6.1: Calculated Drell-Yan cross section for different systems and rapidity intervals, using the MRS43 structure function

6.1 The DY cross section

The DY process has been used as a reference in all ion-ion studies by the NA50 collaboration. The study of J/ψ cross section with respect to DY production allows to cancel out most uncertainties on luminosity measurements and efficiency calculation.

It has already been shown that in proton-nucleus collisions, the DY is a good reference for J/ψ production since $\alpha = 1$. We want to see if this is true when including nucleus-nucleus results.

The DY cross sections we want to compare have been measured in different kinematic domains and beam energies. An easy way to compare these different measurements is to divide the measured DY cross section by the theoretical calculation and extract the so called K_{DY} factor

$$K_{DY} = \frac{\sigma_{DY\ measured}}{\sigma_{DY\ LO}} \tag{6.1}$$

where the measured DY cross section in a given kinematical window is compared with the Leading Order calculation. The structure function MRS43 is used for the calculation. The calculated DY cross sections at L.O. are shown in Table 6.1.

In Figure 6.1 the p-A points of the present analysis are presented together with other p-A and nucleus-nucleus published points [16], [17], [18]. The whole systematics from p-p to Pb-Pb indicates that K_{DY} is compatible with a constant. Since in the calculation DY is assumed to scale as $(AB)^\alpha$ with $\alpha = 1$ this means that indeed measured DY cross section scales with the number of nucleon-nucleon collisions.

This allow to conclude that even in nucleus-nucleus, as expected, DY is a good reference mechanism for the study of J/ψ suppression.

The extracted K_{DY} is 1.80 ± 0.04 with $\chi^2 = 1.1$.

6.2 The J/ψ cross section

For what concerns the J/ψ cross section, the energy dependence is theoretically known with much less accuracy if compared to DY. This information is however important since nucleus-nucleus J/ψ data (NA38) have been taken at a lower energy. To be able to compare the J/ψ cross section values obtained at different energies we have used an experimental approach, based on the availability of low statistics J/ψ measurements performed at 200 GeV/c [20].

To determine the rescaling factor for 450 GeV/c points we have simultaneously fitted the two sets of data with a common nuclear dependence and a scaling factor. In Figure 6.2 the NA50 points are shown together with NA51 and NA38 points. The estimated 7% systematic error on NA50 points is taken into account. The NA51 p-p and p-d points are not used in the fits (see comment on the influence of p-p points on α determination in Section 1.4).

The scaling factor extracted from the simultaneous fit is 0.325± 0.031. This value is compatible with the less accurate value 0.418 ± 0.083 [19] which would be obtained from the x_F and $\sqrt{s}$ dependence of the J/ψ cross section as given by the Schuler parametrisation [7] (see Section 1.3).

The two sets of points have a compatible nuclear dependence: $\alpha_{450} = 0.925\pm$ 0.018, $\alpha_{200} = 0.88\pm$ 0.24, $\alpha_{450+200} = 0.925\pm0.018$. Of course the 450 GeV/c points dominate because of the much smaller uncertainties.

When rescaling the 450 GeV/c results to 200 GeV/c the large uncertainty on the scaling factor should be included into the error estimation as done if Figure 6.3.

However, this approach is unsatisfactory because it deprives the 450 GeV/c results of all their weight. Moreover the present estimation of the rescaling factor is different from a previous one made by NA50 in [19]: 0.406 ± 0.038 . This estimation, was based on previous NA38 results on J/ψ cross section at 450 GeV. This may indicate the presence of a large systematic error on the rescaling factor that could bias the conclusions. Therefore this approach is not conclusive for what regards the comparison between p-A and S-U results.

A different comparison, more respectful of the uncertainties of each set of results, and independent on the estimations of the rescaling factors, is investigated in Section 6.5.

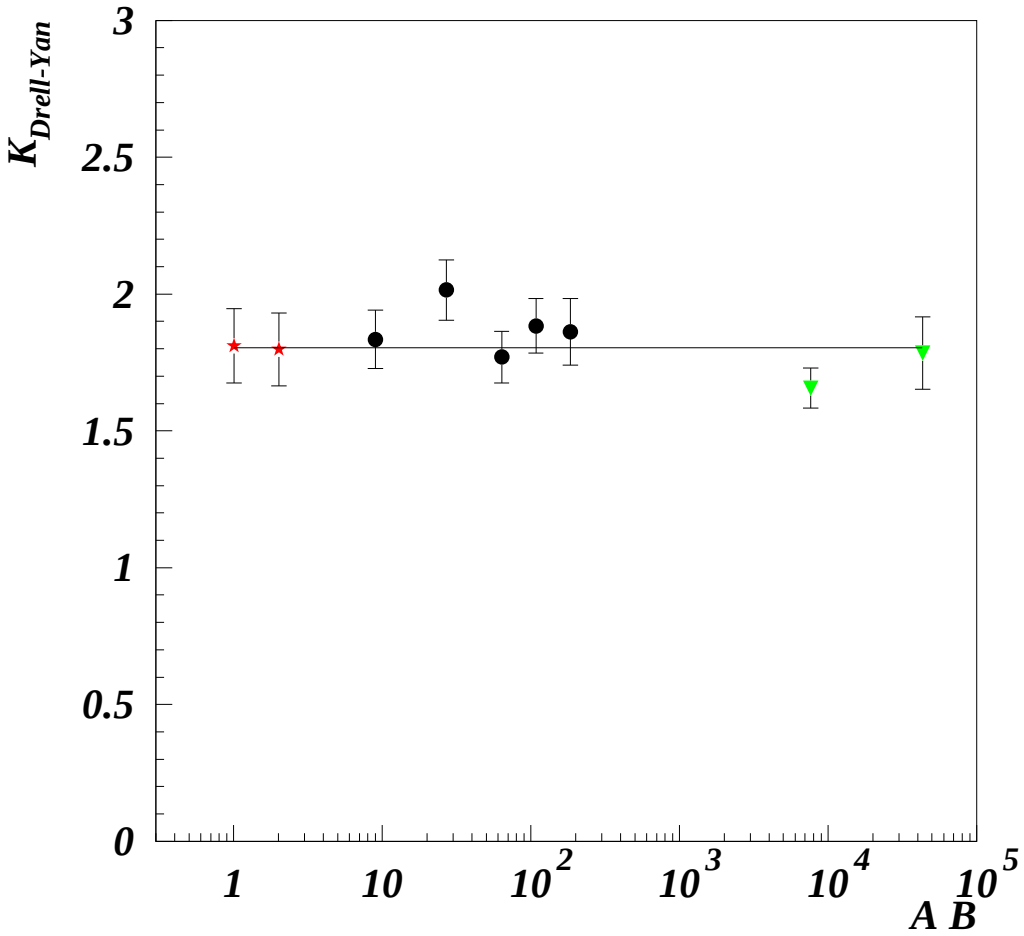

Figure 6.1: The K_{DY} from a Leading Order calculation with MRS43 structure function, versus the product of the projectile and target mass numbers. The p-p and p-d (stars), p-A 450 GeV (filled circles), S-U 200 GeV and Pb-Pb 158 GeV (filled triangles) points are shown. The fit to the all the points is shown.

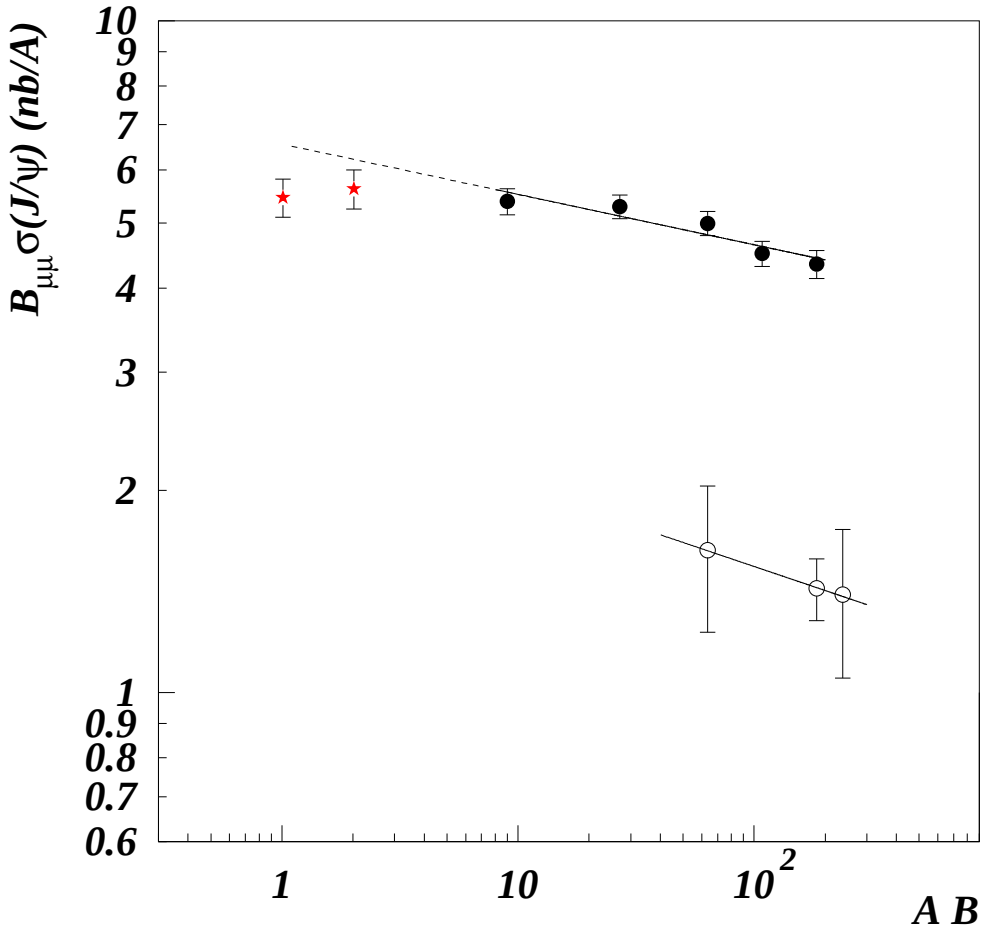

Figure 6.2: Scaling of J/ψ cross section in p-A collisions from 450 GeV/c $-0.4 < y^* < 0.6$ to 200 GeV/c $3 < y_{Lab} < 4$. Separate fits to NA50 points (filled circles) and NA38 p-Al, p-W and p-U points (open circles) are shown.

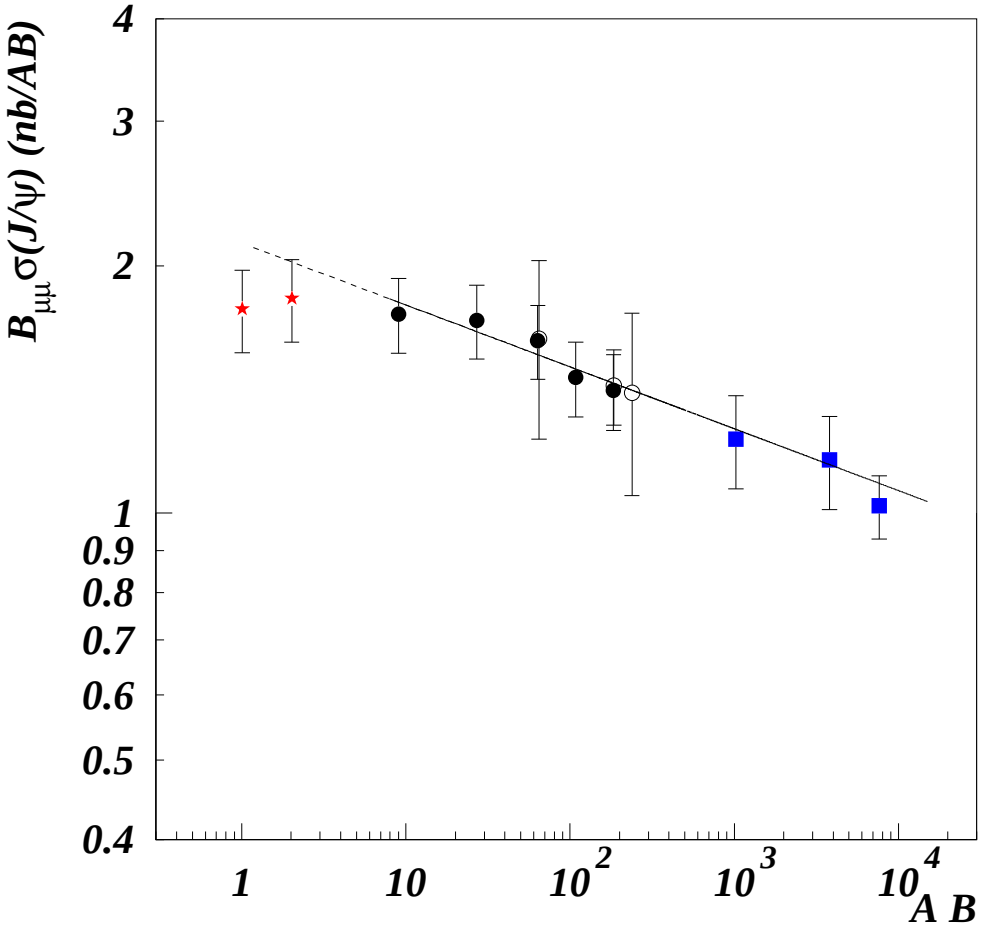

Figure 6.3: J/ψ cross section, rescaled at 200 GeV/c. The p-p and p-d (stars), p-A 450 GeV (filled circles), p-A 200 GeV (open circles), O-S, O-U and S-U 200 GeV (filled squares) points are shown. The fit to the rescaled p-A data is shown.

6.3 The ψ/DY ratio

The measured J/ψ suppression can be interpreted as the result of a breakup of a pre-resonant $c\bar{c}$ state, meant to become later on, if not destroyed, the fully formed J/ψ . It is then convenient to study the J/ψ cross section as a function of the length of nuclear matter that the pre-resonant $c\bar{c}$ state has to cross to escape the region where it was produced.

In this framework the J/ψ cross section can be written at first order as

$$\sigma(AB \rightarrow J/\psi + X) \propto AB\, exp(-\rho_0 \sigma_{abs} \overline{L}) \tag{6.2}$$

where:

- A is the atomic mass of the target, B is the atomic mass of the projectile. Therefore AB is proportional to the total number of nucleon-nucleon collisions. This accounts for the production of the $c\bar{c}$ pair (hard-process),
- ρ_0 is the average nuclear matter density: $0.17\,\text{nucleons/fm}^3$,
- σ_{abs} is the cross section for the pre-resonant J/ψ state with nucleons:

$$(J/\psi)_{pre-resonant} + N \rightarrow D\overline{D} + X \tag{6.3}$$

- $\overline{L}$ stands for the mean path of the $c\bar{c}$ pair within nuclear matter,

The $\overline{L}$ calculation is averaged over the impact parameter in p-A collisions where this quantity is not accessible to measurement. In A-B collisions the $\overline{L}$ is averaged over each impact parameter bin.

The calculation of $\overline{L}$ takes into account the two properties of J/ψ production in proton-nucleus and nucleus nucleus collisions:

- at each stage of the collision, the $c\bar{c}$ production probability is proportional to the number of N-N collisions occurring at that stage,
- the L value takes into account the interaction of the $c\bar{c}$ both with the target nucleons and with the projectile nucleons. In fact the projectile nucleons are moving faster than the $c\bar{c}$ pair, therefore they can interact with the $c\bar{c}$ pair.

In this framework it is extremely useful to compare the J/ψ cross section with the DY cross section for several reasons:

1. as stated several times when the ψ/DY ratio is considered, many uncertainties on the normalisation are washed away

2. the DY cross section is directly proportional to the number of nucleon-nucleon collisions

3. with the ψ/DY ratio it is possible, for nucleus-nucleus interactions, to study the J/ψ production per nucleon-nucleon collision in different centrality bins.

In Figure 6.4 the ψ/DY is plotted versus $\overline{L}$ for the p-A collisions studied in this work. From a simple exponential fit the effective cross section of the J/ψ with nuclear matter is extracted: $\sigma_{\psi N}^{pA} = 4.4 \pm 0.9$ mb.

In Figure 6.5 the ψ/DY ratio, measured at 450 GeV, is rescaled to 200 GeV beam energy and to the kinematical domain of the NA38 experiment. The procedure for DY scaling is reported in Section 4.11. When the rescaling is performed, the uncertainty on the scaling factor is included in the error bars. This is dominated by the error on the J/ψ scaling because the energy dependence of DY production is known from theory with much better accuracy. As said previously, this error is huge and could bias the comparison of the results. A direct comparison of the two data sets is made in Section 6.5.

From the separate fit to the S-U point we get $\sigma_{\psi N}^{SU} = 5.7 \pm 1.9$ mb. The difference between the two cross section is $\Delta\sigma_{\psi N}^{SU-pA} = (1.3 \pm 2.1)$ mb that is compatible with zero.

6.4 The ψ'

In Figure 6.6 the ψ'/ψ ratios extracted in this work are presented together with previous NA38-NA50 and NA51 measurements. The results taken at different energies can be directly compared because no energy dependence is expected in the ψ'/ψ ratio.

The present results indicate a difference of J/ψ and ψ' nuclear absorptions ($\alpha_{\psi'} < \alpha_{J/\psi}$) with a $\Delta\alpha = -0.028 \pm 0.014$ in p-A collisions. The previous results, obtained however with points from different experiments, therefore not sharing the same systematics, indicated a different behaviour $\Delta\alpha = 0.016 \pm 0.009$ [20].

The extrapolation of the ψ'/ψ nuclear dependence up to S-U and Pb-Pb points is not able to explain the measured ψ'/ψ ratio in these collisions, which is much lower.

In Figure 6.7 I plot the ψ'/DY ratio. The ψ' cross sections have been rescaled to 200 GeV using the same scaling factor as for the J/ψ . The larger error bars are caused by the introduction of the scaling factor.

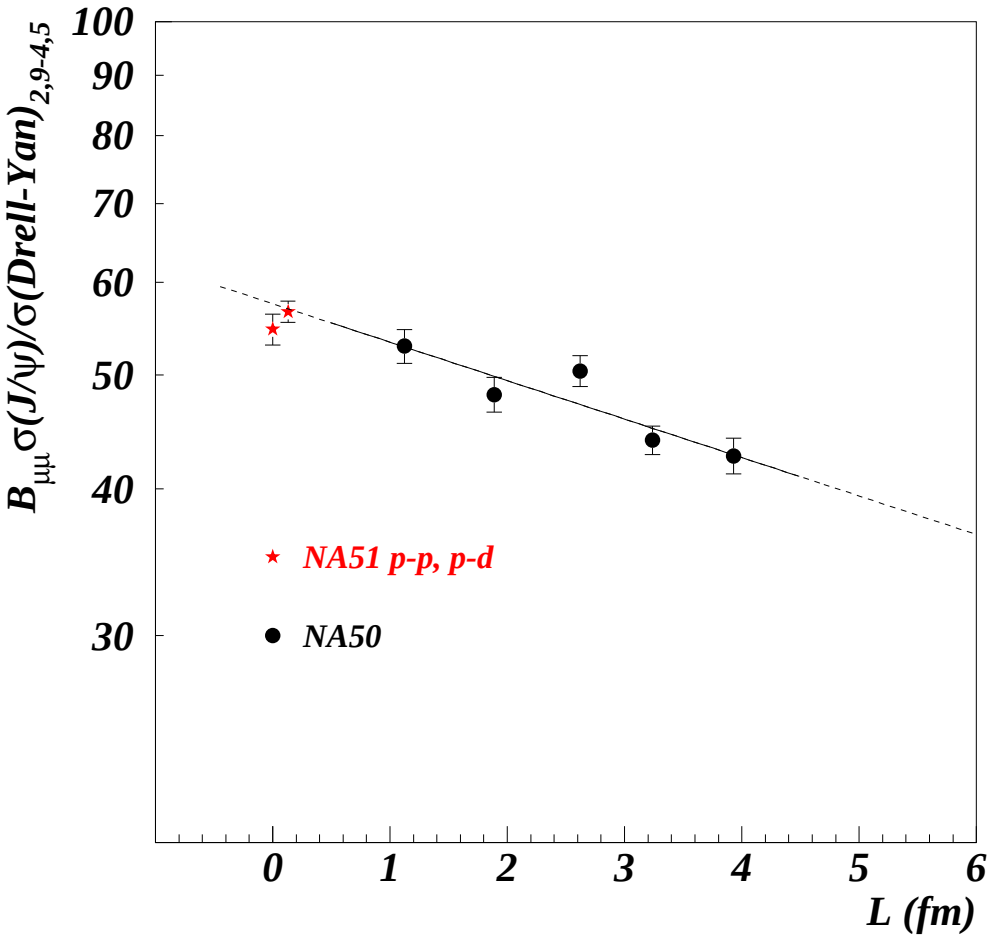

Figure 6.4: The ψ/DY ratio is plotted as a function of L for the values obtained in the present analysis. The continuous line indicate the region where the exponential fit is performed and the dashed line indicate the extrapolation.

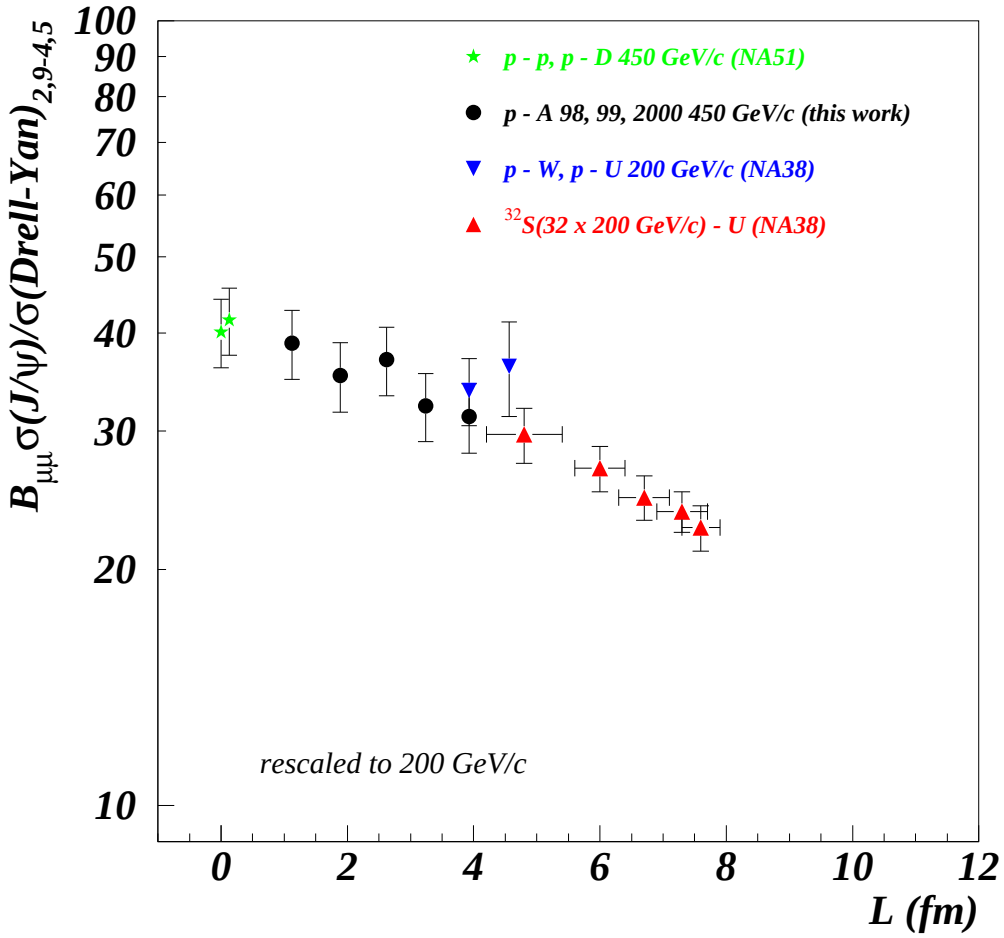

Figure 6.5: The ψ/DY ratio is plotted as a function of L. The results of the presents analysis and of NA51 measurements are rescaled to NA38 energy and kinematical domain.

From the p-A points at 450 GeV we extract an absorption cross section for the ψ' : $\sigma^{pA}_{\psi' N} = 6.4 \pm 1.3$ mb. The NA38 collaboration, from a fit to the S-U points found $\sigma^{SU}_{\psi' N} = 24 \pm 5$ mb.

However, a more refined calculation for the absorption cross section should be performed in this case because the simple exponential fit is valid only when the measured absorption is small.

6.5 Direct comparison of p-A and S-U data

In order to reduce the systematic error due to the rescaling, a different procedure may be used. The results of p-A analysis at 450 GeV incident momentum may be compared directly with the S-U data taken at 200 GeV/c. The rescaling factor can be estimated directly from the measured ψ/DY in p-A and S-U and at the same time the difference in absorption cross section is studied.

In Figure 6.8 I make a simultaneous fit to the two data sets. A common J/ψ absorption cross section is able to describe both results.We get $\sigma_{\psi N} = 4.7 \pm 0.8$ mb with $\chi^2 = 0.96$ while the scaling factor from 450 GeV to 200 GeV is 0.73 ± 0.04 . As said before the two separate fits give $\sigma^{pA}_{\psi N} = 4.4 \pm 0.9$ mb with $\chi^2 = 2.1$ and $\sigma^{SU}_{\psi N} = 5.7 \pm 1.9$ mb with $\chi^2 = 0.03$.

6.6 The absorption cross section of direct J/ψ

As said before in Section 6.5, part of the observed J/ψ yield does not come from direct J/ψ but, instead, is given by the decay of other hadronic resonances into a secondary J/ψ . The various χ_c and the ψ' in fact, decay in a large fraction into J/ψ + X.

In this work, a different nuclear absorption cross section for J/ψ and ψ' has been observed. This may bias the comparison between p-A and S-U results. Therefore the contamination to the J/ψ sample coming form ψ' decay is subtracted using the measured $\sigma_{\psi'}/\sigma_{DY}$ in p-A and S-U. For every measured ψ' , according to the branching ratios reported in [2] 3.13 ± 1.10 J/ψ s are subtracted from the sample. The results are shown in Figure 6.9.

A separate fit to the two sets now gives: $\sigma^{pA}_{\psi N} = 4.3 \pm 1.1$ mb with $\chi^2 = 1.4$ and $\sigma^{SU}_{\psi N} = 5.2 \pm 2.0$ mb with $\chi^2 = 0.03$. The simultaneous fit gives $\sigma_{\psi N} = 4.5 \pm 0.9$ mb with $\chi^2 = 0.63$. The scaling factor from 450 GeV to 200 GeV does not significantly changes: 0.75 ± 0.06 .

One can see that the subtraction of the ψ' contamination gives a better compatibility between the p-A and S-U results: $\Delta\sigma^{SU-pA}_{\psi N} = (0.9 \pm 2.3)$ mb.

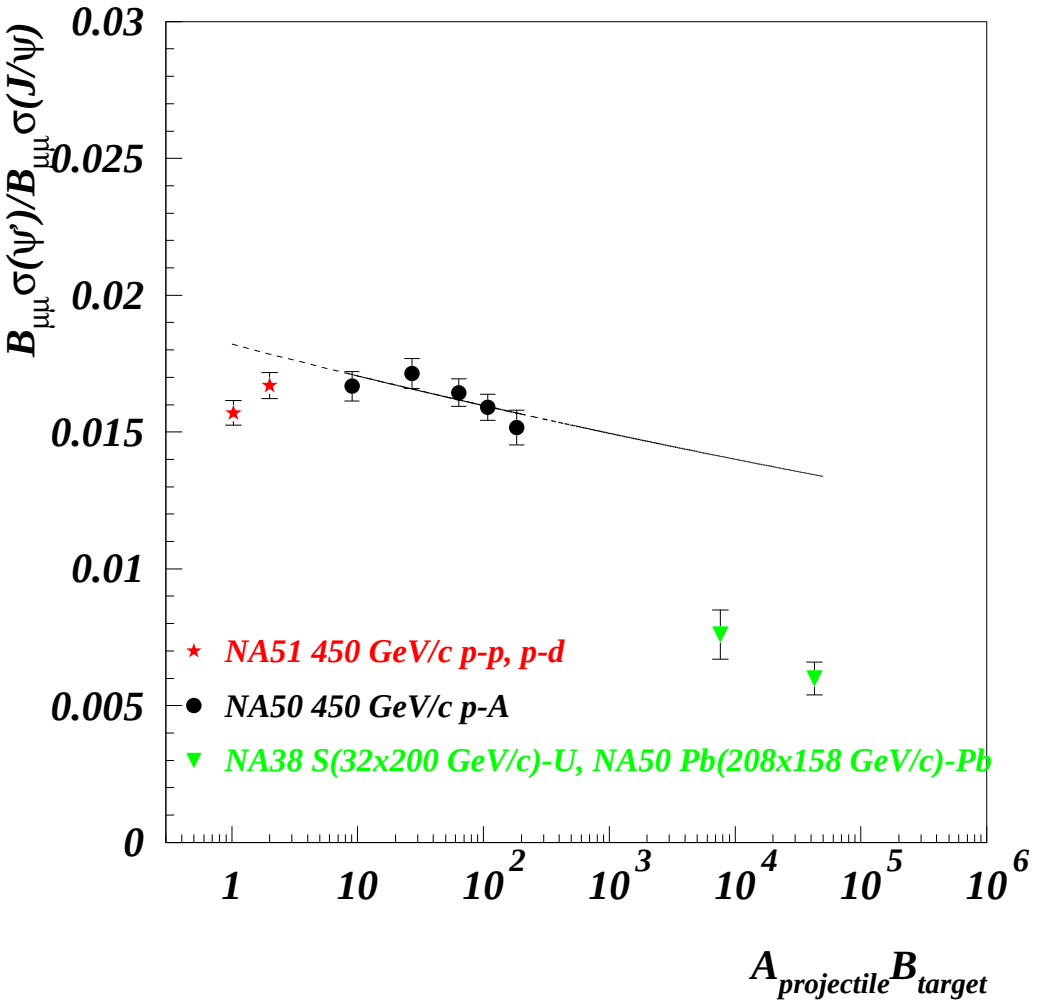

Figure 6.6: The ψ'/ψ ratio obtained in the present work is plotted together with previous NA38, NA50 and NA51 measurements. A constant fit and an $(AB)^{\alpha}$ fit are performed on the points of present analysis.

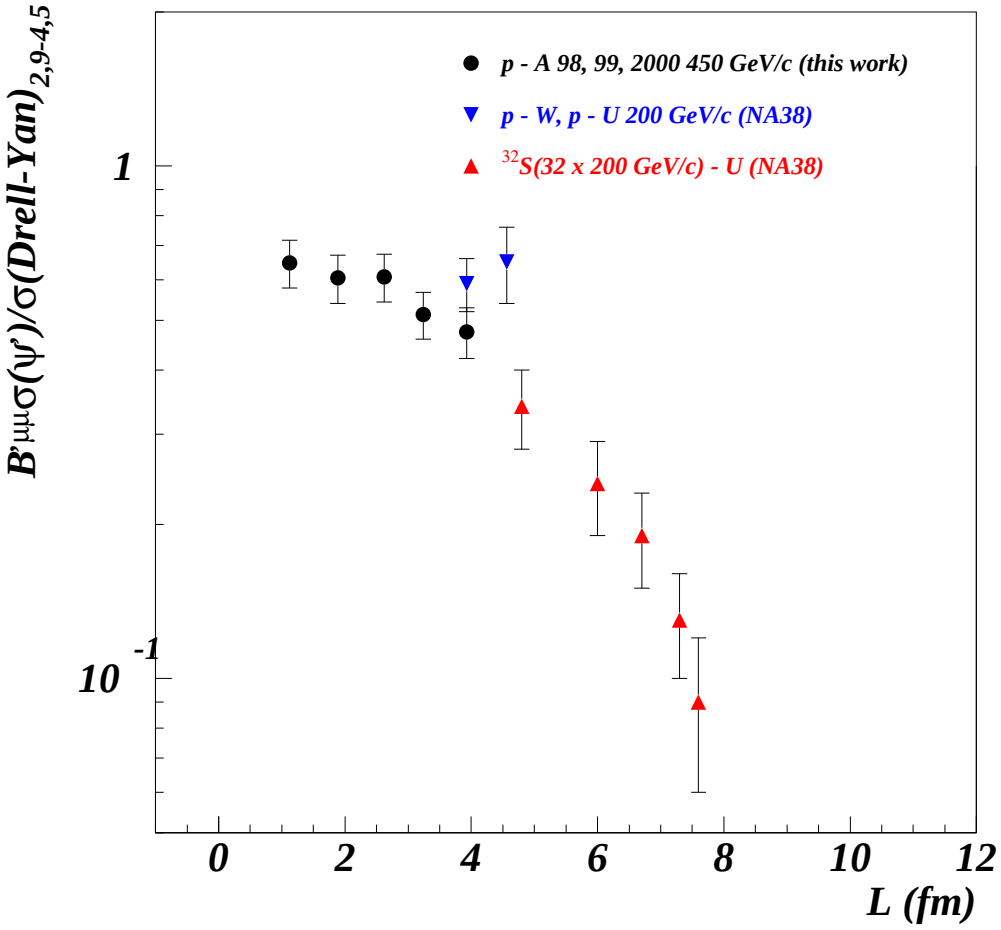

Figure 6.7: The ψ'/DY ratio is plotted as a function of L. The results of the presents analysis are rescaled to NA38 energy and kinematical domain.

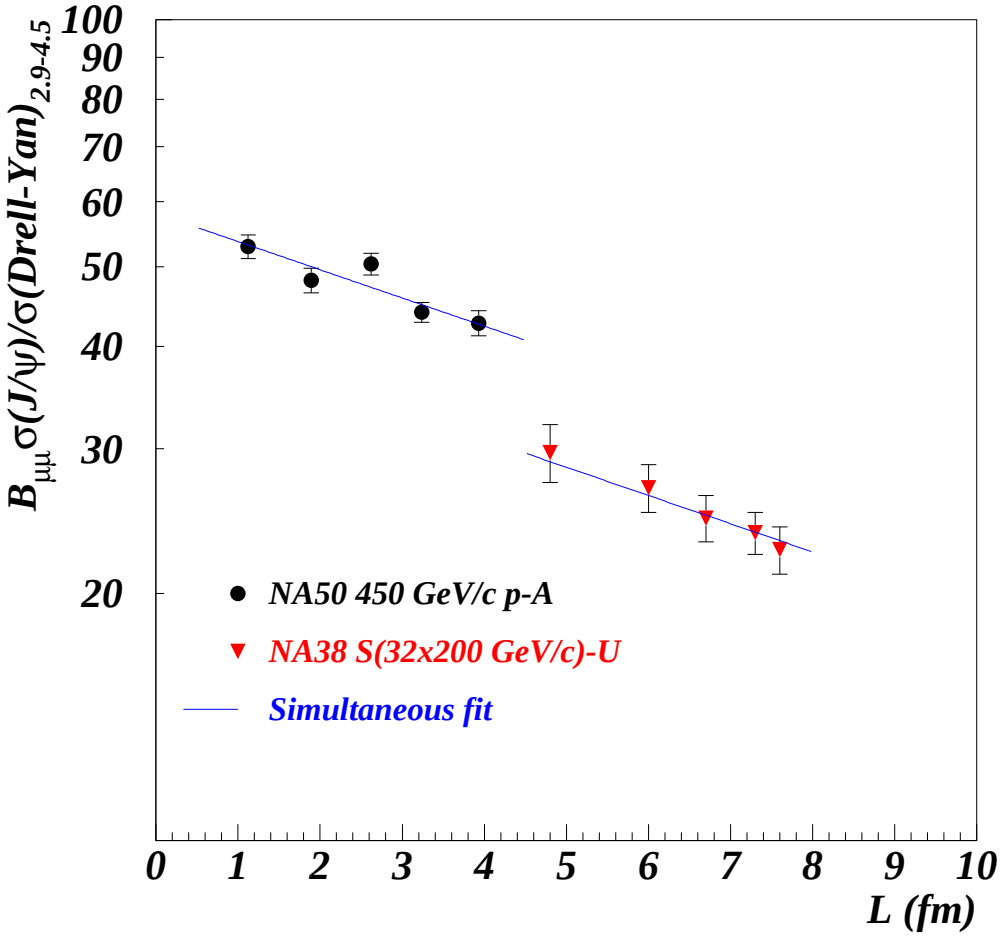

Figure 6.8: The $(J/\psi)/DY$ ratio is plotted as a function of L and a simultaneous fit is performed on p-A and S-U points with common nuclear absorption cross section and a scaling factor between 450 GeV and 200 GeV results.

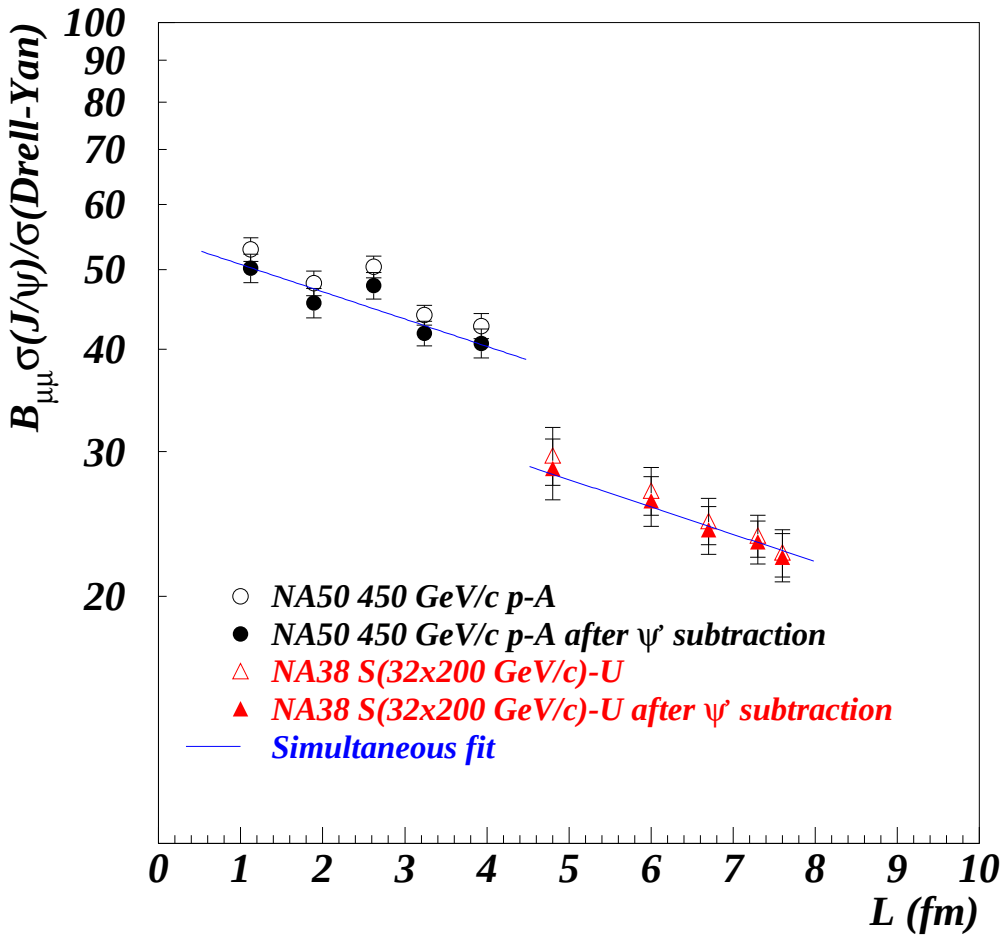

Figure 6.9: Before and after removing the ψ' contamination, the $(J/\psi)/DY$ ratio is plotted as a function of L and a simultaneous fit is performed on p-A and S-U points with common nuclear absorption cross section and a scaling factor between 450 GeV and 200 GeV results.

Chapter 7

Conclusions

In this thesis I have presented an analysis of charmonia and Drell-Yan production in p-A collisions at 450 GeV/c.

In particular, I have obtained the J/ψ , ψ' and DY cross sections on Be, Al, Cu, Ag and W targets, as well as cross section ratios. The nuclear dependence of these cross sections has been parametrised as A^{α} , where A is the target mass number. A deviation of the exponent α from unity is expected in case of the occurrence of nuclear effects.

We have extracted the following α values:

$\alpha_{J/\psi}$	$0.925 \pm 0.018\,(0.002)$
$\alpha_{\psi'}$	$0.913 \pm 0.024\,(0.015)$
α_{DY}	$0.995 \pm 0.025\,(0.016)$

starting from the measured cross sections (the statistical error is reported into brackets).

We see that α_{DY} is compatible with unity, confirming the theoretical expectation that in p-A collisions at 450 GeV, in our kinematical domain, nuclear shadowing does not affect DY production. The DY production cross section is proportional to A and therefore to the number of nucleon-nucleon collisions.

On the contrary the charmonia α values deviate significantly from one, indicating a sizeable nuclear absorption.

The DY process, being proportional to the number of N-N collisions can be used as a good reference to study a hard process as charmonium production.

This led us to consider the ratios of charmonia production cross section with DY, $\sigma_{J/\psi}/\sigma_{DY}$ and $\sigma_{\psi'}/\sigma_{DY}$, which are equivalent to a measurement of the

cross sections per nucleon-nucleon collisions. The study of these ratios allows to cancel most of the systematic errors connected with luminosity measurement and with the estimation of detection efficiency. In this way we have obtained a more accurate estimation of the nuclear dependence of the charmonia cross sections:

$\alpha_{J/\psi}$	0.932 ± 0.014
$\alpha_{\psi'}$	0.905 ± 0.020
$\Delta\alpha = \alpha_{\psi} - \alpha_{\psi'}$	$-0.028 \pm 0.014\,\text{(statistical)} \pm 0.004\,\text{(systematic)}$

In the framework of a simple model of the nuclear absorption of charmonia I have extracted the effective cross sections for charmonia dissociation in the interactions with the nucleons:

$\sigma_{J/\psi N}$	$(4.4 \pm 0.9\ )$ mb	p-A
$\sigma_{\psi' N}$	$(6.4 \pm 1.3\ )$ mb	p-A

These effective cross sections do not refer to the interactions of a fully formed charmonium resonance. In fact, the current theoretical understanding of charmonia production considers three separate steps for the production and evolution of the charmonium state:

1. the production of a $c\bar{c}$ pair in a hard-scattering interaction between a projectile and a target parton
2. the formation of a bound, coloured $c\bar{c}$ state
3. the hadronization of the intermediate coloured state to form the final J/ψ or ψ' resonance

In this approach, the J/ψ and ψ' result from the evolution of a common pre-resonant state. The interaction of the pre-resonant state with nuclear matter, is common to J/ψ and ψ' .

On the contrary, for what concerns the final states, the ψ' is expected to have a larger absorption cross section in the interaction with nuclear matter. In fact the ψ' has a smaller binding energy and a greater radius.

From these considerations it is clear that a quantitative description of charmonia interaction with the nuclear medium is a complicate task. However, the data on p-A collisions presented in this work will hopefully allow to properly tune the proposed models on this subject.

One of the most interesting results obtained in this analysis is the observation of a difference between $\sigma_{J/\psi N}$ and $\sigma_{\psi' N}$ at this energy. This confirms the results of E866 experiment that first measured, at higher energies (800 GeV), a difference between J/ψ and ψ' behaviour [21].

The difference between J/ψ and ψ' behaviour shows that, at these energies, J/ψ and ψ' resonances traverse part of the nucleus as fully formed resonances. This is a strong constraint to theoretical models for what concerns resonance formation times.

The NA50 p-A data were then compared with NA38 S-U data (taken with a similar apparatus), where no effect connected with a phase transition to a deconfined medium has been experimentally observed. On the contrary these effects were observed in Pb-Pb collisions by the NA50 experiment.

Concerning ψ' , the NA38 experiment observed a much higher absorption cross section in S-U collisions ($\sigma_{\psi' N}$ $(24 \pm 5$) mb) than what is now measured in p-A interactions. This is probably due to the dissociation of the loosely bound ψ' resonance (binding energy $\approx$ 50 MeV) in its interactions with the hadronic matter produced in S-U collisions and expanding together with the ψ' (hadronic comovers).

For the J/ψ , which has a higher binding energy (670 MeV), the theoretical understanding is much more controversial. Some authors presume that the J/ψ , once formed, can not be split by the "hadronic comovers", other studies indicate that the interaction with "comovers" can play an important effect.

From NA38 data we have for S-U collisions: $\sigma_{J/\psi N}$ $(5.7 \pm 1.9$) mb and, comparing this result with the pA data analysed in this thesis, I get $\Delta\sigma^{SU-pA} = (1.3 \pm 2.1)$ mb, that is compatible with zero. The two data sets can be fitted simultaneously with a common nuclear absorption cross section $\sigma_{J/\psi N} = 4.7 \pm 0.8$ mb with $\chi^2/\mathrm{dof} = 0.96$.

This value, however, is slightly biased by the contamination of the ψ' generated in the interaction which, through the decay $\psi' \rightarrow \mathrm{J}/\psi + \mathrm{X}$, create an additional J/ψ source.

When this contamination is removed using the measured ψ' yield we get $\Delta\sigma^{SU-pA} = (0.9 \pm 2.3)$ mb.

In summary, the results of this thesis indicate that the absorption cross section of the J/ψ in p-A and S-U collisions are compatible. Therefore no additional source of J/ψ suppression has to be introduced to explain S-U data compared to p-A.

Bibliography

[1] T. Matsui and H. Satz, Phys. Lett. B 178 (1986) 416.

[2] D.E. Groom et al., Eur. Phys. J. C 15 (2000) 1.

[3] F. Karsh et al., Z. Phys. C 37 (1998) 617.

[4] R. Vogt, Phys. Rep. 310 (1999) 197.

[5] C. Gerschel and J. Hufner, Z. Phys. C 56, (1992) 171.

[6] M.C. Abreu et al., Proc. of Quark Matter 1999, Torino 10-15 May, Nucl. Phys A661 (1999) 93c

[7] G.A. Schuler, CERN-TH. 7170/94.

[8] R. Arnaldi, Ph.D. thesis, 2000, Clermont.

[9] C. Soave, Ph.D. thesis, 1998, Torino.

[10] L. Fredj, Ph.D. thesis, 1991, Clermont.

[11] R. Arnaldi et al., Nucl. Instr. and Meth. A 409 (1998) 608.

[12] S. Beolé, Ph.D. thesis, 1998, Torino.

[13] M.C. Abreu et al., Eur. Phys J. C 14 (2000) 443.

[14] K.J. Eskola et al., JYFL-4/00 (Sep. 2000).

[15] A. Baldit et al., NA60 Proposal, CERN/SPSC 2000-010.

[16] M.C. Abreu et al., Phys. Lett. B 438 (1998) 35.

[17] C.M. Lourenco, Ph.D. thesis (1995).

[18] M.C. Abreu et al., Phys. Lett. B 410 (1997) 327.

[19] M.C. Abreu et al., Phys. Lett. B 410 (1997) 337.

[20] M.C. Abreu et al., Phys. Lett. B 466 (1999) 408.

[21] M.J. Leitch et al., Phys. Rev. Lett. 84, 3256-3260 (2000)

Appendix A

Cross sections and ratios of cross sections

Here I report a summary of the results obtained in this work using the "standard" fitting method on absolute cross sections and cross section ratios in the dimuon acceptance window: $-0.4 < y^* < 0.6$ and $|\cos\theta_{CS}| < 0.5$.

Due to a recent re-calibration of the Argon counters used for beam luminosity measurements (see Sec. 2.3.2) the accuracy on the calibration factor has been improved. In this section I quote the updated absolute cross sections. This has no consequence on cross section ratios and on the determination of the nuclear dependencies of the different processes.

A.1 J/ψ cross section

system	Cross section (nb/A)	err. (nb/A)	statistical err. (nb/A)
p Be	5.19	0.23	0.02
p Al	5.10	0.21	0.02
p Cu	4.82	0.20	0.01
p Ag	4.34	0.19	0.01
p W	4.19	0.20	0.02

A.2 ψ' cross section

system	Cross section (pb/A)	err. (pb/A)	statistical err. (pb/A)
p Be	86.4	4.9	2.9
p Al	87.2	4.8	3.1
p Cu	78.6	4.1	2.6
p Ag	69.1	3.8	2.3
p W	69.5	4.6	3.2

A.3 DY cross section $(2.9 < m_{\mu\mu} < 4.5\,\mathbf{GeV})$

system	Cross section (pb/A)	err. (pb/A)	statistical err. (pb/A)
p Be	98.3	5.7	3.6
p Al	107.9	5.7	3.9
p Cu	94.8	5.0	3.2
p Ag	100.9	5.3	3.1
p W	99.8	6.5	4.5

A.4 $\sigma_{\mathbf{J/\psi}}/\sigma_{\mathbf{DY}}(2.9 < m_{\mu\mu} < 4.5\,\mathbf{GeV})$

system	$\sigma_{\mathrm{J}/\psi}/\sigma_{\mathrm{DY}}$	err.
p Be	52.9	1.7
p Al	48.1	1.6
p Cu	50.4	1.5
p Ag	44.0	1.2
p W	42.7	1.5

A.5 $\sigma_{\psi'}/\sigma_{\mathbf{DY}}(2.9 < m_{\mu\mu} < 4.5\,\mathbf{GeV})$

system	$\sigma_{J/\psi}/\sigma_{DY}$	err.
p Be	0.882	0.042
p Al	0.825	0.042
p Cu	0.828	0.039
p Ag	0.700	0.032
p W	0.647	0.040

A.6 $\sigma_{\psi'}/\sigma_{\mathbf{J}/\psi}$

system	$\sigma_{\psi'}/\sigma_{J/\psi}$ standard method	error
p Be	0.0167	0.0005
p Al	0.0171	0.0006
p Cu	0.0164	0.0005
p Ag	0.0159	0.0005
p W	0.0152	0.0006

system	$\sigma_{\psi'}/\sigma_{J/\psi}$ uniform smearing	error
p Be	0.0167	0.0004
p Al	0.0165	0.0005
p Cu	0.0163	0.0005
p Ag	0.0158	0.0005
p W	0.0144	0.0006

List of Tables

List of Figures